Design of a Propulsion System for Swimming Under Low Reynolds Flow Conditions

by

Michael W. Wybenga

A thesis
presented to the University of Waterloo
in fulfillment of the
thesis requirement for the degree of
Master of Applied Science
in
Systems Design Engineering

Waterloo, Ontario, Canada, 2007

I hereby declare that I am the sole author of this thesis. This is a true copy of the thesis, including any required final revisions, as accepted by my examiners.

I understand that my thesis may be made electronically available to the public.

Michael W. Wybenga

Abstract

This work focuses on the propulsion of swimming micro-robots through accessible, quasi-static, fluid-filled, environments of the human body. A literature review of currently proposed systems reveals that no safe and simple propulsion system exists to achieve this goal.

The intended operating environment of the system dictates the design constraints. Biocompatability is key as is the ability to function under low Reynolds number flow conditions. In this fluidic regime, viscous forces dominate and inertial forces are essentially negligible.

Inspiration is drawn from biological examples of propulsion systems that exploit the dominance of viscous forces. A system based on the prokaryotic flagella is chosen due to its simplicity; it is essentially a rigid helix that rotates about its base. However, the system cannot be used directly since a rigid helix poses a piercing threat *in vivo*.

To eliminate the piercing threat, a propulsion system utilizing a flexible filament is proposed. The filament is designed such that under rotational load, and the resulting viscous drag, it contorts into a helix and provides propulsive force. To facilitate correct contortion: (1) the filament must balance the viscous drag forces with the body stiffness, (2) bending must be predisposed to a controlled axis that twists down the length of filament, and (3) the base of the helix must resist the loads transferred to it.

Four mathematical models are created to investigate the behaviour of the proposed flexible filament: two analytical models (resistive-force theory (RFT) and the Lighthill model), an ADAMS model using a lumped-parameter approach for fluid drag, and a finite element model. An experimental prototype of the flexible tail is built for similar purposes. An experimental rigid tail is also built to serve as a benchmark.

The finite element model fails to generate meaningful results and is discarded. Also, since the experimental set-up utilizes a fixed motor, the Lighthill model is not directly comparable so it too is discarded. The remaining models are compared against one another as well as the experimental tails.

The experimental results for propulsive force generated by the rigid tail match the RFT model. An analysis of the system concludes that experimental error is likely minor. The ADAMS model of the rigid tail, as a result of modelling error, under-predicts the propulsive force.

The experimental flexible filament shows that the proposed propulsion system is feasible. When actuated, the tail contorts into a ‘helix-like’ shape and generates propulsive force. An ADAMS model of an ideal flexible filament shows that, if a complete helix is formed, there is no loss in performance when compared to a rigid counterpart. Unfortunately, the experimental filament is too stiff to form a complete helix. Accordingly, the idealized-filament ADAMS model does not simulate the experimental filament well.

To decrease this discrepancy, a second ADAMS model, attempting to directly simulate the experimental filament, rather than an ideal one, is created. This model provides results that match better with the experimental results, although significant inaccuracy still exists. Regardless, the second ADAMS model gives confidence that a multi-body dynamic model using lumped-parameter drag forces, after further modifications, can simulate the experimental flexible filament well.

Acknowledgements

First and foremost I would like to thank Dr. John McPhee and Dr. Eric Kubica, my two supervisors at the University of Waterloo, without whom this project would have never existed. I would also like to thank Dr. Mile Ostojic of the National Research Council, Intergrated Manufacturing Technology Institute who provided the initial idea for this work. Much gratitude is also given to the National Sciences and Engineering Research Council of Canada who provided the bulk of the funding for this project. Thanks should also be given to Dr. Stephen Birkett who allowed me to use his extensive lab facilities. There are countless others who helped with this project and to name them all would be an impossibility: regardless, I thank them all.

Contents

List of Tables

List of Figures

Nomenclature

$a\ [m]$	Helix filament radius — cylindrical cross-section
$b\ [m]$	Helix filament amplitude
$\beta\ [deg \text{ or } rad]$	Helix pitch angle
$C_s\ \left[\frac{N\cdot s}{m^2}\right]$	Gray/Hancock resistive coefficient for motion tangential to helix centreline
$C_n\ \left[\frac{N\cdot s}{m^2}\right]$	Gray/Hancock resistive coefficient for motion normal to helix centreline
$F_{body}\ [N]$	Linear drag force felt by the body when moving
$F_R\ [N]$	Propulsive force generated by tail when body is free to move
$F_{R0}\ [N]$	Propulsive force generated by tail when body is fixed
$g\ \left[\frac{m}{s}\right]$	Acceleration due to gravity
γ	C_n/C_s
$h\ [m]$	Helix filament height — rectangular cross-section
k	$2\pi/\lambda$
$K_s\ \left[\frac{N\cdot s}{m^2}\right]$	Cox tangential drag coefficient for cylinder
$K_n\ \left[\frac{N\cdot s}{m^2}\right]$	Cox normal drag coefficient for cylinder
$L_t\ [m]$	Total length of helix along centreline
$L_i\ [m]$	Length of the i^{th} link
$M_{body}\ [N\cdot m]$	Rotational drag torque felt by the body when moving
$M_R\ [N\cdot m]$	Required tail driving torque when body is free to move
$M_{R0}\ [N\cdot m]$	Required tail driving torque when body is fixed

λ $[m]$	Helix wavelength — projected onto plane through axis of rotation
Λ $[m]$	Helix wavelength — along filament centreline
ϕ_i $[deg$ or $rad]$	desired angle of deflection for i^{th} joint
ρ $\left[\frac{kg}{m^3}\right]$	Fluid density
R $[m]$	Body radius
τ $[m]$	Helix torsion
μ $\left[\frac{N\cdot s}{m^2}\right]$	Fluid viscosity
U $\left[\frac{m}{s}\right]$	Swimming velocity of body
V $\left[\frac{m}{s}\right]$	Velocity of point on helix
V_s $\left[\frac{m}{s}\right]$	Velocity, tangential to helix centreline, of point on helix
V_n $\left[\frac{m}{s}\right]$	Velocity, normal to helix centreline, of point on helix
w $[m]$	Helix filament width — rectangular cross-section
ω $\left[\frac{rad}{s}\right]$	Rotational velocity of tail with respect to body
ω_e $\left[\frac{rad}{s}\right]$	Rotational velocity of tail with respect to fluid
Ω $\left[\frac{rad}{s}\right]$	Body rotation rate with respect to fluid
ξ_i $[deg$ or $rad]$	Angle of twist between links for i^{th} link

Chapter 1

Introduction

In 1966 the science fiction film *Fantastic Voyage* took viewers, along with 5 miniaturized humans and a miniaturized submarine, into the human body to save a man's life. Today, doctors around the world use wireless capsule endoscopes, ingested by patients, to capture images of the most remote sections of the human gastro-intestinal tract. In the future, miniature robots will be guided through the human body to diseased areas for observation, analysis, and treatment. A world that was once the realm of science fiction is quickly becoming a reality.

This thesis lays the ground work for technology that is expected to be commercially feasible in 5-10 years. At that time, it is expected that wireless, *in vivo*, medical devices will be able to actively explore environments that only provide a few millimeters of free space. These include the eyeball, gastro-intestinal tract, circulatory system, respiratory system, urinary tract, spinal chord, and renal system. From a mechanical stand-point, one of the challenges is how to propel the devices through these environments safely. This challenge is the main focus of this work.

1.1 Motivation and Goals

Wireless *in vivo* medical devices already prove invaluable to the medical community. In the near future they will become even more indispensable. They offer a promise of non-invasive procedures that allow for first-hand observation, biopsy, analysis, and eventually treatment of multitudes of diseases. Furthermore, *in vivo* micro-robots will also allow for medical devices to reach areas of the human body that are currently inaccessible. They have the potential to save lives while easing the trauma of invasive medical procedures.

There is still much work to be done though before these devices will be readily available. One of the challenges regarding their development is locomotion through the different environments of the body. Since the possible environments are vastly different, this work focuses on those that are fluid-filled. Narrowing the focus aligns the scope of the project with the time-line.

Accordingly, this work is viewed as a stepping stone toward the development of a propulsion system able to operate in the fluid-filled environments of the human body. Therefore, as a first step, the main goal of this work is to develop a conceptual propulsion system that is safe and simple. Furthermore, the design should be proven at the proof-of-concept level but not necessarily developed to the point where it could be used in a final product.

1.2 Project Outline

The process undertaken to achieve the goals outlined in Section 1.1 begins with a background review of *in vivo* medical devices. The focus of the review is on wireless devices that are tailored for use in static, fluid-filled environments. These environments were chosen to narrow the scope of the project to fit more closely with the project time-line. The purpose of the literature review is to illuminate an area of *in vivo* micro-robot propulsion that has not been fully investigated. The result of the literature review is that, currently, no safe, simple propulsion system exists with the ability to explore more than one fluid-filled *in vivo* environment. The projects reviewed either proposed propulsion tailed for a single, specific environment, complicated systems, or systems that have safety issues. Therefore, it was decided that this project should attempt to address what is currently lacking.

The design process to develop the new propulsion system involves identifying the need, the design constraints, and the design criteria. The largest constraint identified is that, due to size restrictions imposed by the scale of *in vivo* environments, the propulsion system must operate under low Reynolds number flow conditions. In terms of design, this means that conventional propulsion systems like jets and boat propellers will not work. However, low Reynolds flow propulsion systems exist in nature and, as part of the design process, these were drawn upon for inspiration. Accordingly, by examining the natural systems, several possible designs were identified and compared. The final concept chosen involves emulating a bacterial helical flagellum with one major modification. Instead of using a rigid filament, comparable to a corkscrew, the filament is flexible and contorts into the corkscrew shape under rotational load. In this way, the flexible filament will not pose a piercing threat inside the body simply because it is not stiff enough. As the final step of the design process, the flexible filament propulsion system is designed in detail.

The feasibility of the proposed flexible filament propulsion system is then explored using several models. Two analytical models are used: Resistive Force-Theory as developed by Gray and Hancock [1] and the Lighthill model [2]. Two computer-based models are also used. The first is a simplified multi-body dynamic model utilizing a lumped parameter approach for fluid drag. It is implemented in MSC.ADAMS. The second is a finite element model using a coupling algorithm for fluid drag. It is implemented in LS-DYNA. Unfortunately, the finite element model is unsuccessful in execution. However, the three remaining models are implemented such that they are directly comparable and the result is that there is strong evidence supporting the feasibility of the flexible filament design. However, discrepancies between the models means that no one model can be deemed accurate enough to act as a precise design tool.

To infer the level of accuracy needed for a model to be used as a precision design tool, comparison to a physical system is required. Accordingly, three different propulsion systems based on helical flagella are built and tested. Experiments are conducted on a custom test bench designed to overcome the challenge of measuring forces that are predicted by the aforementioned models to be at the nano-Newton level. Accordingly, the length scale for the entire system is scaled up by a factor of twenty. The Buckingham Pi theory of non-dimensional analysis is used to ensure that similitude exists. Also, a cantilever beam configuration is utilized to amplify the propulsive forces generated by each of the three systems.

The observations made during the experimental phase show that the flexible filament is a feasible propulsion system. However, modifications to the prototype, made to ease the manufacturing process, cause a drop in performance when compared to a rigid helical flagellum. The main cause for the performance drop is the inability of prototype filament to fully contort into a complete helix. Recommendations to reduce this performance drop are given. Another observation is that the models created do not simulate the propulsion system accurately enough to be considered a precise design tool. However, it is speculated that the MSC.ADAMS model, with modifications, could achieve this status. Recommendations regarding these modifications are given as well.

1.3 Contributions

This work provides several contributions to the development of swimming micro-robots. First, a new propulsion system is developed that is simple yet safe for use *in vivo*. The design, through the use of computer modelling and experimental testing has been shown to be feasible. Second, the developed lumped-parameter model is a contribution to the state of the art. It will provide the basis, to be built upon, for a design tool that will provide a low computation-cost means for predicting the performance and requirements of the propulsion system. This will prove invaluable in reducing development effort for future iterations of the proposed propulsion system.

Another contribution of this work is in the area of analytical modelling of biological organism utilizing helical flagellar motion. This work extends the principles of resistive force-theory to prokaryotic helical flagellar motion. Previous works have only considered eukaryotic helical flagellar motion.

1.4 Document Structure

Chapter 2 provides a background review of pertinent works pertaining to exploration of the human body *in vivo*. The review begins with the advent of passive endoscopic capsules and continues through newer projects that are still conceptual. Instances where the literature is directly related to this work are examined more closely to determine if the results presented can be used here.

Chapter 3 focuses on the design of the proposed propulsion system. The chapter contains the entire design process from conception to detailed design. This includes an evaluation of the design constraints, design criteria, design inspirations, and possible alternatives.

Modelling of the proposed system is outlined in Chapter 4. The models created include two analytical models, a lumped parameter model developed in MSC.ADAMS, and a finite element approach developed in LS-DYNA. Results from each model are gathered and compared to the other models.

Chapter 5 outlines the development and testing of a prototype of the propulsion system. The prototype is used to validate the models previously mentioned. The chapter outlines the test bench construction, the experimental procedures followed, and analyzes the experimental results.

Chapter 6 contains a summary of the conclusions and recommendations made throughout the rest of the report.

Chapter 2

Background & Literature Review

Capsule endoscopy involves the inspection of the gastrointestinal (GI) tract using a wireless capsule instead of a traditional tethered endoscope. Passive capsules travel through the GI tract using natural peristalsis while active capsules locomote using their own propulsion mechanisms.

Originally this work pertained to the development of an active capsule endoscope. Accordingly, a background and literature review on the topic was conducted [3]. It is reproduced, in modified form, here in Sections 2.1 and 2.2.

The conclusion of [3] is that several large, well-funded active capsule endoscope projects are underway. Therefore, attempting to provide significant, recognizable contributions to the field, with the possibility of creating commercially successful products, would be a serious challenge.

However, shifting the focus of the project to explore more forward-thinking technologies would illuminate research corridors less explored. A decision was made to focus less on the gastrointestinal tract, and more on swimming robots for use in all fluid-filled, *in vivo* environments. Section 2.3 outlines the state of the art in this area of research and discusses areas that have not been sufficiently explored.

2.1 Passive Propulsion Capsule Endoscopy

The following section outlines two passive propulsion capsule endoscopes. As mentioned, passive capsules move as a result of natural peristalsis. This limits their functionality such that they are used only if traditional endoscopes – with the ability to perform biopsy, but cannot access the entire GI tract – fail to illuminate the problem [4]. Regardless, passive endoscopes fulfill a useful niche in hospitals worldwide.

2.1.1 Given Imaging: Pioneering Capsule Endoscope

Given Imaging is the pioneer of capsule endoscopy. Their product, the Pillcam™, was first introduced in the late 1990s [5]. Today the Pillcam™ is available in two single-use models: SB and ESO.

The SB model contains a single camera to allow for imaging of the human (GI) tract. Specifically, its target is the twenty feet of small intestine that is inaccessible by tradition endoscopy and colonoscopy.

In operation, the pill moves through the GI tract via natural peristalsis. Twice a second, batteries power four light emitting diodes and an image is taken. The image is transmitted wirelessly to a data recorder worn by the user. Eight external sensors, also worn by the user, track the position of the pill as it travels. The pill takes roughly eight hours to move through the GI tract. The patient's daily routine is uninterrupted during this time.

The ESO model is intended for use in the human esophagus. The shorter length of the esophagus translates into a shorter required battery life. Accordingly, the ESO model contains a second camera and takes fourteen images a second. Data collection is the same as the SB model. Propulsion is accomplished by having the user swallow the pill while lying down. They are then raised by thirty degree angular increments to slide the capsule toward the stomach. The procedure lasts for approximately twenty minutes.

For both models, when the examination is complete, the collected data is imported into Given Imaging's proprietary RAPID® software. Using this software, a doctor will examine the images and note areas that are of special interest. As a supporting tool, RAPID is equipped with proprietary diagnostic tools such as the suspected blood indicator. However, its main functionality is no different than a standard image viewer.

2.1.2 RF System Lab: Orientation Control

RF System Lab in Japan is developing what they hope will be the next generation of capsule endoscopes. It is called the Norika3. Although the capsule is not yet approved for human use, it appears that it will be shortly.

When compared to the Pillcam™ there are two major technological advances implemented in the Norika3. First, using magnetic fields, orientation control has been achieved – forward propulsion is still peristaltic. Second, wireless power transmission has been implemented, eliminating the requirement for batteries. Other features of the Norika3 that differentiate it from the Pillcam™ are:

- Camera is equipped with a focusing system
- Lighting is accomplished with 2 white LEDs and 2 near-infrared LEDs (the Pillcam™ has 4 white LEDs)
- CCD camera used (Pillcam™ uses CMOS)
- Images transmitted 30 times per second (Pillcam™ takes 2 images per second)
- Extra space allocated for medicine/biopsy tanks (currently not used)

The control aspects of the Norika3 capsule – orientation, camera focus, and lighting – are accomplished via a remote operator. The interface for the control is a joystick similar to everyday gaming devices [6].

Control via human operators is a major disadvantage of the Norika3 since it increases the invasiveness of the procedure. Peristaltic motion equates to a capsule travel time of roughly 8 hours. Since an operator must monitor the robot for optimal results, the patient has no choice but to remain at the testing facility for the duration of the procedure.

2.1.3 Discussion

While both Given Imaging and RF Systems Lab have developed passive capsule endoscopes, Given Imaging is the dominant player in the market. For instance, to date, over 340,000 patients have used the Pillcam™ since its FDA approval in 2001 [7].

Their head start into the field is considerable especially when one considers the lengthy process of having medical devices approved for human use. Another consideration is the infrastructure – training, hospital space, monitoring stations – associated with the product. To expect medical centers to overhaul their existing infrastructure in exchange for limited advances in the technology is unrealistic. Consequently, attempting to successfully introduce another passive capsule endoscope onto the market without new, compelling benefits would be very difficult.

For this reason, it is unwise to dedicate resources, such as this work, to the development of passive capsule endoscope technology. It is desirable to explore developments into the next generation of capsules to see if progress can be made there. This exploration is outlined in the following section.

2.2 Active Propulsion Capsule Endoscopy

Their exists a trade-off between current capsule endoscope technology and traditional endoscopy. Capsule endoscopy provides a less invasive procedure and can image more of the GI tract than a traditional endoscope. However, the movement of a traditional endoscope is fully controllable allowing for doctors to examine interesting areas more fully and to glaze over healthy tissue.

To eliminate this trade-off, several projects – as outlined in this section – are underway to add active propulsion to capsule endoscopes. The intent is to use active propulsion to mimic the functionality of traditional endoscopy.

2.2.1 Olympus & Arai/Ishiyama Laboratory: Corkscrew Propulsion

Active propulsion as proposed by Olympus and the Arai/Ishiyama Laboratory, Research Institute of Electrical Communication, Tohoku University, is comparable to a corkscrew moving through the GI tract. They have developed a pill casing that has a helical ridge embossed on its outer wall that grips the intestinal wall. Rotating the pill using external magnetic fields causes locomotion through the GI tract [8] Arai and Ishiyama concluded that a capsule with a helix of two complete turns, embossed at a height of 1 $[mm]$, could navigate at 5 $[mm/s]$ [9].

The technology, as proposed by Olympus, incorporates many of the technological advancements seen in the Norika3 such as wireless power transmission, a drug delivery tank, and a fluid biopsy tank. A capsule equipped with ultrasonic imaging capabilities is also proposed [8].

At this date, Olympus has yet to release their active capsule. However, they did release a passive capsule in late 2005. It has the same functionality as the Pillcam™ but is equipped with a high resolution camera. Olympus has also released an ultrasonic version of their passive capsule.

2.2.2 IMC: Legged Propulsion

The Intelligent Microsystem Center (IMC) is located in Korea and functions as part of that government's 21st Century Frontier Research and Development Program. Their goal is to create an actively-propelled endoscope by the end of 2006 [10]. To accomplish this they have contracted the services of several research groups including (1) the Korean Institute of Science and Technology (KIST) (2) The Center of Research in Microengineerng (CRIM) located at the Scuola Superiore Sant'Anna in Italy and (3) the Nanorobotics Lab at Carnegie Melon. Together they are in a well-funded partnership to create an active capsule endoscope with increased functionality [10]. The IMC and CRIM have quantified these functional improvements as such:

- Clamp and resist peristalsis for a period of 24 hours[1]

---

[1] A capsule tailored specifically for this purpose is listed as part of a patent application filed by the Korean

- Locomotion speed > 70 $[mm/s]$ (small intestine), > 50 $[mm/s]$ (large intestine) [10]

IMC's proposed solution to these design requirements is in the form of a six-legged capsule [12]. In developing the system they have gone through several different mechanisms. First, CRIM and KIST proposed a robot utilizing six legs each with one active DOF and one passive DOF [13]. Each leg could be activated separately using independent SMA actuators. A single leg prototype of the system was tested *in vitro* on intestinal tissue. The results show that the legs apply adequate force to propel the capsule.

Second, the researchers proposed a robot with multiple active degrees of freedom on each leg. They have presented the results of a multi-body simulation showing the robot moving through a compliant tube [14].

More recently, a new design was proposed by the Nanorobotics Lab that utilizes beetle-inspired adhesives on the leg tips. In this iteration, the legs are not used to propel the robot but simply to anchor the capsule. Locomotion is accomplished using an inch-worm mechanism built into the capsule [15].

2.2.3 Given Imaging: Active Pillcam™

Given Imaging is also preparing to move toward active systems. In fact, they are positioning themselves to create a full set of diagnostic tools for the entire GI tract including the stomach and colon. As evidence, below is a list of some of their pertinent patents.

- Implementation of wireless power transmission via induction to a capsule endoscope [16]
- Orientation and locomotion of a capsule endoscope controlled by external magnetic fields [17]
- Capsule propelled by an embedded magnetohydrodynamic propulsion system [18]
- Extensible arms for drug delivery/biopsy [19]
- Capsule, aimed at stomach exploration, complete with ballast to stabilize position and orientation. Moving the human "around" the capsule allows specific locations to be viewed [20]

Outside of these patents details are scarce, as Given is a corporation that does not publish its developments.

Institute of Science and Technology [11].

2.2.4 Discussion

Research into the next generation of capsule endoscopes is well underway. To increase functionality, future capsules will incorporate wireless power transmission, biopsy/drug deliver tanks, and active propulsion. The forerunners in developing these systems are Given Imaging, Olympus Medical Systems, and the Intelligent Microsystem Centre.

However, none of these projects have been released to market or even developed as a final product suitable for clinical trials. The agenda set forth by the IMC calls for their system to be finished by the end of 2006 [10]. At that point, clinical trials would still need to take place. The agenda of Given Imaging is unknown. Olympus initially presented their concept for their active pill in May 2005 [8]. There has been no further announcements. Accordingly, if a product was developed, at this point, there would be no “second-to-market” barriers.

Furthermore, the propulsion systems presented are not proven in real-world situations. The Olympus propulsion system has, so far, only demonstrated success in navigating *in vitro* environments at 5 $[mm/s]$ [9]: results for *in vivo* navigation are not available. IMC has demonstrated success in adhering to a vinyl tube [15]: they have not demonstrated adhesion in an environment similar to the intestine nor a working caterpillar propulsion system. The situation is such there could be room for innovations that would make for a better product.

However, these projects have an advantage due to the large amount of resources allocated to them. Both Olympus and Given Imagining are large international corporations with presumably large R&D budgets. IMC has researchers from six institutions, funded by eight million USD per year, working on their project [10, 12]. Competing against these resources as a small team of university researchers is not a good idea.

A smarter approach is to envision future *in vivo* inspection devices. Accordingly, the focus for this work was shifted from the GI tract to all fluid-filled, *in vivo* environments. Also, instead of creating an entire inspection robot, the focus is on creating a modular subsystem for these robots. Specifically, it was decided to develop a propulsion system capable of navigating these environments.

2.3 Propulsion in Liquid-Filled, *In Vivo* Environments

As manufacturing techniques shrink technology, all parts of the human body will be accessible for inspection, diagnosis, and treatment of disease. Currently, technology is small enough to allow for inspection of the GI tract using passive capsule endoscopes. The next-generation of capsules will allow for active inspection of the GI tract.

Other *in vivo* environments include the circulatory system, the respiratory system, the lymphatic system, the renal system, the sub-arachnoid space in the spinal chord, and the eyeball. With the exception of the respiratory system, all of these systems are filled with liquid and could be explored with a submersible micro-robot. Navigation will require the development of new small-scale propulsion systems. This section explores projects that aim to accomplish that goal.

2.3.1 Nanorobotics Lab at Carnegie Melon: Flagellar Propulsion

The Nanorobotics Lab at Carnegie Mellon is developing a micro-swimming robot propelled by a rigid helix as inspired by an E. Coli bacterium. Initially (2003), the researchers proposed a multi-flagellar system for use in the renal system. By assuming that each flagella is independent of its neighbour, they theorize that a 1 $[mm]$ spherical robot body could propelled at almost 1 $[mm/s]$ with a 2% hydrodynamic efficiency (1 $[nW]$ input) using 100 $[\mu m]$ long, 60 $[nm]$ diameter filaments. The number of filaments is undisclosed [21]. These numbers are generated based on a incomplete Resistive-Force Theory (RFT) analytical analysis (Section 4.1.1): the model developed fails to take into account the torque generated as the flagellum rotates about the tangent of its helical centre-line. The incompleteness of the model is not acknowledged.

Following that, under a new principal researcher, results were presented based on a single flagellum system [22]. Once again, an incomplete RFT was used to predict performance. Validation was attempted by building a scaled prototype. Comparing results for swimming force, Behkam and Sitti claim that the analytical model over-predicts the experimental values by a constant factor. The analytical model predicts a force versus rotation frequency linear relationship of:

$$y = 1.93x \tag{2.1}$$

whereas the experimental results yield:

$$y = 2.3x - 9.5 \tag{2.2}$$

where y $[mN]$ is the thrust force and x $[Hz]$ is the rotational frequency of the flagella. The difference in slope between (2.1) and (2.2) means that the two systems are not different by a constant factor. Also, the experimental results consist of only two data points. The negative y-intercept of (2.2) implies, in the absence of other forces, that the system is moving backwards when the motor is turned off. No other forces are accounted for in Beckam and Sitti's results and the negative y-intercept is not accounted for. Accordingly, only the two data points given should be regarded as useful: extrapolated data can not be verified.

In 2005, new results were presented comparing a new prototype and the previously used analytical model [23]. Two different flagella configurations were tested under a range ($5 - 15$ [Hz]) of operational frequencies. The experimental results match the theoretical predictions better than in [22]. There is no explanation given for why this is so. Furthermore, neither of the two flagella configurations in [23] are identical to the configuration used in [22] so a direct comparison is unavailable. Also, despite the range of frequencies tested, only 6 data points (3 for each flagella) are presented. Consequently, once again, the results of [23] should be regarded as suspect.

In the latest results (2006) presented by the Nanorobotics Lab [24], the researchers finally perform a complete RFT analysis of an eukaryotic flagella as outlined by Chwang and Wu (Sections 3.4.2 and 4.1.1). However, they compare this model, without acknowledgment, to their prototype, which is a replica of a prokaryotic flagella (Section 3.4.3). Brennen and Winet assert that the difference should be small when the cell body is relatively large [25]; however, the discrepancy should be accounted for in their discussion of the results. The specific comparison involves three new flagella configurations (when considering [22] and [23]). The results are such that the number two configuration matches the theoretical data very well while there is a large discrepancy between the number one and three configurations; even under a modified model that takes into account wall effects. No explanation is given for these discrepancies. Nor is any reference made to the results of [22] and [23]. Consequently, without further validation the results presented in [24] should be applied carefully.

In summary, the Nanorobotics lab has developed a rigid helical flagellum propulsion system. They have shown success in terms of functionality: the flagellum generates propulsive force when rotated. However, their ability to predict the system's performance using analytical modelling is not consistent.

These are likely to be the last papers presented by the Nanorobotics Lab on this system. The principal researcher's latest work represents a shift in focus. They have begun to look at developing a hybrid system where actual bacteria, rather than artificial flagella, are used to propel the robot [26].

2.3.2 L'École Polytechnique: Magnetic Levitation

Mathieu *et al* at L'École Polytechnique are looking at exploration of the circulatory system. Their goal is to use an Magnetic Resonance Imaging (MRI) machine to navigate a magnetically levitated probe through the arteries and veins. The project is labeled the MR-SUB.

Initial results have shown that the magnetic gradients generated by a MRI machine are strong enough to navigate a probe through larger blood vessels [27, 28]. The main challenge, however, was imaging the probe to ensure accurate position control. The researchers have presented some possible solutions [29], but also conclude that much work has to be done before a reliable solution is found.

2.3.3 Discussion

The two aforementioned projects represent pertinent work regarding *in vivo* exploration of the accessible systems of the human body. The MR-SUB has two major advantages. First, strong external magnetic fields mean the system is particularly well-suited to the circulatory system. Resisting the flow of blood requires large forces that would be difficult to achieve using internal actuation. Second, using existing infrastructure increases the attractiveness for potential buyers. However, for environments with quasi-static fluid flow, systems utilizing internal actuation should perform well. Given the already high demand for MRI machines in the health-care system, these options should be preferred.

The rigid helix propulsion system being developed at Carnegie Melon is one of these options. Despite the discrepancies in the model development, the system has been proven to create propulsive force and should be able to swim inside the human body. There is one major flaw though. An E.Coli bacteria's flagella is roughly 20 [nm] in diameter and 10 [μm] long. At this scale, it poses no threat to a human. However, when scaled up to facilitate the practicalities of current technology, a rigid helix turns into a needle. This poses a safety risk that is unacceptable.

As such, there still exists a need to develop a safe, simple propulsion system for a micro-robot for use *in vivo*.

2.4 Modelling of Cellular Propulsion Systems

The modelling of cellular propulsion systems is important to this work. Several analytical models such as the aforementioned RFT are used to model the proposed propulsion system. However, for the convenience of the reader it was determined that this information was best presented in Chapter 4.

Chapter 3

Design of a Propulsion System for Swimming *In Vivo*

This chapter outlines the design process undertaken to develop a propulsion system suitable for use inside the human body. This includes defining the need, outlining design constraints and criteria, evaluating possible solutions, and detailing a design concept.

3.1 Statement of Need

There exists today a trend toward technology miniaturization. Accordingly, the prospect of exploring the human body using micro-robots is an inevitability. Already exploration of the GI track is possible. It is speculated that the environments to be explored next will include the circulatory system, the respiratory system, the renal system, the eyeball, and the spinal chord. With the exception of the respiratory system, these environments are liquid-filled. Consequently, there exists a need to develop a safe, efficient propulsion system for swimming *in vivo*.

3.2 Design Constraints

The design constraints, as identified for the propulsion system, are given in this section. They are listed in qualitative terms, in keeping with the concept-design scope of the project.

3.2.1 Biocompatibility

Biocompatiblity, in a general sense, can be defined as the ability of a material or system to perform with an appropriate host response in a specific application. An appropriate response is dependent on the performance of the system or material with regards to four possible effects [30]. They are:

1. Cellular adhesion effects – does not adhere to cells unless designed to do so safely.
2. Local biological effects – zero disruption of cell mitotic functions and zero modification of normal healing. Does not cause infection, introduce toxicity, tumorigenisis, etc.
3. Systemic & remote effects – does not cause embolization of clots, allergic reactions, pyrogenic reactions, etc.
4. Effects of host on implant – does not disturb physical or mechanical effects, system stability, immune responses, etc.

Biocompatibility classification of medical devices is regulated by the country of use. Most countries use a class system to delegate restrictions on medical devices. The classes are set taking into account how the device is used (e.g. contact with skin vs. contact with blood) and the duration of use (e.g. minutes vs. hours). Regulation procedures change from country to country, however, often rigorous *in vitro* and animal model testing is required.

In contrast to a full screening based on Health Canada's regulatory requirements, this project uses a more general approach toward biocompatibility. At the system level, instances of planned device/tissue interaction are designed to be safe. Ideally, no evidence of the interaction will remain. The same ideal is desired for unintentional interactions. Validation of this criteria will require *in vivo* testing.

At the material level, biocompatibility will be ensured by using only chemically inert biomaterials. Over short periods of time – less than a month – these materials elicit minimal reaction when interacting with tissue. Over longer periods of time tissue encapsulation may be an issue [30]. Accordingly, these biomaterials should ensure biocompatibility for the propulsion system proposed.

3.2.2 Non-Biological Environment Compliance

There are six open volume systems in the human body that could be accessed by swimming micro-robots. They are:

- Circulatory system

- Gastrointestinal tract
- Renal system
- Lymphatic system
- Subarachnoid space (open space within spine)
- Eyeball

The circulatory system is the most dynamic of the environments. The constant flow within the system adds complexity to requirements of any propulsion system used. The changing viscosity of blood, depending on vessel diameter, adds further complexity. For these reasons, design for the circulatory system was discarded.

The other systems are compared in Table 3.1 to illuminate operating conditions. Accordingly, the device must be able to withstand acidic environments to a pH level of 2.0. It must also function in a specific gravity range of 1.0-1.03 and a fluid viscosity range of $1.0 - 4.0$ [cP ($mPa \cdot s$)].

Environment	**Dimensions**	**Specific Gravity**	**Viscosity (cP)**	**pH**
Water (Control)	n/a	1.0	1.0	7.0
Gastro-Intestinal				
Stomach	$50\ ml - 1\ l$	~ 1.008	~ 1.0	~ 2.0
Intestine	$> \phi 15\ mm$	~ 1.01	~ 1.0	5.8-7.6
Renal	$\phi 2.5\ mm$[1]	1.003-1.030	~1.2	4.5-8.0
Lymphatic	$\phi 4\ mm$[2]	1.012-1.023	~ 1.5	7.35-7.45[3]
Subarachnoid Space	$\phi 2.2\ mm$[4]	~ 1.005	~ 1.0	7.31-7.35
Eyeball	~ $\phi 22\ mm$[5]	~ 1.0	2.0-4.0	~ 7.0

Table 3.1: Comparison of viable *in vivo* environments [31–40]

The dominant factor imposed by *in vivo* environments is their scale. To access all the proposed environments, the robot must be able to fit into a tube 2.2 [mm] in diameter. This has large

---

[1] Based on current urethroscope technology.

[2] Based on the largest duct – the thoracic.

[3] Based on pH of blood.

[4] Accessible until thoracic region of spinal chord.

[5] Diameter of spherical volume.

consequences when one considers that all swimming systems are governed by the Reynolds number:

$$R_e = \frac{\rho U l}{\mu} \tag{3.1}$$

where ρ is the density of the fluid, U is the local velocity, l is a characteristic dimension[6], and μ is the fluid viscosity.

The Reynolds number is a dimensionless parameter that gives the ratio of inertial forces to viscous forces for a given object. Objects with a Reynolds number greater than one are in large Reynolds number flow and require inertia-based propulsion systems for swimming. Fish, boats, and humans, in water, fall into this category.

The scale of *in vivo* environments drives the characteristic dimension (l) down. If the swimming speed (U) is small enough, and viscosity (μ) is constant, viscous forces begin to dominate the system. Objects with a Reynolds number less than one are in low Reynolds number flow – inertial forces are negligible when compared to viscous forces. The situation can be described mathematically using the simplified Navier-Stokes equation [41]:

$$\triangledown p + \mu \triangledown^2 U = 0 \tag{3.2}$$

where p is the local pressure and U is the local velocity.

Since Equation (3.2) is free from time-dependent terms, the system is non-accelerating and the propulsive force is dependent on position only. Consequently, propulsion systems that utilize reciprocal motion — moving to and from a position by reversing steps — experience no net motion [41]. As such, the Reynolds number of the system dictates the type of propulsion system required.

To approximate the Reynolds number of an *in vivo* robot it is first assumed that the robot body is spherical. Accordingly, the characteristic dimension (l) for Equation (3.1) is the sphere's diameter ($2R$). Table 3.1 is then consulted. As mentioned, 2.2 [mm] is size limit of the body. To allow for an operating margin, a body diameter of 1 [mm] is chosen. The viscosity (μ) is set at 1.0 – 4.0 [$mPa \cdot s$], and the fluid density (ρ) is 1000 [kg/m^3] (i.e. specific gravity of 1.0). Therefore, the Reynolds number is determined by the swimming velocity (U) of the system. At first this value would seem arbitrary. However, if one uses natural systems as inspiration, Bejan and Marden claim that locomotion velocity can be roughly approximated by applying their unified theory for scale effects in running, swimming, and flying [42]. This theory is developed by finding the optimal balance between the vertical loss of useful energy, and the horizontal loss caused by friction against the surrounding medium.

---

[6] Often diameter or length.

To apply the theory the robot body mass (M_b) must be approximated. The density (ρ_b) of the body is assumed equal to water to ensure neutral buoyancy (Section 3.3). Accordingly, the mass of the body, using the spherical body assumption, is:

$$M_b = \rho \frac{4}{3} \pi R^3. \tag{3.3}$$

The mass, body density, and gravity (g) are then used to calculate an approximation for optimal[7] swimming speed (U_{opt}) according to the relationship proposed by Bejan and Marden:

$$U_{opt} \sim g^{1/2} \rho_b^{-1/6} M_b^{1/6}. \tag{3.4}$$

Given Equation (3.4), an rough estimate for the Reynolds number is solved for using Equation (3.1). The result is that $R_e \sim 22 - 88$. Unfortunately, fluid behaves unpredictably in this range of Reynolds numbers [43]. The system scale must be modified so that the Reynolds number pertains to a better understood flow situation. Therefore, the system is scaled down until ($Re < 1$) thus ensuring laminar or low Reynolds number flow. Consequently, to fulfill the need outlined in Section 3.1, a propulsion system tailored for use in low Reynolds number flow is required.

3.3 Design Criteria

The following design criteria have been identified for this project:

- Neutrally Buoyant – The overall specific gravity of the system should be close to 1.0 (Table 3.1) to neutralize the effects of gravity and buoyancy thus eliminating the need for ballasts. The narrow specific gravity range of the surveyed biofluids (Table 3.1) allows for the system to be neutrally buoyant in all accessible environments.
- Speed – To decrease the invasiveness of the device, the propulsion system should move as fast as possible. However, this criteria is balanced with the power requirements of the system. The IMC has concluded that their active capsule endoscope should be able to navigate the 9 [m] GI tract in roughly 2 hours [10]. To do so, the device must move at approximately 1 [mm/s].
- Low power requirements – Low power requirements allow for wireless power transmission. This eliminates battery life restrictions. Wireless power transmission is a developing technology; however, order of magnitude calculations suggest that several hundred microwatts could be available [31].
- Efficiency – Efficiency is a goal from a sustainability and wise-use point of view.

---

[7] Order of magnitude accuracy.

- Size – The required scale poses issues for manufacturing and assembly. It is speculated that larger components will be easier to manufacture and handle. Accordingly, the robot should be as large as possible.
- Simple – Inherent simplicity will help render issues with manufacturing and assembly more manageable. For instance, a simple mechanisms using few parts is favoured over a complex mechanism.

3.4 Biological Low Reynolds Number Propulsion Systems

The inability of the system to utilize inertia-based propulsion automatically eliminates traditional large-scale propulsion systems such as a boat propeller. However, low Reynolds flow propulsions systems exist in nature and can be drawn upon for inspiration. They are presented in this section along with short analyses regarding the feasibility of transferring the concepts to a man-made propulsion system.

As a brief background: eukaryotic single-cell organisms contain a distinct nucleus and other complex organelles bound by membranes. They are part of the domain Eukaryotae which also contains plants, animals, and fungi. On the other hand, prokaryotic cells do not contain distinctive membranes. They are most often bacteria and are generally much smaller than eukaryotic cells [2].

3.4.1 Eukaryotic Ciliary Beating

Cilia are cytoplasmic appendages found on eukaryotic cells. They mostly occur in densely-packed groups of thousands moving in coordination to propel the cell [44].

Each cilia's general composition consists of an outer ring of microtubule doublets surrounding a pair of central tubules. The tubule doublets are connected to the central tubules by radial spokes and to the other doublets via dynein arms [44].

The motion of the cilia is facilitated by the microtubule's ability to slide over one another. When powered by adenosine triphosphate (ATP), the dynein bridge is broken and the dynein molecule undergoes an orientation change that causes sliding between doublets. Repetition of the process ensures that sliding continues as required. Non-reciprocal motion is created by a beating motion that can be separated into two distinct phases (Fig. 3.1). Phase one, or the effective stroke, sees the ciliary shaft bend primarily at its base while the rest of the cilia remains relatively straight. During the second phase, or recovery stroke, the cilia returns to the start position by the propagation of a slow bend from the base to the tip. The effective stroke is the

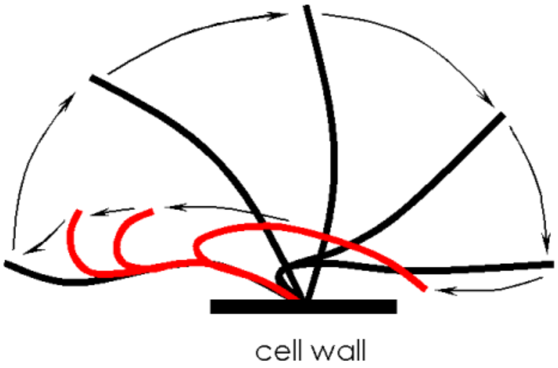

Figure 3.1: Cilia Stroke Cycle (Recreated from [44])

more propulsive of the two and as such dictates the direction of net motion [44].

From an engineering standpoint, ciliary propulsion is difficult to replicate. The ability to actively generate bending at specific locations along the length of the appendage using current materials is incredibly challenging. The requirement for large numbers adds additional complications. Therefore, other options for low Reynolds number propulsion systems are explored.

3.4.2 Eukaryotic Flagella

Eukaryotic flagella are similar to cilia. They have the same microtubule composition and motion inducing sliding mechanism [44]. Scale is the main difference between the two. Whereas cilia are generally $2 - 20$ [nm] long, flagella are generally $100 - 200$ [nm] long. Additionally, cilia generally occur in vast numbers while flagella occur in smaller numbers [44].

The other difference is in the pattern of movement. Instead of a reciprocating stroke cycle, the eukaryotic flagella generates propulsive force by propagating a wave down its length. This wave can either be planar or helical in nature. The planar wave is more efficient and, consequently, more prominent [45]. The waves propagate down the length of the flagella at a frequency of 20-30 per second [44]. The presence of a moving wave rather than a standing wave ensures that the system exhibits non-reciprocal motion.

Like the cilia, the internal actuation required in a planar flagella causes difficulties from an engineering point of view. Therefore, it is once again recommended that other propulsive options be explored.

3.4.3 Prokaryotic Flagella

Prokaryotic flagella are quite different from eukaryotic flagella. First, the prokaryotic flagellar filament is made of 20,000 to 30,000 flagellin protein molecules polymerized into a helical tube structure. Second, due to its composition, the helical structure is essentially rigid. Third, actuation of the filament is facilitated by a rotary motor embedded in the cellular wall rather than along the filament itself. The flagellar filament is attached to the motor via a flexible 'hook' that emulates a universal joint. The handedness of the helix ensures that the system undergoes non-reciprocal motion [44].

The prokaryotic flagella is the most similar to engineered systems. The filament can be regarded as a rigid structure while the biological motor – complete with a stator and rotor – is virtually identical to electrical motors. Consequently, it is recommended that this system be used as inspiration for the propulsion system required.

3.5 Design Options

Based on the prokaryotic flagella, several propulsion concepts were considered. They are outlined here. A decision matrix comparing the possible solutions follows.

3.5.1 Rigid Helical Flagellum

This solution involves closely recreating the prokaryotic flagella by attaching a rigid helix to a rotary actuator. This simplicity of this solution makes it attractive. One manufacturing method is to form the rigid helix from a piece of correctly sized wire. Another proposal is to grow the helix as a carbon nanotube [21].

As mentioned in Section 2.3.1, there is a possibility that this design could violate the safety design constraint. Early versions of this system would be as large as possible to increase their feasibility. At that scale however, the rigid helix would have a diameter of roughly 0.1 [*mm*]. This equates to having a needle inside the body. Accordingly, the rigid flagellum solution is only viable if the helix is small enough to not create a piercing threat inside the body.

3.5.2 Compliant Helical Flagellum

This design incorporates compliance into a helical flagellum to reduce the piercing threat. To do so, the helix is molded out of a biocompatible elastomer. The geometry and stiffness of the material are balanced such that, under swimming loads, the helix is shaped as desired. Under impact loads, the helix flexes to absorb enough energy to eliminate the piercing threat.

The disadvantages of this option are twofold. First, molding adds a level of complexity to the manufacturing process. Second, to always prevent piercing, the balance point between operational loads, body stiffness, and impact loads must be found. This requires a full characterization of all possible loads which, would require rigorous testing or modelling of *in vivo* conditions. Consequently, the engineering process required to create a feasible compliant helical flagellum would be complicated.

3.5.3 Flexible Filament

The flexible filament solution provides a greater level of protection from piercing. The premise is that under rotational load, a flexible filament, specifically shaped, will contort into a helix as a result of the drag forces it is subjected to. Since the filament is operating away from static equilibrium, impact forces at the tip of the filament are not resisted. Instead the filament simply bends out of the way. At equilibrium, the slenderness of the filament is such that axial forces – as required to pierce tissue – will cause the filament to buckle rather than cause damage.

The flexible filament also has disadvantages. First, like the compliant helix, molding is required. Second, functionality is lost in that the filament cannot swim both forwards and backwards; contorting the filament into a helix allows for forward propulsion only. Third, like the compliant helix design, the flexible filament has a more involved engineering process. The rotational loads must be balanced with the body stiffness to ensure a proper helix forms. However, since impact loads are not part of this balance, the flexible filament is, from an engineering standpoint, simpler than the compliant helix.

3.5.4 Decision Matrix

The following decision matrix compares the compliant helix design to the flexible filament design. The rigid helix design was discarded because of its inability to ensure safety *in vivo*. However, the rigid helix design is considered when assigning values to the other two designs. The safety criteria is specific to the design's piercing threat; all other aspects of biocompatibility are assumed equal. Manufacturing pertains to ease of manufacturing for medium scale production runs. Functionality is related to the design's ability to propel the robot both forwards and backwards. The mechanism and engineering simplicity criteria are an attempt to measure reliability at two levels. The former speculates that performance reliability is influenced by the complexity of

Criteria	Weight	Compliant Helix	Flexible Filament
Safety	3	2(3)=6	3(3)=9
Manufacturing	1	1(1)=1	1(1)=1
Functionality	1	1(3)=3	1(2)=2
Mechanism Simplicity	2	2(3)=6	2(3)=6
Engineering Simplicity	2	2(1)=2	2(2)=4
Total		18	22

Scoring: 1 = Low, 2 = Medium, 3 = High

Table 3.2: Decision Matrix

the final drive system. The latter speculates that performance is related to the complexity of the design from an engineer standpoint. In other words, the more complex the design calculations, the more that could go wrong. Based on Table 3.2 the flexible filament design was chosen. In the following section the design will be explained in more detail.

3.6 Proposed Design

An overview of the final concept is given in Figure 3.2. It consist of a large robot body driven by a single flexible filament. The details of the filament are well-defined and are presented in the sections that follow. The internals of the body, unless pertinent to propulsion, are not considered as is in line with the project scope.

To ensure biocompatibility, the materials used are safe for use *in vivo*. All metal parts are designed to be titanium, while the filament is made of silicone elastomer [30]. These materials are chemically inert inside the body. Their ability to withstand pH levels of 2.0 is unknown and must be determined as part of future work.

3.6.1 Design Constraints Required to Form a Helix

There are three design constraints required to form a helix from a filament under rotational load. First, a balance between viscous forces and body stiffness must be achieved. Inertial forces will be present but are considered negligible (Equation (3.2) in Section 3.2.2). Viscous forces act to curl a body about the axis of rotation. Inertial forces act to fly a body away from the axis of rotation. Stiffness resists body deformation from equilibrium. A steady-state helix will be created under rotation load at the point where the viscous forces curl the body at an equal but opposite magnitude to the resistance offered by the body stiffness.

One possible solution is to tune the material spring constant against the system velocity so that the required balance occurs at the point desired (Fig. 3.3). This requires that the forces on the flagellum be well understood and remain constant for all environments and situations. The narrow operating margin of this situation makes the solution non-ideal.

Another solution is to discretize the helix into a series of relatively rigid sections attached via flexure pivots. Over-curl is prevented by hard stops in the geometry of each pivot (Fig. 3.4 and 3.3). Although functional, a discretized flagellum is ultimately undesirable for two reasons. First, general flexibility is lost with the addition of relatively rigid sections. Second, stress concentrations at the flexure pivots are expected to increase the chances of fatigue failure compared to smooth filaments.

The last solution involves designing a material geometry that displays a two-stage elastic stiffness response at all sections of the flagellum. The first stage provides little resistance to curl. The second stage, tuned to activate at the desired angle of deflection, drastically stiffens the material to prevent further curl (Fig. 3.3). This solution reduces the chance of fatigue failure while allowing for a wide operating margin. It is recommended that further research be conducted to design a geometry/material combination capable of displaying the required two-stage response.

The second requirement of helix formation is that the helix must be prevented from collapsing upon itself along the axis of rotation. If this happens, the three-dimensional helix collapses into a two-dimensional spiral. The solution is to limit the degrees of freedom of the filament. As another requirement of the tail geometry, bending must be heavily predisposed to a predetermined axis. The orientation of this axis twists as one travels down the length of the filament. As mentioned, the amount of allowable bending is controlled by the two-stage elastic response of the material about the predisposed axis.

With these provisions in place, the filament is, in essence, a infinite series of rigid links attached by one degree of freedom revolute joints. As a system then, the flagellum may only transform from a straight line to the helix desired — no over-curling or collapsing may occur.

The third requirement is that the base of the helix must resist the rotational reaction loads transferred to it. If the base cannot do so the balance required for the first condition can never be achieved. The head of the micro-robot is the base of flagellum and must therefore resist the reaction loads. This is accomplished by having sufficiently large drag forces. Unfortunately,

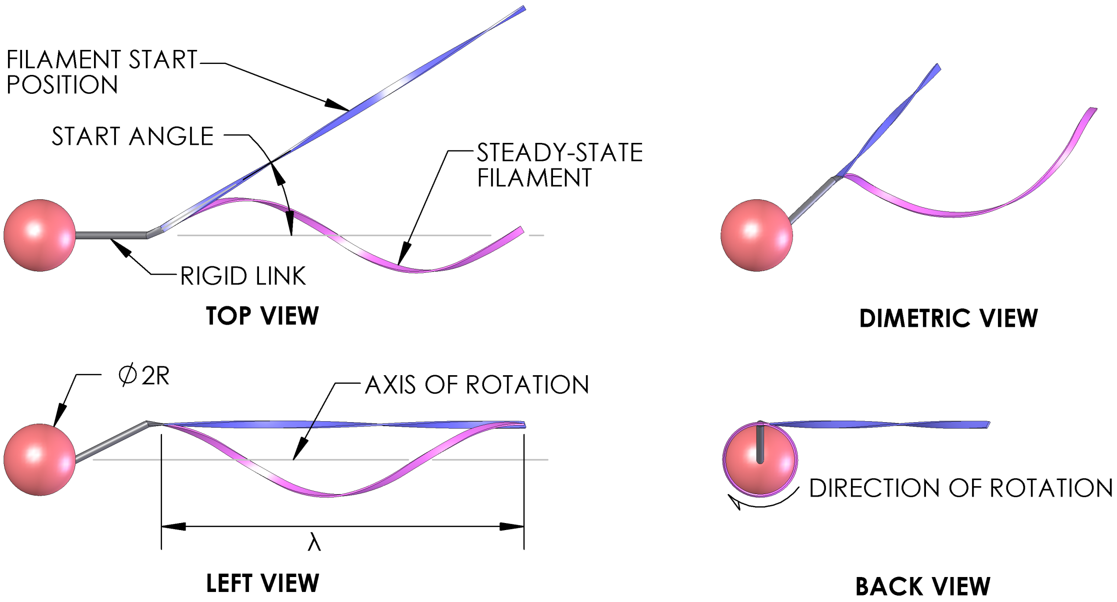

Figure 3.2: Artist Conception of Proposed Design

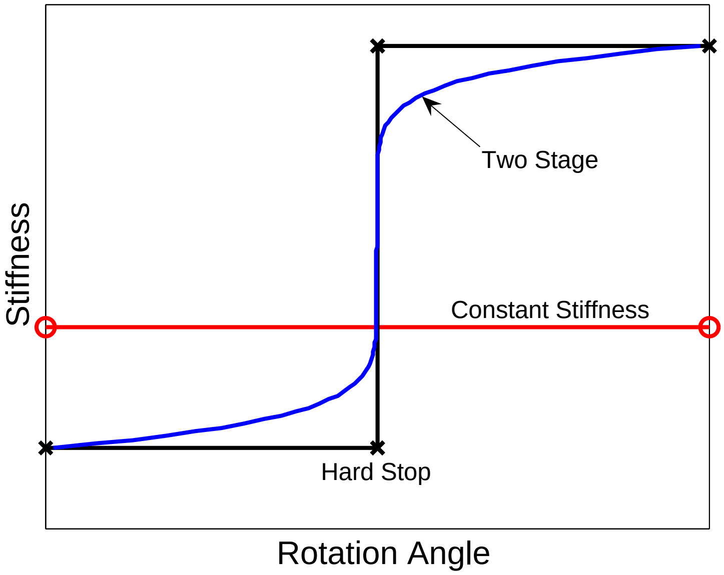

Figure 3.3: Possible stiffness profiles

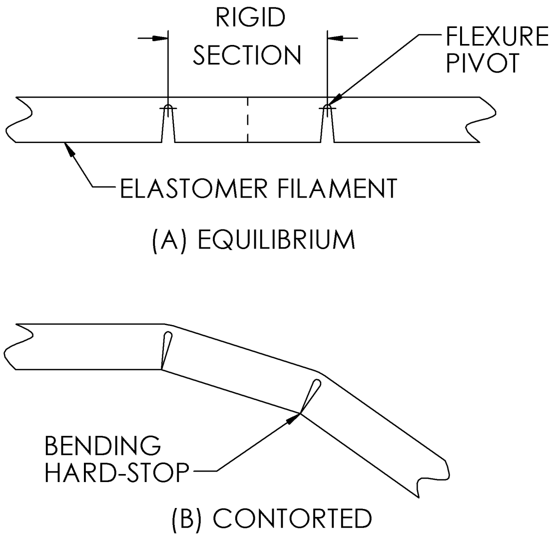

Figure 3.4: (A) Flexure pivot filament at equilibrium (B) flexure pivot filament contorted to hard-stop limit

in low Reynolds flow, drag forces can be assumed proportional to velocity [1]. Therefore, a robot head must be designed that allows adequate swimming velocities while providing enough resistance to form a steady helix.

3.6.2 Helix and Filament Parameters

The parameters that describe the engineered propulsion system are inspired by biological systems. This section outlines the derivation of these parameters.

A helix is described by its amplitude (b), wavelength (λ), and filament radius (a). A visual representation is given in Figure 3.5. Mathematically, a single turn of the a helix is described as:

$$\begin{aligned} x &= b\cos\theta \\ y &= b\sin\theta \\ z &= \frac{\lambda}{2\pi}\theta \end{aligned} \tag{3.5}$$

for $\theta \in [0, 2\pi\}$.

Generally prokaryotic flagella exhibit the following values for these parameters: $\lambda = 2.5$ [μm], $b = 0.25$ [μm], $a = 10$ [nm] [46]. Non-dimensionally, these values become $\Pi_1 = \lambda/b = 10$ and $\Pi_2 = a/b = .04$.

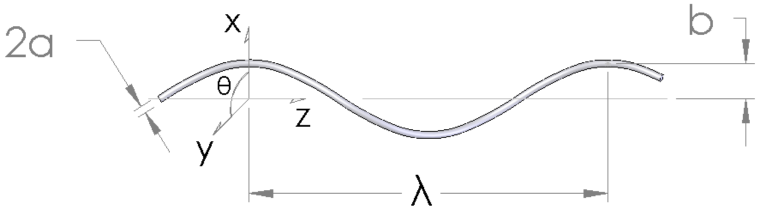

Figure 3.5: Helix parameters

The efficiency of a helical flagella is defined by its geometry. In his work on analytical modelling of a flagellum (Section 4.1.2), Lighthill also investigated flagellar efficiency [2]. The culmination of the investigation is the relative efficiency chart seen in Figure 3.6. The helix centreline wavelength (Λ) – the curve distance (s) of a single wave – is defined as:

$$\Lambda = \sqrt{\lambda^2 + 4\pi^2 b^2}. \tag{3.6}$$

Given (3.6) and the biological helix parameters, generalized biological systems can be evaluated such that $\Lambda/a \approx 150$ and $2b/\lambda = 0.2$. It should be noted that, in terms of Figure 3.6, a typical prokaryotic flagella could be more efficient. However, Lighthill's model is generated assuming only a helix and no body. Adjustments to allow for the presence of a head may – or may not – shift biological systems into an optimal efficiency state. Regardless, for this work, an assumption is made that biological systems perform their function well. Accordingly, a man-made system with similar dimensionless ratios will in turn function well.

Another ratio to consider is the swimming velocity of a prokaryotic specimen with respect to its body diameter: $n = U/2R$. This value can vary from $1 - 100$ $[s^{-1}]$ in nature [25]. For this work, the value of n varies from $1 - 10$ $[s^{-1}]$. To ensure low Reynolds flow (Section 3.2.2), the Reynolds number can be set at a maximum of one. Together, these modifications allow Equation (3.1) to be rewritten as:

$$2R < \sqrt{\frac{\mu}{\rho n}}. \tag{3.7}$$

A plot of Equation (3.7) shows that the largest possible body diameter ($2R$) is approximately 1 $[mm]$ (Fig. 3.7). This value is chosen, despite the swimming velocity trade-off, because it will ease in eventual manufacturing of the robot body.

The robot will function mainly in tubular environments, therefore, it is desirable that the helix not extend past the body. Accordingly, the helix amplitude is set at $b = 0.5$ $[mm]$. Using Π_1 and Π_2 directly, $\lambda = 5$ $[mm]$ and $a = 0.02$ $[mm]$. Due to anticipated manufacturing difficulties, the

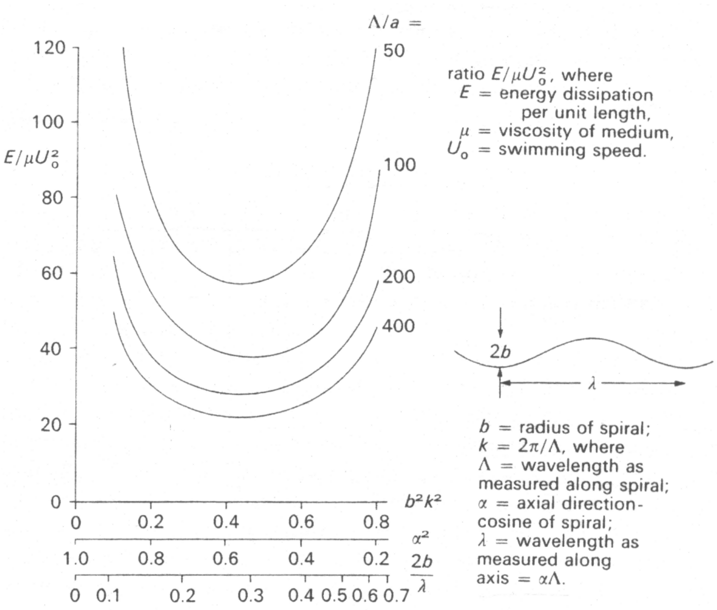

Figure 3.6: Efficiency of helical flagella free from a cell body (Lighthill, J., "Flagellar Hydrodynamics", *SIAM Review*, Vol. 18, Figure 12 (pp. 203), pp. 161-230, 1976, Copyright © Society for Industrial and Applied Mathematics. Reprinted with permission.)

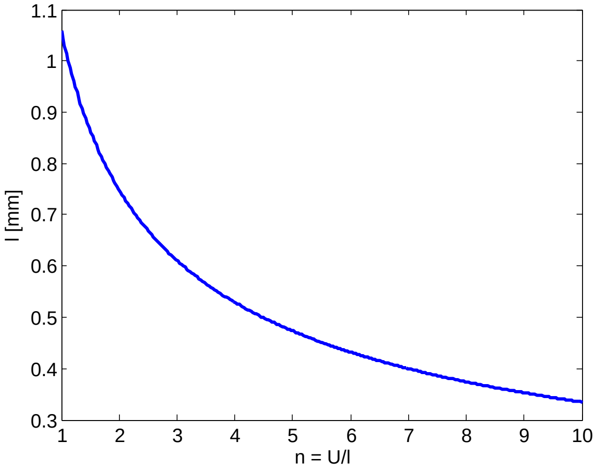

Figure 3.7: Body size versus swimming velocity with respect to body length

filament radius (a) is increased such that $a = 0.06$ [mm]. This change is speculated to have a minimal effect on performance.

These parameters, when mapped to Figure 3.6 correspond to an non-dimensional efficiency value of approximately 42. The typical prokaryotic flagellum – as outlined previously – has a non-dimensional efficiency of 38. Accordingly, the flexible filament should require approximately 10% more power than biological systems.

With the helix parameters determined, the flexible filament can be designed. First, using (3.6), the length of the filament is calculated as 5.9 [mm].

Second, to ensure that bending is predisposed to a specific axis, the filament is given a rectangular cross-section. The filament has a width of $w = 0.125$ [mm] and a height of $h = 0.0625$ [mm]. These values are chosen because they maintain a consistent surface area with a 0.12 [mm] diameter cylinder. Since low Reynolds number flow is dominated by viscous surface friction [43], it is hoped that by keeping a constant surface area the drag forces will be similar.

It is speculated that to make a consistent helix shape, a thinning taper may be required down the length of the helix. This is to account for the superposition of loads along the filament length. In other words, loads experienced at the tip are compounded up the length of the filament. The requirement for a taper is investigated during the modelling phase of the project (Chapter 4).

Third, the required twist in the filament is determined by calculating the torsion of the helix. The torsion of a space curve is defined by the rate of change of its osculating plane. A curve is planar if its torsion is equal to zero and it has non-zero radius of curvature [47]. The torsion of a helix is defined as:

$$\tau = \frac{2\pi\lambda}{4\pi^2 b^2 + \lambda^2}. \tag{3.8}$$

For the system proposed the torsion of the desired helix equates to $\tau = 900.95$ [m^{-1}]. Accordingly, the number of turns along the length of a filament is:

$$\frac{\tau\Lambda}{2\pi} \tag{3.9}$$

which, for the proposed filament, equals 0.847 turns.

Fourth, the stiffness of the material is set so that the filament curves appropriately (Section 3.6.1). Therefore, the filament should bend to match the radius of curvature of the desired helix as described by:

$$R_c = b + \frac{\lambda^2}{4\pi^2 b}. \tag{3.10}$$

For the system proposed the radius of curvature of the desired helix equates to $R_c = 1.767$ [mm]. Tuning the material stiffness to match this value depends on the drag loads experienced by the filament. These forces are not available at this stage of the design process. Accordingly, further investigation is carried out during the modelling phase of the project (Chapter 4).

Lastly, the starting angle of the filament with respect to the rigid link is required. This value is simply the pitch angle of the helix:

$$\tan\beta = \frac{2\pi}{\lambda}b = kb. \tag{3.11}$$

For the desired helix $\beta = 32.14°$.

3.6.3 Actuation

Actuation of the flagellum can be accomplished by one of two solutions. The first is direct actuation via a simple rotary actuator such as a motor. Coupled to the motor is a rigid link that places the beginning of the flexible filament at the desired position and angle (Fig. 3.2). When the motor is on, the helix base scribes the desired circle.

The second solution is based on the premise of wobble plate pumps. A wobble plate is actuated by a circular array of linear actuators. The flagellum rigid link contacts the wobble plate. The linear actuators are synchronized to move the wobble plate such that the base of the helix travels as required. The main advantage of this system is that the linear actuators allow for variability within the wobble plate. Consequently, the rotation of axis for the rigid link can be changed within the confines of the system. It is conjectured that this could be used for steering the robot.

It should be noted that these solutions are concepts and are not designed in full like the filament. However, as a goal of this project, approximate power requirements for any method of actuation will be acquired.

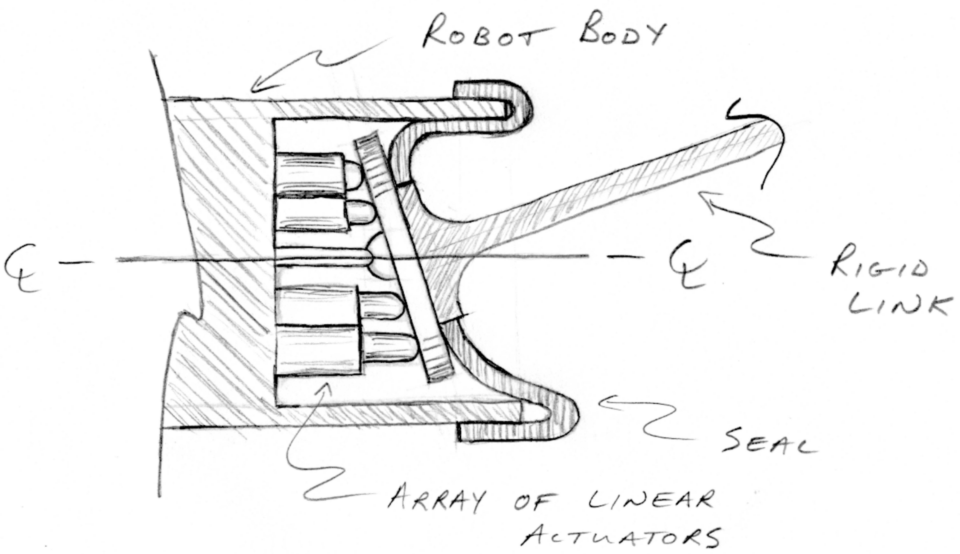

Figure 3.8: Wobble plate actuation system concept

Chapter 4

Modelling & Analysis

To assess the feasibility and performance characteristics of the propulsion system design proposed in Chapter 3, several models are created. This chapter outlines those models and analyzes the results to determine if the propulsion system is viable.

4.1 Analytical Modelling

In 1955 Gray and Hancock penned the pioneering paper on the hydrodynamics of flagellar propulsion [1]. In it, they developed Resistive-Force Theory (RFT), which states that hydrodynamic forces are proportional to the local body velocity, with the constant of proportionality defined as the resistive coefficient. Gray and Hancock's work was widely adopted by the academic community and was subsequently used to model a variety of biological [48–50] and man-made [22] systems.

However, a simplification in resistive-force theory adds uncertainty to any results obtained. RFT relates the velocity of each segment of a flagellum to only the local drag force acting on that element. However, as Lighthill points out, the true hydrodynamics create a situation where the velocity of a flagellum segment is affected not only by the drag on it, but also by the forces exerted on it by the rest of the flagellum [2]. To account for this, Lighthill attempted to model the true hydrodynamics of flagellar propulsion and derived his own model.

Resistive-force theory and Lighthill's model, despite their limitations, provide a good approximation of the performance of a helical propulsion system. Furthermore, later in this chapter computer models are developed to investigate the transient behaviour of the flexible filament propulsion system. It is hoped that the analytical models can be used to validate the computer-based models.

4.1.1 Resistive-Force Theory

Resistive-force theory is developed by considering a small element of flagellum moving under low Reynolds number flow conditions through a Newtonian fluid. Gray and Hancock theorized that the reaction forces could be regarded as proportional to the velocity of the element and the viscosity of the medium [1]. Accordingly, if the tangential and normal velocities of a cylindrical element of length ds are $\mathbf{V}_s$ and $\mathbf{V}_n$ respectively, the tangential (dF_s) and normal (dF_n) viscous forces are:

$$dF_s = -C_s V_s ds, \tag{4.1}$$

$$dF_n = -C_n V_n ds, \tag{4.2}$$

where C_s and C_n – the resistive coefficients – are defined as:

$$C_s = \frac{2\pi\mu}{ln\frac{2\lambda}{a} - \frac{1}{2}},\ C_n = \gamma C_s, \tag{4.3}$$

where λ is the helix wavelength, a is the filament radius, μ is the fluid viscosity, and γ is the ratio of C_n/C_s. The value for γ initially proposed by Gray and Hancock is 2. Gray and Hancock validated resistive-force theory and their proposed resistive coefficients by comparing their model with the behaviour of sea-urchin spermatozoa [1]. The result was that almost no difference ($\sim$ 1%) existed between the natural system and their analytical model. Embracement of the theory by the academic community followed their success. Researchers began modelling other biological organisms and refining the resistive coefficients. Brokaw suggested that a more appropriate value for γ is 1.8 [51]. Lighthill proposed, for systems with helical waves, that the resistive coefficients are [2]:

$$C_s = \frac{2\pi\mu}{ln\frac{2q}{a}},\ C_n = \frac{4\pi\mu}{ln\frac{2q}{b} + \frac{1}{2}}, \tag{4.4}$$

where $q = 0.09\Lambda$ or 9% of the centreline wavelength of the helix (Λ). For this thesis, Lighthill's relationships are used because they are defined for the helical motion utilized by the proposed flexible filament propulsion system.

It should be noted that, for a flagella based propulsion system, propulsion is created for two reasons. The first, outlined in Section 3.2.2, is the presence of non-reciprocal motion. The other is an inequality between normal and tangential drag as quantified by γ [1]. Consequently, γ can be considered loosely proportional to swimming efficiency. Therefore, if γ can be increased in

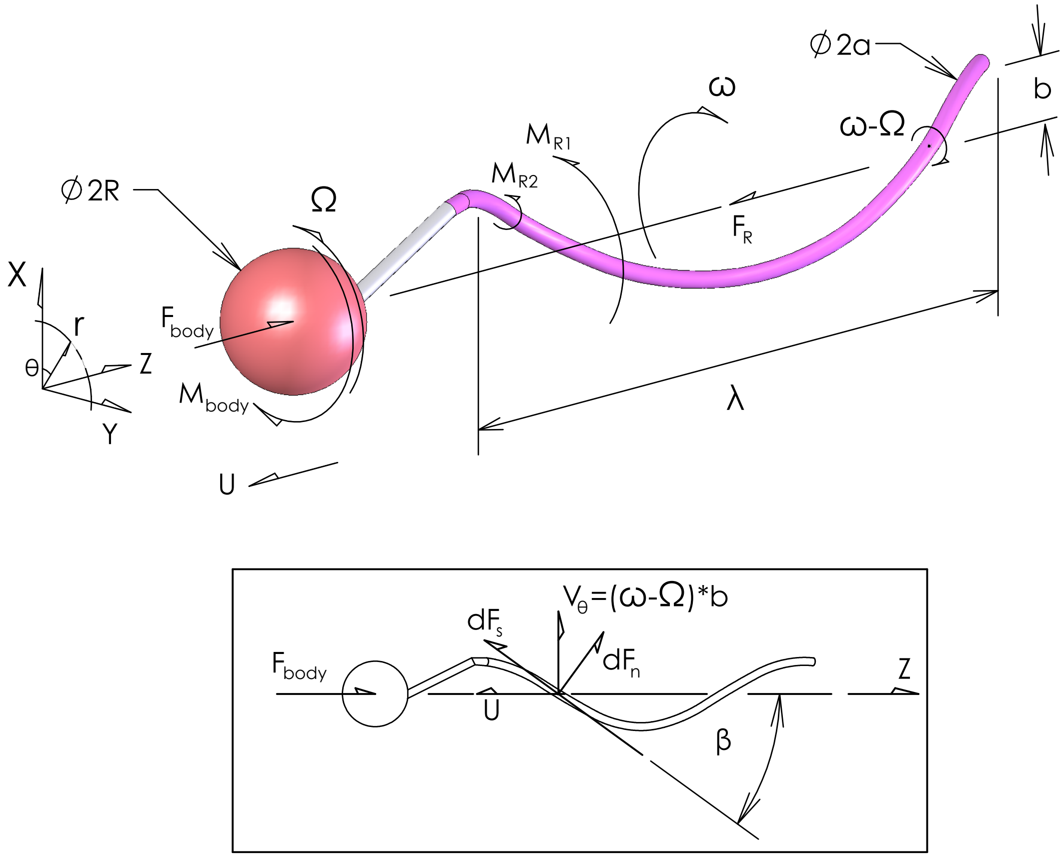

Figure 4.1: Model Layout

man-made systems, efficiency could increase. It is recommended that different filament cross-sections be explored to try and exploit this.

Resistive-force theory is applied to a system by performing a force balance. A modified version of the method originally presented by Chwang and Wu [50] for systems with helical flagella is given here. Consider the system shown in Figure 4.1. The model is defined such that the tail rotates, with respect to the body, at ω $[rad/s]$. The body rotates about the z-axis at Ω $[rad/s]$. The body travels at velocity U $[m/s]$ along the z-axis. It is assumed that the body is constrained such that all other degrees of freedom are eliminated. Therefore, neglecting forces due to acceleration, the force balance is:

$$+\rightarrow \quad \sum F_z = 0 = F_{body} - F_R, \tag{4.5}$$

$$+\circlearrowleft \quad \sum M_z = 0 = M_{body} - \sum M_R = M_{body} - M_{R1} - M_{R2}. \tag{4.6}$$

where, for an element on the helix, the force in the z-direction is:

$$dF_R = dF_n \sin\beta - dF_s \cos\beta. \tag{4.7}$$

While the force in the θ-direction can be coupled with the helix amplitude to give a torque about the z-axis:

$$dM_{R1} = -(dF_n \cos\beta + dF_s \sin\beta)b, \tag{4.8}$$

where β is the constant pitch-angle between the helix and the z-axis as defined in Equation (3.11). It is defined again here:

$$\tan\beta = \frac{2\pi}{\lambda} b = kb. \tag{3.11}$$

An additional torque results from drag on the filament as it rotates about the tangent of its centreline. At this point the force balance varies from the work done by Chwang and Wu. Their derivation pertained to eukaryotic organisms exhibiting undulatory helical waves. In these systems, the helix rotates about the the tangent of its centreline at a rate of $\Omega \cos\beta$ $[rad/s]$. This work focuses on a rigid helix being rotated at its base. Consequently, the filament rotates about the tangent of its centreline at a rate of $(\omega - \Omega)\cos\beta$ $[rad/s]$. This difference is illustrated in Figure 4.2. Given the rotation rate of the tail about the tangent of its centreline the viscous reaction torque (dM_s) exerted on the tail is [50]:

$$dM_s = -4\pi\mu a^2 (\omega - \Omega)\cos\beta ds. \tag{4.9}$$

The z-component of this torque (dM_{R2}) is:

$$dM_{R2} = -4\pi\mu a^2 (\omega - \Omega)\cos\beta dz. \tag{4.10}$$

Brennen and Winet claim that the torque difference caused by dissimilar rotation rates between eukaryotic and prokaryotic flagellum will likely not make a large difference in the accuracy of an RFT model [25]. This claim is investigated in the analytical modelling results section (Section 4.1.3).

Using the simplified spherical body shape shown in Figure 4.1, with radius R, the drag forces influencing the body are [50]:

$$F_{body} = -6\pi\mu R U, \tag{4.11}$$

$$M_{body} = -8\pi\mu R^3 \Omega. \tag{4.12}$$

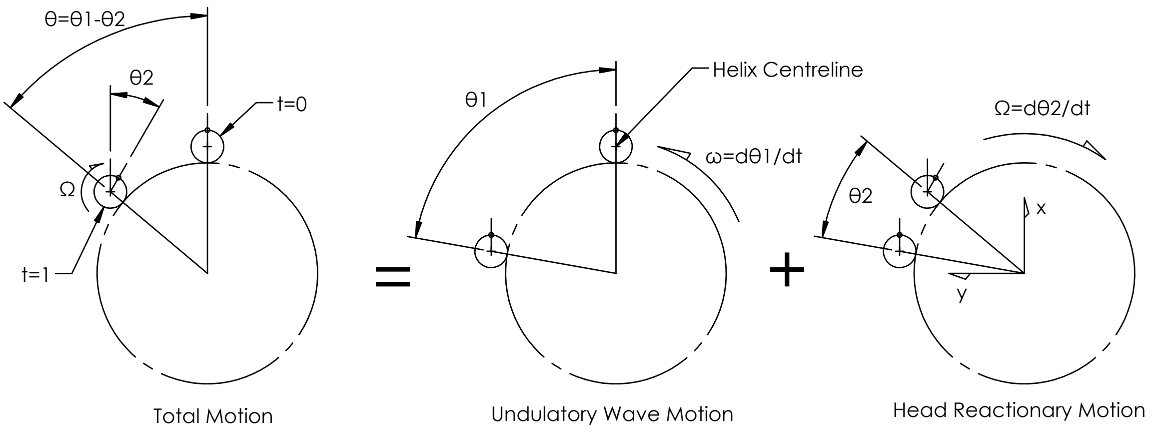

(a) Undulatory Helical Wave Form

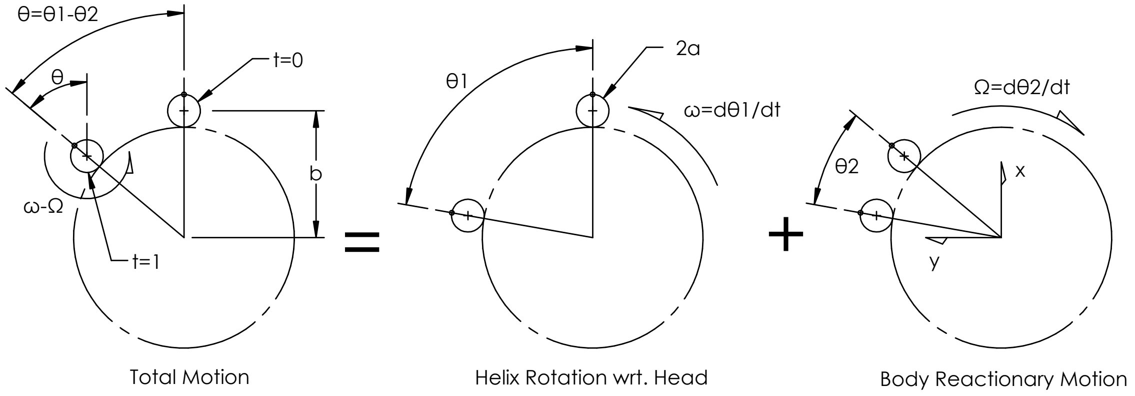

(b) Rigid Helix

Figure 4.2: (a) Relative positions of a section of tail exhibiting undulatory helical wave propagation a unit time apart (b) Relative positions of a section of rigid helical tail under simple rotation a unit time apart (Part (a) recreated from [50]).

Given the forces and moments on the system, the equilibrium conditions, equations (4.5) and equations (4.6), become:

$$0 = -6\pi\mu RU - \int_0^{\lambda} (dF_n \sin\beta - dF_s \cos\beta) = 0, \tag{4.13}$$

$$0 = -8\pi\mu R^3\Omega + b\int_0^{\lambda} (dF_n \cos\beta - dF_s \sin\beta) + \int_0^{\lambda} 4\pi\mu a^2 (\omega - \Omega)\cos\beta dz. \tag{4.14}$$

Additionally, referring back to Figure 4.1, it can be seen that equations (4.1) and (4.2) become:

$$dF_n = C_n \left[b(\omega - \Omega)\cos\beta - U\sin\beta \right] \sec\beta dz, \tag{4.15}$$

$$dF_s = C_s \left[b(\omega - \Omega)\sin\beta + U\cos\beta \right] \sec\beta dz. \tag{4.16}$$

In turn, when substituted with Equation (3.11), the relationship $C_n = \gamma C_s$, and the relationship $\omega = kc$, the equations above become:

$$dF_n = \gamma C_s \left[(kc - \Omega)b - Ukb \right] dz, \tag{4.17}$$

$$dF_s = C_s \left[(kc - \Omega)kb^2 + U \right] dz, \tag{4.18}$$

where $k = 2\pi/\lambda$ and c is the phase velocity of the wave down the helix. Equations (4.17), (4.18), (4.11), and (4.12) can then be substituted as required into equations (4.13) and (4.14) to generate two simultaneous linear equations for two unknowns U and Ω:

$$\left(1 + \gamma\kappa^2 + \mathsf{A}\right) U + (\gamma - 1)\kappa\Omega b = (\gamma - 1)\kappa^2 c, \tag{4.19}$$

$$(\gamma - 1)\kappa U + \left(\gamma + \kappa^2 + \mathsf{B}\right)\Omega b = \kappa\left(\gamma + \kappa^2 + \mathsf{C}^*\right) c, \tag{4.20}$$

where,

$$\kappa = kb, \tag{4.21}$$

$$\mathsf{A} = \frac{3\mu\kappa}{C_s}\left(\frac{R}{b}\right)\sqrt{1 + \kappa^2}, \tag{4.22}$$

$$\mathsf{B} = \frac{4\mu}{C_s}\left[\pi\left(\frac{a}{b}\right)^2 + \left(\frac{R}{b}\right)^3 \kappa\sqrt{1 + \kappa^2}\right], \tag{4.23}$$

$$\mathsf{C}^* = \frac{4\pi\mu}{C_s}\left(\frac{a}{b}\right)^2. \tag{4.24}$$

Solving for U gives:

$$U = \frac{(\gamma - 1)\kappa^2 c\,(\mathsf{B} - \mathsf{C}^*)}{(1 + \gamma\kappa^2 + \mathsf{A})(\gamma + \kappa^2 + \mathsf{B}) - \kappa^2(\gamma - 1)^2}, \tag{4.25}$$

which, can then be used to solve for Ω using either Equation (4.19) or (4.20). Back-substitution of U and Ω allows for the propulsive force (F_R) and the required driving torque ($M_R = M_{R1} + M_{R2}$) to be solved for:

$$F_R = \frac{C_s\lambda\left[(\gamma - 1)\kappa^2 c - (\gamma - 1)\kappa\Omega b - (1 + \gamma\kappa^2)U\right]}{\sqrt{(1 + \kappa^2)}}, \tag{4.26}$$

$$M_R = \frac{C_s\lambda b\left[(\gamma - 1)\kappa U - \kappa(\gamma + \kappa^2)c + (\gamma + \kappa^2)\kappa\Omega b\right] + 4\pi\mu a^2\lambda(\omega - \Omega)}{\sqrt{(1 + \kappa^2)}}. \tag{4.27}$$

As previously mentioned, the force balance is carried out assuming that the robot body can move freely along and about the z-axis (2 DOF). Another situation of interest occurs when the body is fully constrained (0 DOF) such that forward velocity (U) and rotation rate (Ω) are zero. Accordingly, the linear propulsive force (F_{R0}) and the required driving torque (M_{R0}) are simply (4.26) and (4.27) with the new constraints applied:

$$F_{R0} = \frac{C_s\lambda(\gamma - 1)\kappa^2 c}{\sqrt{(1+\kappa^2)}}, \tag{4.28}$$

$$M_{R0} = \frac{-C_s\lambda b(\gamma + K^2)\kappa c + 4\pi\mu a^2\lambda\omega}{\sqrt{(1+\kappa^2)}}. \tag{4.29}$$

At this point the force balance is complete. The result is six equations – (4.19), (4.20), (4.26), (4.27), (4.28), and (4.29) – that can be used to solve for the performance characteristics of the system under two different sets of restraints (0 DOF and 2 DOF).

4.1.2 Lighthill Model for Helical Stokeslets

In 1975 Sir James Lighthill delivered a lecture on flagellar hydrodynamics [2]. In the presentation he explained his theorem, based on slender body theory (SBT), for predicting the performance of flagellar propulsion. Lighthill then applied his theory to eukaryotic flagella with helical undulatory motion. The centreline motion of these undulations is identical to the centreline motion of rigid helix undergoing pure rotational motion. Consequently, Lighthill's model as presented in [2], is valid for both prokaryotic and eukaryotic flagella [52]. The actual theory of Lighthill's model is beyond the scope of this work so its development is outlined only briefly here. That said, all information required to implement the model is given.

Lighthill begins his analysis by considering what he coins the zero-thrust swimming speed (U_0) of a flagellum; the performance of the flagellum is considered without any effects from a cell body. However, the rotation of the flagellum with respect to the fluid ($\omega_e = \omega - \Omega$) still takes into account the rotation rate of the body (Ω). It should be noted that Lighthill's analysis neglects flow anomalies that certainly exist at the flagellum tips. Using these assumptions Lighthill arrives concludes that:

$$U_0 = \frac{F_{\theta/L}\alpha b k_s}{4\pi\mu}\left[-1 - ln(\epsilon) + A_1\right], \tag{4.30}$$

$$\Omega = \omega - \frac{F_{\theta/L}}{4\pi\mu b}\left[-\left(1-\alpha^2\right) - \left(2-\alpha^2\right) ln(\epsilon) + \alpha^2 A_1 + 2\left(1-\alpha^2\right)A_2\right], \tag{4.31}$$

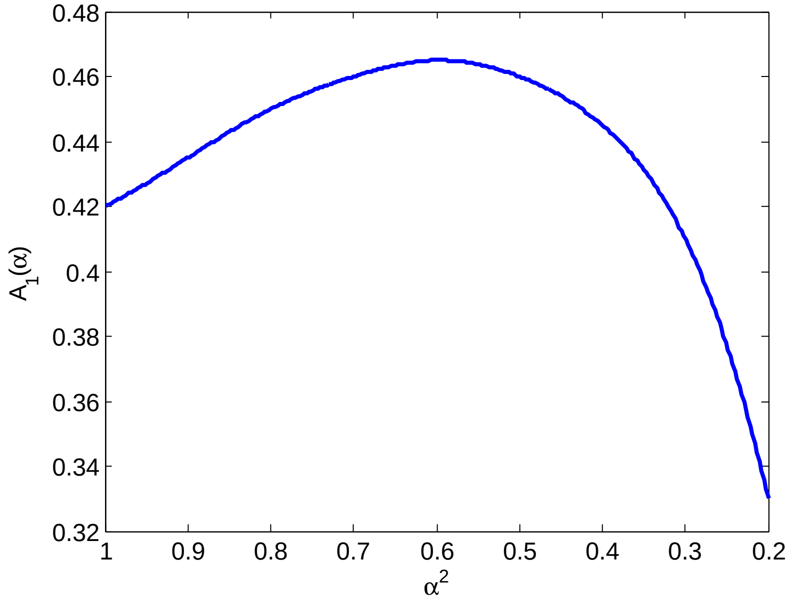

Figure 4.3: The function $A_1(\alpha)$ as replicated from Lighthill [2]

where $F_{\theta/L}$ is the viscous drag force per unit length generated, perpendicular to the axis of rotation, by the flagellum. The value of interest here, as will be shown, is the zero-thrust swimming speed (U_0). To solve for this value the following relationships are required:

$$\Lambda = \sqrt{\lambda^2 + 4\pi^2 b^2}, \tag{3.6}$$

$$k_s = 2\pi/\Lambda, \tag{4.32}$$

$$\alpha = \lambda/\Lambda, \tag{4.33}$$

$$\epsilon = 5.2a/\Lambda, \tag{4.34}$$

where the function A_1 is:

$$A_1(\alpha) = ln(\epsilon) + \int_{\epsilon}^{\infty} \frac{\theta \sin(\theta) d\theta}{\left[\alpha\theta^2 + 2(1-\alpha^2)(1-\cos(\theta)\right]^{3/2}}. \tag{4.35}$$

The solution to Equation (4.35), for $\alpha^2 \in [1, 0.2\}$, is shown in Figure 4.3. The value for $F_{\theta/L}$ is found by considering that the torque $M_R = F_{\theta/L}b$ is balanced by the torque resisting cell body rotation ($D_r\Omega$), where D_r is the rotational damping coefficient of the cell body. Therefore, according to Lighthill[1]:

$$D_r\Omega = bF_{\theta/L}L = 4\pi\mu b^2(\omega - \Omega)\chi\Lambda \tag{4.36}$$

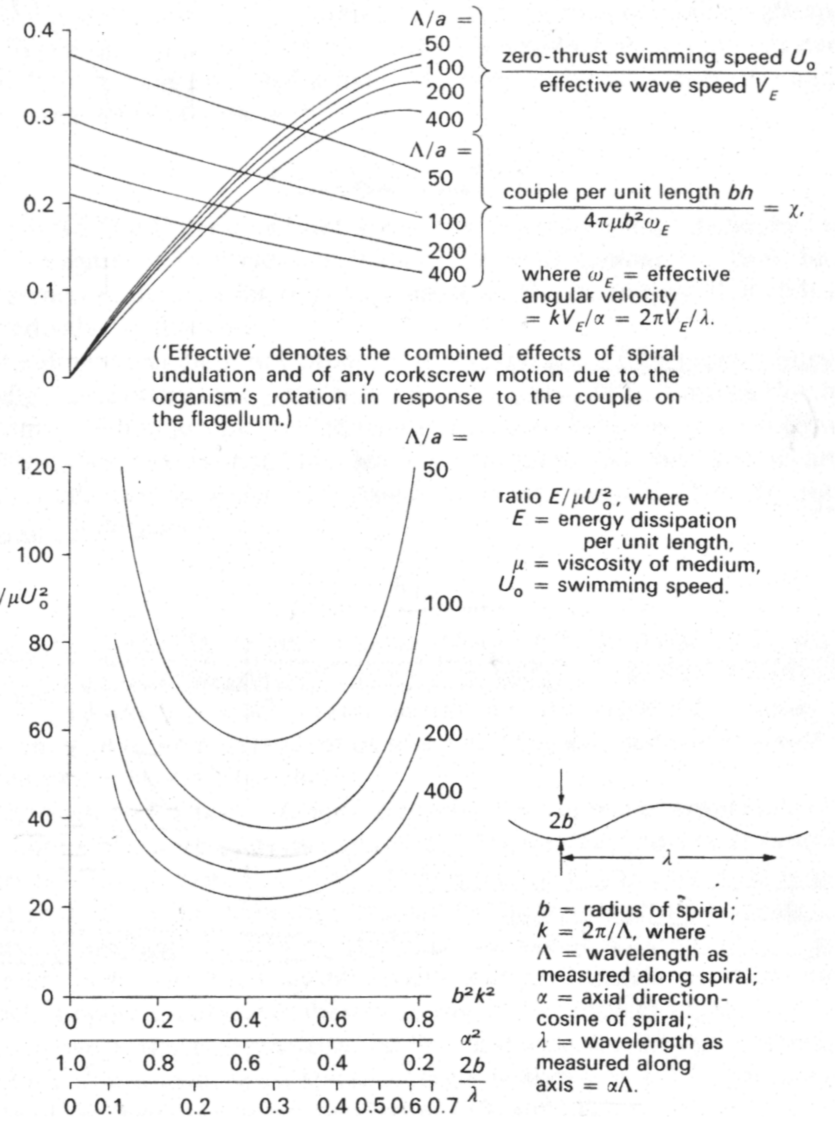

Figure 4.4: Zero-thrust swimming of helical flagella (Lighthill, J., "Flagellar Hydrodynamics", *SIAM Review*, Vol. 18, Figure 12 (pp. 203), pp. 161-230, 1976, Copyright © Society for Industrial and Applied Mathematics. Reprinted with permission)

where χ is taken from Figure 4.4. Given the system layout in Figure 4.1, D_r is the rotational drag coefficient of a sphere with radius R as derived from Equation (4.12) to be:

$$D_r = \frac{M_{body}}{\Omega} = 8\pi\mu R^3. \tag{4.37}$$

Lighthill then expands his model to consider two situations. The first situation is a modified form of the helix motion that gives *nonzero* thrust. The second situation is the same motion further modified to account for the velocity field associated with the drag forces on the cell body. Both situations neglect any end effects at the helix tips. Here, the second situation is presented as it best represents the system proposed. Accordingly, when accounting for the cell body, the swimming speed (U) is:

$$U = \frac{U_0}{1 + \left[\frac{3R}{\alpha L}\left(\ln(\alpha L/2a) - 1\right)\right]}\left[1 + \frac{\ln(\alpha L/R) - \frac{3}{2}}{2\left(\ln(\alpha L/2a) - 2\right)}\right]. \tag{4.38}$$

Given equations (4.37) and (4.36), the rotation rate of the body (Ω) is:

$$\Omega = \frac{\omega}{\frac{2R}{\chi L} + 1}. \tag{4.39}$$

The propulsive force and driving torque required by the rotating flagellum are:

$$F_R = \frac{6\pi\mu R U}{1 + \left[\frac{3R}{\alpha L}\left(\ln(\alpha L/2a) - 1\right)\right]}\left[1 + \frac{\ln(\alpha L/R)}{2\left(\ln(\alpha L/2a) - 2\right)}\right], \tag{4.40}$$

$$M_R = 4\pi\mu b^2(\omega - \Omega)\chi\Lambda. \tag{4.41}$$

If the body is constrained such that all degrees of freedom are removed (0 DOF), the required driving torque (M_{R0}) is Equation (4.41) modified such that $\Omega = 0$:

$$M_{R0} = 4\pi\mu b^2\omega\chi\Lambda. \tag{4.42}$$

Unfortunately, when the body is constrained, the Lighthill model predicts a propulsive force (F_{R0}) value of 0. This is known to be false.

These five equations – (4.38), (4.39), (4.40), (4.41), and (4.42) – are equivalent performance measurements to those developed for the RFT model. The two models may now be compared to one another directly.

---

[1] Valid only for helix of one wavelength, see [2] for multiple wavelength helices

4.1.3 Results and Discussion

Both models are used to evaluate a single wavelength helix as proposed in Section 3.6. The parameters for this helix, as determined in that section, are:

$$\lambda = 5\ [mm]$$

$$b = 0.5\ [mm]$$

$$a = 0.06\ [mm]$$

Setting the filament radius (a) as listed adds uncertainty to the analytical calculations since the filament is designed to be rectangular in cross-section. However, it is speculated that the effect will be minimal since the surface area has remained constant (see Section 3.6.2). If not, a possible solution to lessen any discrepancies is to model the rectangular cross-section in computational fluid-dynamic software to determine an equivalent radius.

The upper limit of the speed of rotation (ω) is calculated by ensuring that the Reynolds number of the filament, with respect to the filament diameter, is less than one. The Reynolds number is defined as:

$$R_f = \frac{\rho V_n d}{\mu} \tag{4.43}$$

where V_n is the magnitude of the velocity normal to the helix. With the helix as given in Equation (3.5), the velocity at any point, assuming a fixed head, is:

$$\mathbf{V} = (\dot{x},\ \dot{y},\ \dot{z}) = (-b\omega\sin(\theta),\ b\omega\cos(\theta),\ 0) \tag{4.44}$$

where $\omega = \dot{\theta}$. The unit vector tangential to the helix centreline is:

$$\hat{e}_s = (-bk_s\sin(k_s s),\ -bk_s\cos(k_s s),\ \alpha) \tag{4.45}$$

given that $\theta = k_s s$ as outlined in [2]. Accordingly, the magnitude of the fluid velocity normal to the helix is:

$$V_n = \sqrt{|\mathbf{V}| - \mathbf{V}\cdot\mathbf{e}_s} = \omega b\alpha. \tag{4.46}$$

Therefore, Equation (4.43) can be used to solve for (ω). To do so, d is set as the diameter of the filament ($2a$), the velocity is set as in Equation (4.46), and the Reynolds number is set to be less than one to ensure low Reynolds flow:

$$\omega < \frac{\mu}{2\rho b\alpha a}. \tag{4.47}$$

This equates to a maximum rotation rate relative to a fixed cell body of $\omega = 7\pi\ [rad/s]$. Accordingly, the analytical models are evaluated from $\omega = 0$ to the aforementioned maximum.

With all values in place the two analytical models are evaluated. Two situations are considered. First, the robot body is constrained in all six directions (0 DOF) and the propulsive force (F_R0) and required driving torque (M_R0) are computed. Unfortunately, Lighthill's model cannot be used to derive the propulsive force when the body is stationary and therefore only the results from the RFT model are presented. Second, the robot is allowed to move along and about the z-axis (2 DOF). Under these conditions, the forward velocity of the body (U), rotational rate of the body (Ω), propulsive force (F_R), and the driving torque (M_R) are computed.

The results are given in Figures 4.5 – 4.10 and several observations can be made. The curves pertaining to translation along the z-axis do not match well. Setting the Lighthill model as the baseline, RFT predicts a 77.0% greater swimming speed fueled by a 42.0% greater propulsive force. The curves pertaining to rotation about the z-axis match considerably better. RFT predicts a 3.8% greater body rotation rate and driving torque. In a fully constrained state, a 13.0% greater driving torque at the body is predicted.

At this point, the accuracy of the analytical models is unclear. Since they do not match well they cannot validate each other. Furthermore, without a physical system to compare with, neither model can be labelled as accurate. Such a comparison is carried out in Chapter 5.

Another value of interest is the efficiency of the propulsion system as predicted by the analytical model. Efficiency is defined as:

$$\eta = \frac{\text{Power Out}}{\text{Power In}} = \frac{F_R U}{M_R \Omega}. \tag{4.48}$$

Given Equation (4.48), the efficiency of the system is 0.21% according to the Lighthill model and 0.51% according to RFT. This is very low but is comparable with natural systems, which have an efficiency value of approximately 1%. Purcell notes in his historic paper *Life At Low Reynolds Number* that the low efficiency of micro-organisms is a result of their environment and the abundance of nutrients available to them; there is no motivation for high efficiency when food is plentiful [41]. However, for the purposes of this work, the low efficiency of the system is an issue if batteries are required to power the microrobot. It may be possible to increase the predicted efficiency by modifying the helix parameters. Once an accurate model for the propulsion system is found, exploring possible options should be relatively simple.

Lastly, the difference between eukaryotic propulsion and prokaryotic propulsion is explored. Recall that the difference is a result of dissimilar rotation rates of the flagellum about its centreline tangent. As mentioned, Brennen and Winet suspected that the difference would be minor [25]. To investigate the claim the two motions can be compared analytically. Equations (4.19) and (4.20) describe a prokaryotic system. A eukaryotic system is described by setting A in equations

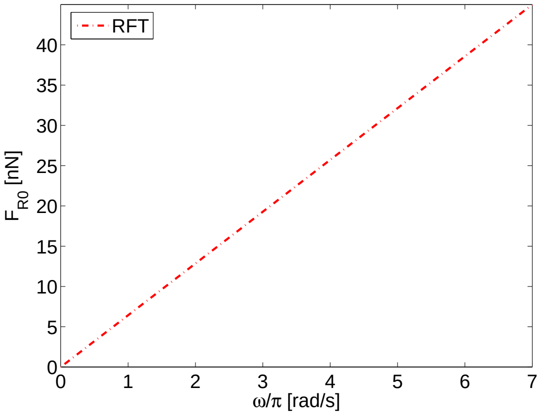

Figure 4.5: Reaction Force (0 DOF)

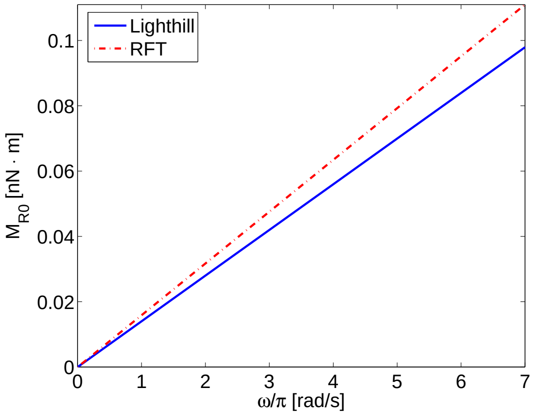

Figure 4.6: Reaction Torque (0 DOF)

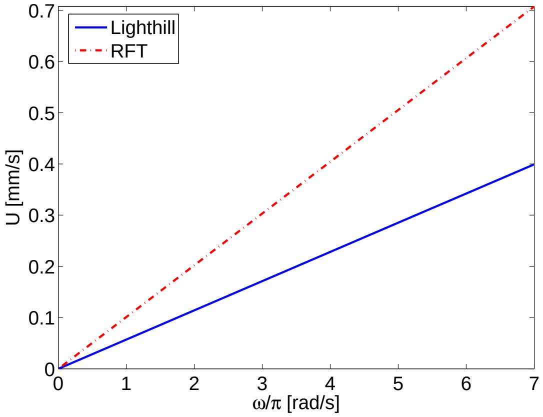

Figure 4.7: Forward Velocity (2 DOF)

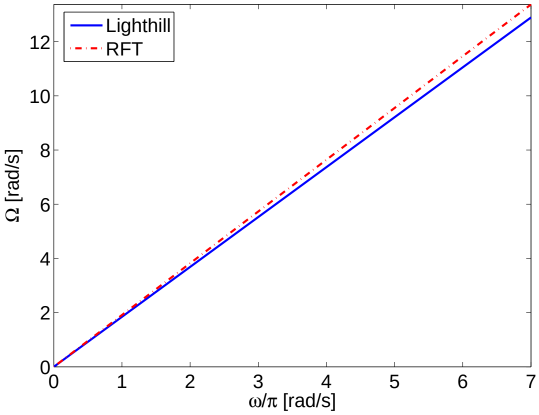

Figure 4.8: Body Rotation Rate (2 DOF)

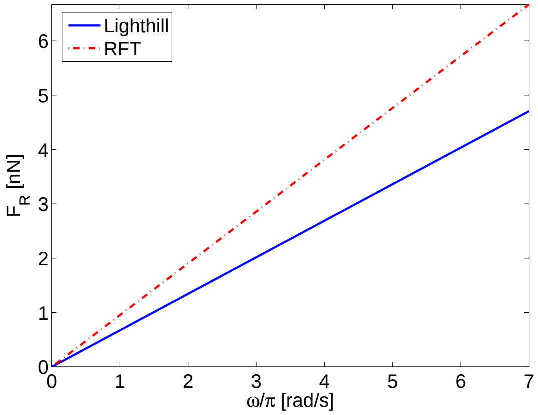

Figure 4.9: Propulsive Force (2 DOF)

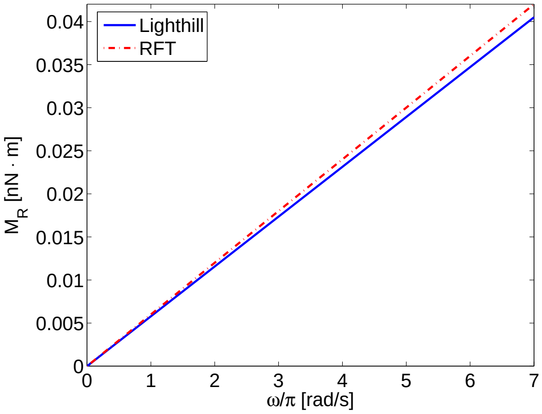

Figure 4.10: Driving Torque (2 DOF)

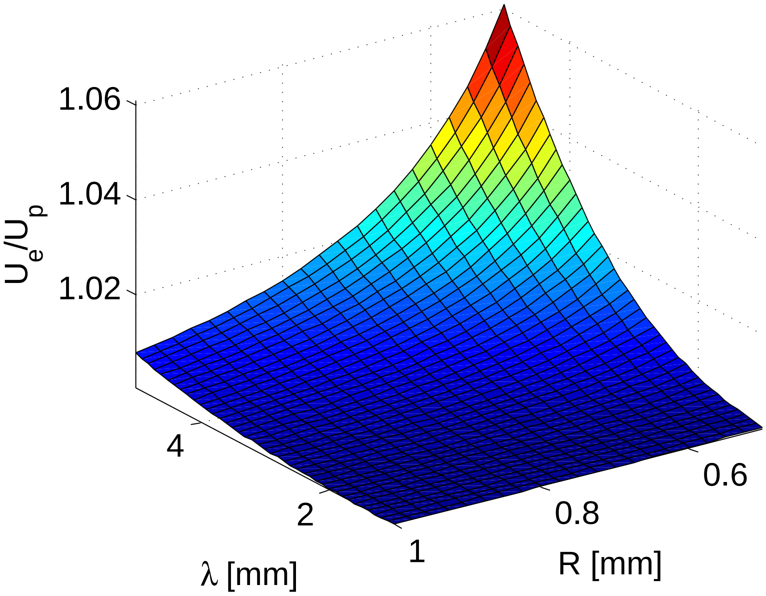

Figure 4.11: Analytical difference between eukaryotic and prokaryotic propulsion

(4.19) and (4.20) to zero. The two systems are compared to arrive at the following:

$$\frac{U_e}{U_p} = 1 + \frac{a^2\lambda}{2R^3\sqrt{1+4\pi^2\left(\frac{b}{\lambda}\right)^2}} \tag{4.49}$$

where U_e is the velocity of a eukaryotic system and U_p is the velocity of a prokaryotic system. Equation (4.49) shows that as the filament radius (a) or helix wavelength (λ) decreases, the two systems behave more similarly. Likewise, as the body radius (R) increases the two systems behave more similarly.

To evaluate the difference between the two systems in actual systems, Equation (4.49) is evaluated for two situations: 1) a series of biological organisms as surveyed by Brennen and Winet, and 2) a range of helix configurations with similar scale as the system proposed. The results from the first situation are that the ratio U_e/U_p is essentially one for biological organisms. Accordingly, as Brennen and Winet suspected, for micro-organisms, differences between centre-line rotation rates creates negligible difference in forward velocity. The results from the second situation are given in Figure 4.11. Here, it is observed that the difference between prokaryotic propulsion and eukaryotic propulsion for similarly dimensioned helices is not negligible. For instance, the values used in this work create a non-trivial ratio of $U_e/U_p = 1.06$. Accordingly, the difference is significant enough that if RFT is used, it is recommended to not treat eukaryotic and prokaryotic motion as interchangeable.

4.2 Multi-body Dynamics Model

Accurate analytical modelling can provide a prediction of the performance of a rigid helical flagella. However, the proposed flexible filament propulsion system displays transient behaviour as it contorts into a stable helix. A model is required to see if this transformation will take place and prove the feasibility of the design. Accordingly, a model, described in this section, was created in the multi-body dynamics software package MSC.ADAMS to provide insight into this transient behaviour.

4.2.1 Model Setup

The flexible filament is extremely complex from a modelling point of view. The system incorporates multi-body dynamics, fluid mechanics, and large deformation structural mechanics. Furthermore, all three systems are coupled — a driving torque is applied to the base of the flagellum and it begins to rotate. The velocity causes pressure which, in turn, causes deformation which, in turn, affects the required torque.

The complexity of the system requires simplifications to be made when modelling in ADAMS. ADAMS does not have provisions for drag caused by fluid flow over immersed bodies. To account for this limitation, the flexible filament is first broken into a series of N rigid links – where the i^{th} link, for $i = 1 \rightarrow N$, is length L_i – attached via revolute joints. The links are lined up end to end according to the start position of the filament (Fig. 3.2) [53]. To preserve the twist of the filament, each joint axis is oriented according to the helical torsion (τ) and its distance from the rigid link (s). This orientation (ξ) is best described relative to the orientation of the previous joint. Therefore, mathematically for the i^{th} joint:

$$\xi_i = \tau\left(s_{i-1} - s_i\right) = \tau L_i \quad \text{for } i = 1 \rightarrow N. \tag{4.50}$$

Figure 4.12 shows the ADAMS model with the discrete links attached via revolute joints. The inset enlarges one of the links to emphasize the orientation change of the joints according to the required filament twist.

Second, the filament stiffness is approximated by applying a torque at each joint. Figure 4.13 shows a single link with the torque – represented by the large curved arrow – applied to it.

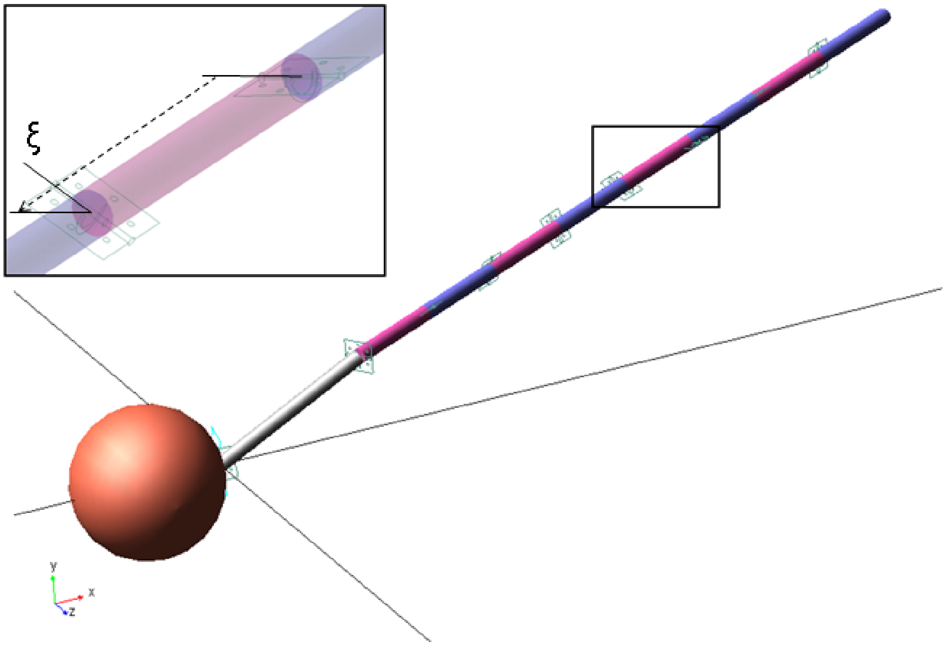

Figure 4.12: ADAMS model with discrete links attached via revolute joints

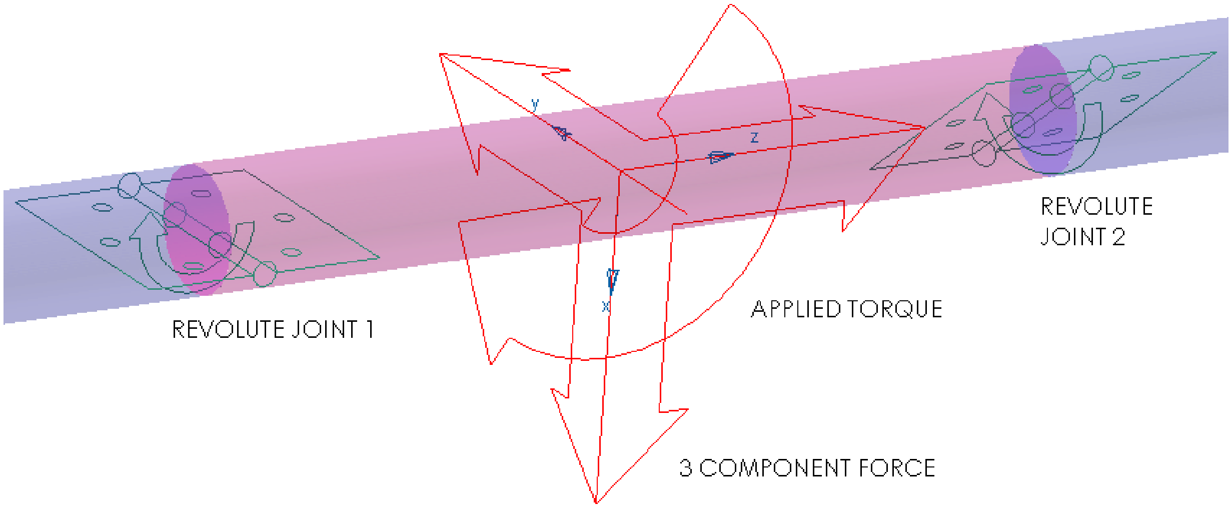

Figure 4.13: Single link of ADAMS model with rotational torque and 3-component linear force applied to it.

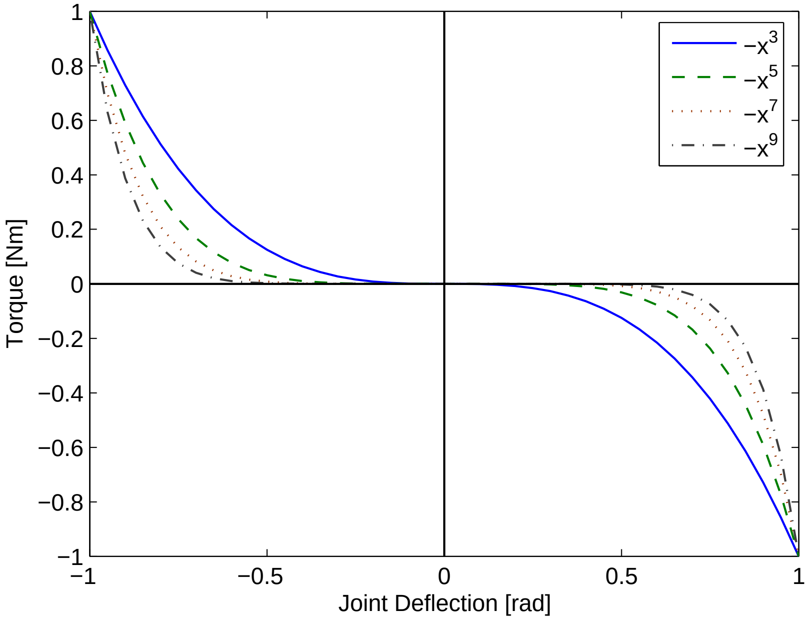

Figure 4.14: Odd power stiffness profiles

The torque is set to mimic a variable stiffness torsional spring at the joint. The torsional spring element found in ADAMS was not used because it does not allow for stiffness to be defined as a function: only as a spline.

As outlined in Section 3.6.1, it is desired to have the filament exhibit a two-stage elastic response. This is accomplished by applying a torque (**T**) at each joint that has a negative odd power function as its stiffness profile. The general form, shown in Fig. 4.14, is:

$$|\mathbf{T}_i| = -\left(\frac{\phi_i}{m}\right)^{2j+1} \qquad \text{for } i = 1 \rightarrow N,\ \ j \in [1, n], \tag{4.51}$$

where ϕ^i is the deflection from equilibrium of the i^{th} joint, and m and j are scaling factors that modify the curve profile as required (see Section 4.2.3) to create a fully developed helix. The negative sign ensures that the applied torque negates deflection from equilibrium.

Third, drag is accounted for by implementing lumped parameter drag forces on the body and helix links. The linear drag force ($\mathbf{F}_D$) and angular drag torque ($\mathbf{T}_\Omega$) for the body are [43]:

$$\begin{aligned} \mathbf{F}_{body} &= -6\pi\mu R\mathbf{U}, \\ \mathbf{M}_{body} &= -8\pi\mu R^3\Omega, \end{aligned} \tag{4.52}$$

where $\mathbf{U}$ is the velocity vector of the body in a global frame and $\mathbf{\Omega}$ is the angular velocity vector. The dynamic viscosity of the medium μ is approximated as water ($1.0\ cP$) based on the results of Table 3.1.

On the body, the drag forces and torques are implemented using one general, six-component force. The magnitude of each force/torque is described using a function incorporating the velocity of the body with respect to the global frame (read: fluid).

Drag forces on the links are defined based on analysis of slender bodies in viscous fluid flow as performed by Cox [54]. They are applied relative to a body-fixed coordinate system on each link as seen in Figure 4.13. The forces are:

$$F_x = -K_n L_i\,(\mathbf{V_i} \cdot \hat{e}_x), \tag{4.53}$$

$$F_y = -K_n L_i\,(\mathbf{V_i} \cdot \hat{e}_y), \tag{4.54}$$

$$F_z = -K_s L_i\,(\mathbf{V_i} \cdot \hat{e}_z), \tag{4.55}$$

where $\mathbf{V_i}$ is the velocity vector of the centre of gravity of the i^{th} link in the global frame. L_i is the length of the i^{th} link and K_s and K_n are defined by Cox [54] as:

$$\begin{aligned} K_s &= \frac{2\pi\mu}{\ln(L_i/a) - \frac{3}{2} + \ln(2)}, \\ K_n &= \frac{4\pi\mu}{\ln(L_i/a) - \frac{1}{2} + \ln(2)}. \end{aligned} \tag{4.56}$$

Link drag forces are implemented in ADAMS as general, three-component forces. Figure 4.13 shows the physical representation of the force in ADAMS. Like the body, the forces on the principal axes of each link are functions incorporating the velocity of that link with respect to the global frame.

4.2.2 Dimension Scaling in ADAMS

In ADAMS, any number less than 1×10^{-11} is truncated to 0. This is a serious limitation of the software when dealing with devices based in millimeter or smaller scales. To eliminate the problem the system variables need to be scaled to an acceptable level. However, scaling of parameters must be done intelligently so that the scaled system behaves identically to the original system. The procedure to perform proper scaling is as follows.

First, the basic dimensions of the system are defined. All other variables can be defined in terms of the three basic dimensions. There are two basic dimension options: mass (M), length (L), time (T) or force (F), length (L), time (T). For this work the MLT system of basic dimensions. The two systems are related by:

$$F \equiv MLT^{-2} \tag{4.57}$$

Second, each system variable is written as a dimensionless ratio containing only itself and the basic dimensions. If these ratios are kept constant during the scaling process, the systems will behave identically. An example of the dimensionless ratio for torque is given below[2].

$$\text{Torque (T)} \Rightarrow \Pi_T = \left.\frac{\mathrm{T}\ \cancel{\left[kg\, m^2\right]}}{\cancel{[s^2]}}\right| \frac{T^2\ \cancel{[s]^2}}{M\ \cancel{[kg]}\ L^2\ \cancel{[m]^2}}$$

Third, the scaling factor for each basic dimension is set. The values chosen must ensure that all system parameters have nominal values within the range required by the software (e.g. for ADAMS $\geq 1 \times 10^{-11}$).

Fourth, the scaling factors for the system parameters are determined. They are based on the predefined basic dimension scaling factors and the requirement that all dimensionless ratios remain constant.

For instance, consider that L is scaled by 1000, while M and T are kept unchanged. To keep Π_T constant, torque inputs to the system must be scaled by a factor of 100,000. Conversely, torque measurements from the system must be scaled by a factor of 1/100,000. The validity of this scaling approach is shown in the following example.

System Scaling Example

Consider a simple cylindrical pendulum, made of steel ($\rho = 7801\ [kg/m^3]$), as shown in Fig. 4.15. The dimensions are $l = 10\ [mm]$ and $r = 0.5\ [mm]$.

The system parameters can be described, using MLT basic dimensions, by the following dimensionless ratios. Keeping these ratios constant will result in final systems that behave iden-

---

[2] MLT basic dimensions.

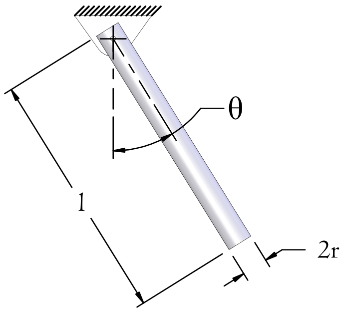

Figure 4.15: Simple pendulum

tically to the original.

Length (l)	$\Pi_l = \frac{l}{L}$
Radius (r)	$\Pi_r = \frac{r}{L}$
Gravity (g)	$\Pi_g = \frac{gT^2}{L}$
Density (ρ)	$\Pi_\rho = \frac{\rho L^3}{M}$

A second system is now defined where mass (M) and time (T) are left constant but length (L) is scaled up by a factor of 1000. Given this scaling factor, the four system parameters must be scaled accordingly. The table below shows the original parameters as well as the appropriately scaled parameters for the second pendulum.

Parameter	System 1	System 2
l	10 $[mm]$	10 $[m]$
r	0.5 $[mm]$	0.5 $[m]$
ρ	7801 $[kg/m^3]$	7801×10^{-9} $[kg/m^3]$
g	9.81 $[m/s^2]$	9810 $[m/s^2]$

Both systems are then simulated in ADAMS. Figure 4.16 shows that the behaviour of the two pendulums is identical despite the change in scale.

More sophisticated analysis can be performed using Buckingham Pi theory and dimensional analysis [43]. This approach allows a system to not only be scaled, but to be defined by a minimal number of non-dimensional parameters. This approach is common in fluid mechanics and is the basis for the formation of famous variables such as the Mach and Reynolds numbers.

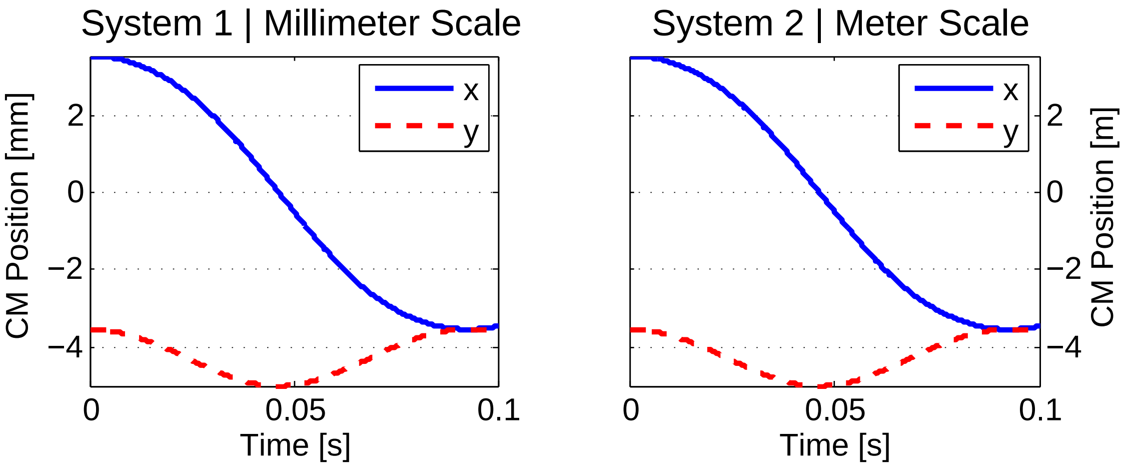

Figure 4.16: Comparison of two models at different scale

Scaling in ADAMS Model Created

For this work, the ADAMS model length parameters are scaled by a factor of 1000. That said, unless otherwise noted, all values listed in Sections 4.2.1 and 4.2.3 are unscaled. See Appendix A for a table listing the corresponding scaling factors used in the ADAMS model.

4.2.3 Results and Discussion

The ADAMS model is built using the same helix parameters outlined in Section 4.1.3. Figure 4.17 shows the ADAMS model at a steady-state condition such that a helix is fully formed. The body is a simple sphere 1 [*mm*] in diameter. Attached to the body is the rigid link. This part is essentially arbitrary. Its purpose is to scribe the appropriate helix amplitude and that is the only constraint placed on it. For the ADAMS model created, the rigid link is 1.118 [*mm*] long and rotated by 30° about the global y-axis.

The discretization of the helix requires additional geometric parameters to be defined, namely, the length of the individual links (L_i), the orientation of the the joints (ξ_i), and the desired deflection of each joint at steady-state (ϕ_i). To ease modelling, the parameters are identical for each link/joint (e.g. $L_1 = L_2 = L_3 ...$).

The length of each link is found by dividing the length of the filament (Λ) by the number of links (N):

$$L_i = \frac{\Lambda}{N}. \tag{4.58}$$

For this work, $N = 8$ and $L_i = 0.738$ [*mm*]. Link 1 of the helix sets the start position of the entire

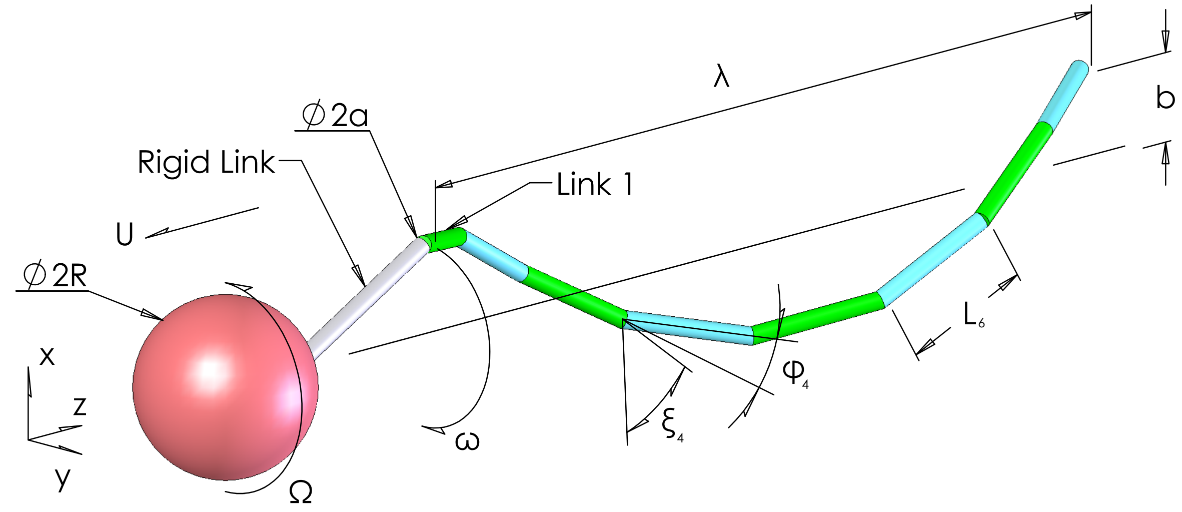

Figure 4.17: ADAMS model at steady state

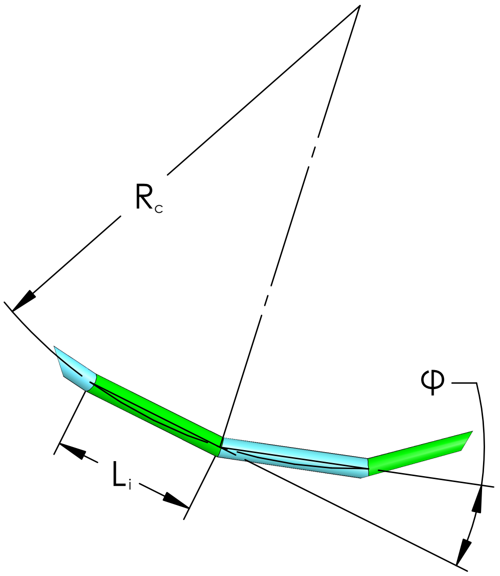

Figure 4.18: Desired joint deflection (ϕ) defined by radius of curvature (R_c)

helix. It is parallel to the y-z plane and is oriented along a vector rotated $\beta = 32.14°$ about the global x-axis (see Section 3.6.2).

Given L, the orientation of each link, with respect to the previous link, is defined by Equation (4.50) to be $\xi = 38.16°$ The desired steady-state deflection is:

$$\phi = \pi - 2\cos^{1}\left(\frac{L_i}{2R_c}\right). \tag{4.59}$$

Equation (4.59) is based on the geometry of the system as outlined in Figure 4.18 with R_c as defined in Equation (3.10). Given the system parameters, Equation (4.59) evaluates such that $\phi_{2-8} = 24.1°$. This is true for all links except the first. In a steady-state position, the first-link optimal deflection is $\phi_1 = \phi_{2-8}/2 = 12.05°$.

The last variable to be set is the stiffness profile for each joint. Recall that the stiffness profile, as shown in Figure 4.14 and described in Equation (4.51), emulates a two-stage elastic response so that the ability of the filament to form a complete helix is robust. For each joint, the scaling factors (m and j) need to be determined such that a complete helix forms when the ADAMS model is run. To set these factors, a trial-and-error method was used; the results are listed in Table 4.1. Since the final ADAMS model was used to tune these parameters they are given after scaling has been applied.

These joint stiffness profiles are interesting in how the value of m changes for each joint. Consider that the lower the value of m, the stiffer the joint. Therefore, Table 4.1 implies that the filament needs to increase in thickness along its length. This is opposite to the speculation, in Section 3.6.2, that the filament would need a slimming taper to maintain a constant curvature. This apparent contradiction is explored further in Section 5.4.

With the model's geometric parameters set, the ADAMS model can be run and the results evaluated. Three situations are considered:

1. Tail revolute joints fixed (Rigid Tail) at desired steady-state position ($\phi_1 = 12.05°, \phi_{2-N} = 24.1°$, Fig. 4.17).
2. Flexible tail created by unconstraining link revolute joints (Flex tail), tail initially at start position (Fig. 3.2).
3. Body unconstrained (6 DOF), flexible tail via unconstrained revolute joints (Flex tail), tail initially at start position.

The first situation (Rigid Tail) provides a direct comparison to the analytical models explored in Section 4.1.3. Its purpose is to explore the validity of the lumped parameter approach used to create the ADAMS model. All six variables ($U, \Omega, F_R, M_R, F_{R0}$, and M_{R0}) are measured and

Joint	m	j
1	0.7	11
2	1.7	11
3	1.5	11
4	1.3	11
5	1.3	11
6	1.2	11
7	1.2	11
8	1.5	11

Table 4.1: ADAMS joint stiffness profile scaling factors by joint

analyzed. First, the body is fixed (0 DOF) to explore propulsive force (Fig. 4.19) and required driving torque (Fig. 4.20). Then, the body is allowed to move along and about the z-axis (2 DOF) to explore the forward velocity (Fig. 4.21), the body rotation rate (Fig. 4.22), the propulsive force (Fig. 4.23), and the required driving torque (Fig. 4.24) generated by the helix.

When the body is fixed, the results from ADAMS differ from the analytical results by large margins. In this situation the driving torque (M_{R0}) is 13.3% greater than the data provided by the Lighthill model. Propulsive force (F_{R0}) is 42.2% less than the values predicted by RFT. Both values are consistent for the entire speed range tested.

With regards to the 2 DOF situation, the results from the ADAMS model once again do not match well with the analytical models. Using the Lighthill model as a baseline, the forward velocity (U) is underestimated by 29.1% and the propulsive force (F_R) is underestimated by 43.3%. Body rotation rate (Ω) is 9.7% greater while the required driving torque (M_R) is only 3.75% greater. The efficiency of the system is only 0.077%.

The ultimate goal of the ADAMS model is to predict the transient and steady-state behaviour of a flexible filament propulsion system. The differences between the Lighthill, RFT, and ADAMS models cast doubt upon the ability of the lumped parameter ADAMS model to do so. However, it should be noted that the three models do fall within the same order of magnitude, which does infer a level of qualitative accuracy to the ADAMS model. In other words, at this point, while the model may not be used as a precise predictor of filament position, it can be used to predict the general behaviour of the filament. It is hoped that experimental testing will determine how accurate the ADAMS model is (see Chapter 5).

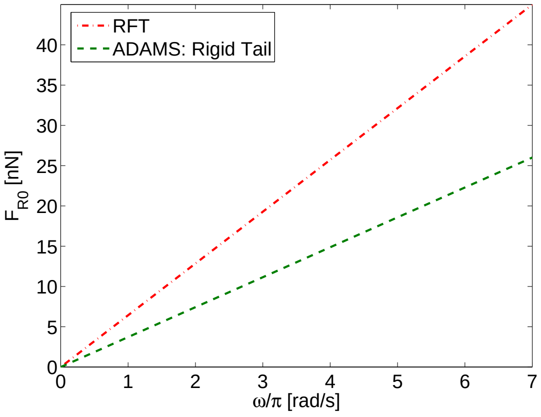

Figure 4.19: Propulsive Force (0 DOF)

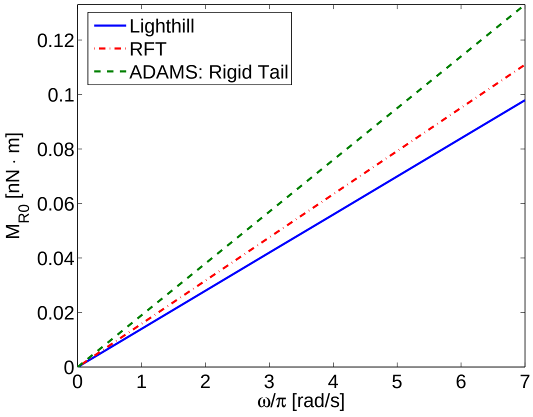

Figure 4.20: Driving Torque (0 DOF)

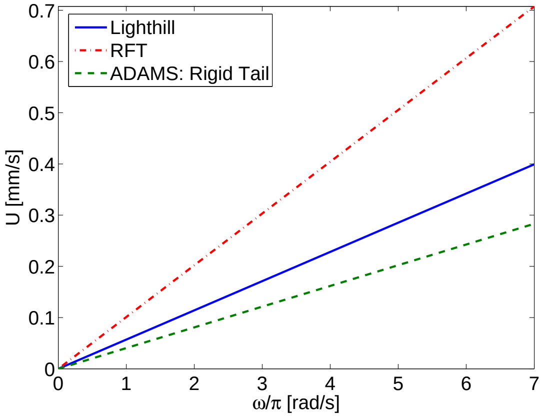

Figure 4.21: Forward Velocity (2 DOF)

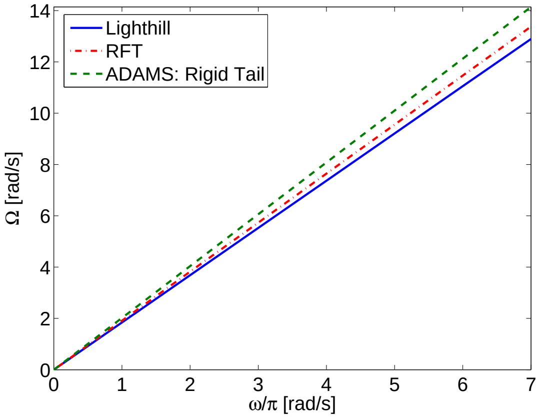

Figure 4.22: Body Rotation Rate (2 DOF)

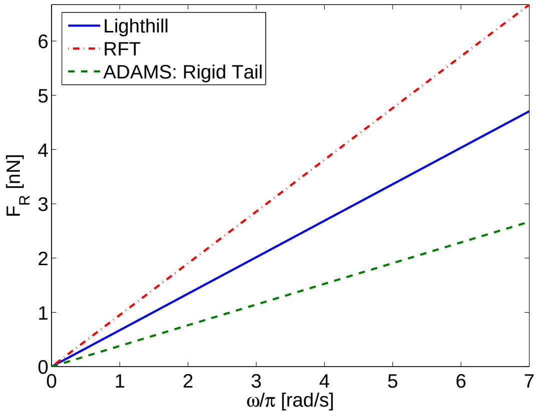

Figure 4.23: Propulsive Force (2 DOF)

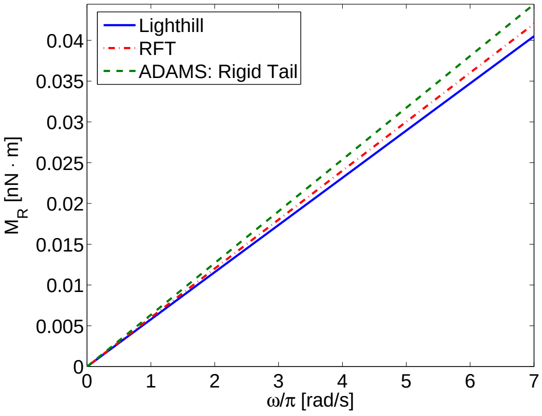

Figure 4.24: Driving Torque (2 DOF)

If the ADAMS model is deemed inaccurate, one possible contributing factor is the slenderness ratio (L_i/a) of the links used in the ADAMS model. The drag coefficients (K_s and K_n) used are derived by Cox [54] under the assumption that their accuracy increases as $a/L_i \rightarrow \infty$. However, using the ADAMS model parameters, the slenderness ratio is only 12.3. It is hoped that this low ratio will not cause significant inaccuracy in the model, however; as mentioned, if inaccuracy exists this could be a contributing source.

Given the qualitative accuracy attributed to the ADAMS model, the second situation is considered. This configuration (Flex Tail) emulates a flexible filament by unconstraining the revolute joints in the tail. The intent for this configuration is to explore the steady-state performance of a flexible filament propulsion system with respect to a rigid tail. To allow for comparisons to the analytical models, this configuration constrains the body in a similar fashion. First, the body is fixed (0 DOF) and the tail begins in the start position as outlined in Figure 3.2. Then, the body is allowed to move (2 DOF) but the tail still begins in the start position. In this situation, the operating conditions of the robot are not indicative of the final environment of a free-floating robot. Therefore, transient behaviour is not looked at in depth here.

Figures 4.25 – 4.27 show the progression of the tail from the start position to steady-state behaviour when rotated at $\omega = 2\pi$ $[rad/s]$ and the body is fixed (0 DOF). From the figures it can be seen that, as hoped, the flexible filament does contort into a helix under rotational load. The model is essentially at steady-state behaviour by 5 revolutions. Similar behaviour is present when the robot body is allowed to move (2 DOF) although steady-state behaviour takes longer to develop (8-10 revolutions). Revolutions are quoted because these values are consistent for the entire speed range tested. For example, at $\omega = 4\pi$ $[rad/s]$, steady-state behaviour still occurs within approximately 5 revolutions.

To quantitatively examine the ability of the filament to form a complete helix, the steady-state angle of rotation of each joint (ϕ) can be measured and compared to the desired angle. Figure 4.28 gathers these results when the body is fully constrained (0 DOF) and $\omega = 2\pi$ $[rad/s]$; numerical values are available in Appendix A. The results show that all joints, except the second, over-rotate. The largest over-rotation is 20% and the average difference is approximately 10%. Even though this difference is moderately significant, the model is deemed acceptable. This is done because the stiffness profile scaling factors (m and j) are not independent from one another. As such, tuning them is a tedious process that is not guaranteed to produce better results. Another reason for allowing this difference is that a similar analysis, conducted when the body is allowed to move (2 DOF), produces better results. The maximum difference is only 7% and the average difference is only 4% (see Appendix A for numerical values).

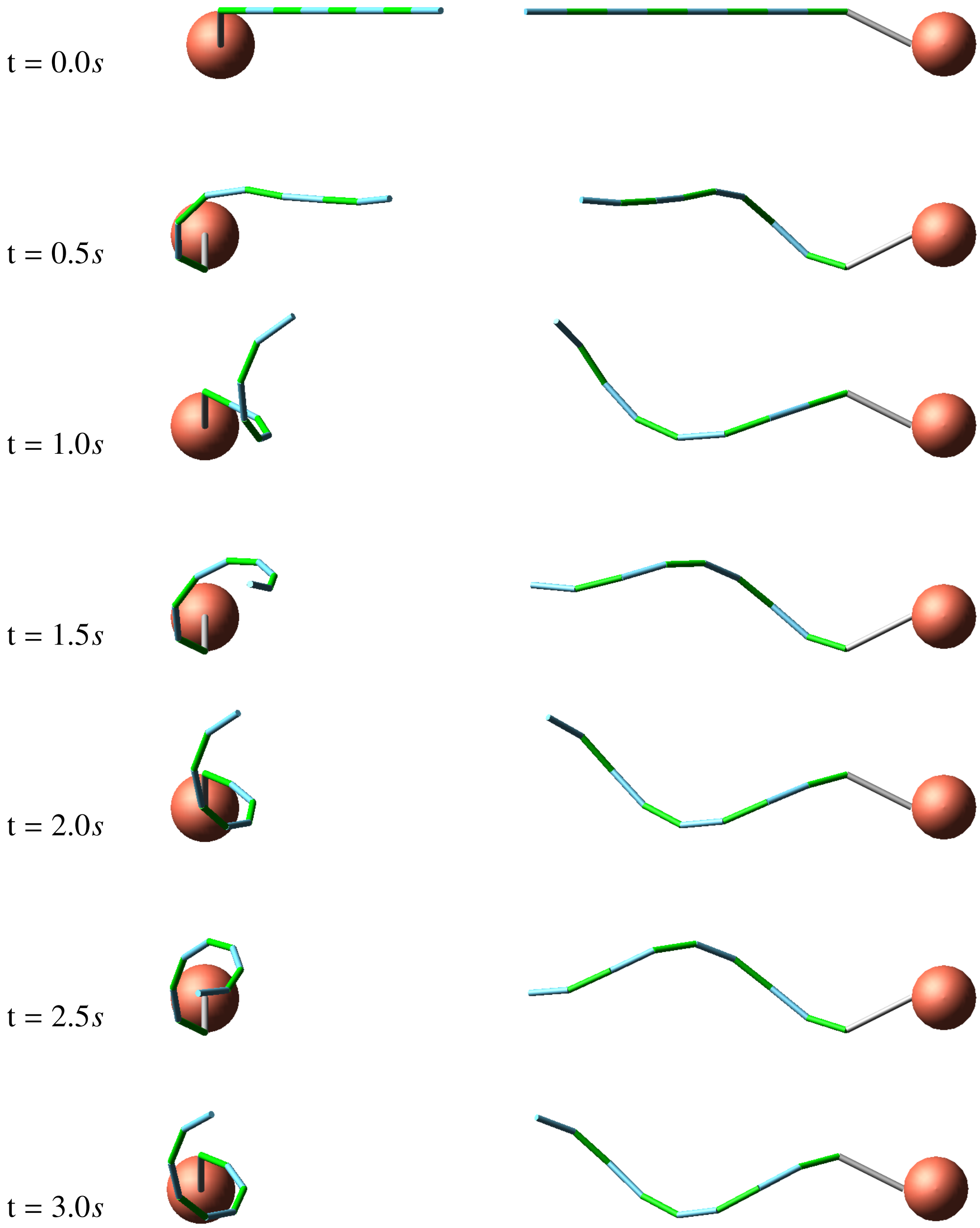

Figure 4.25: Tail position with body fully constrained (a)

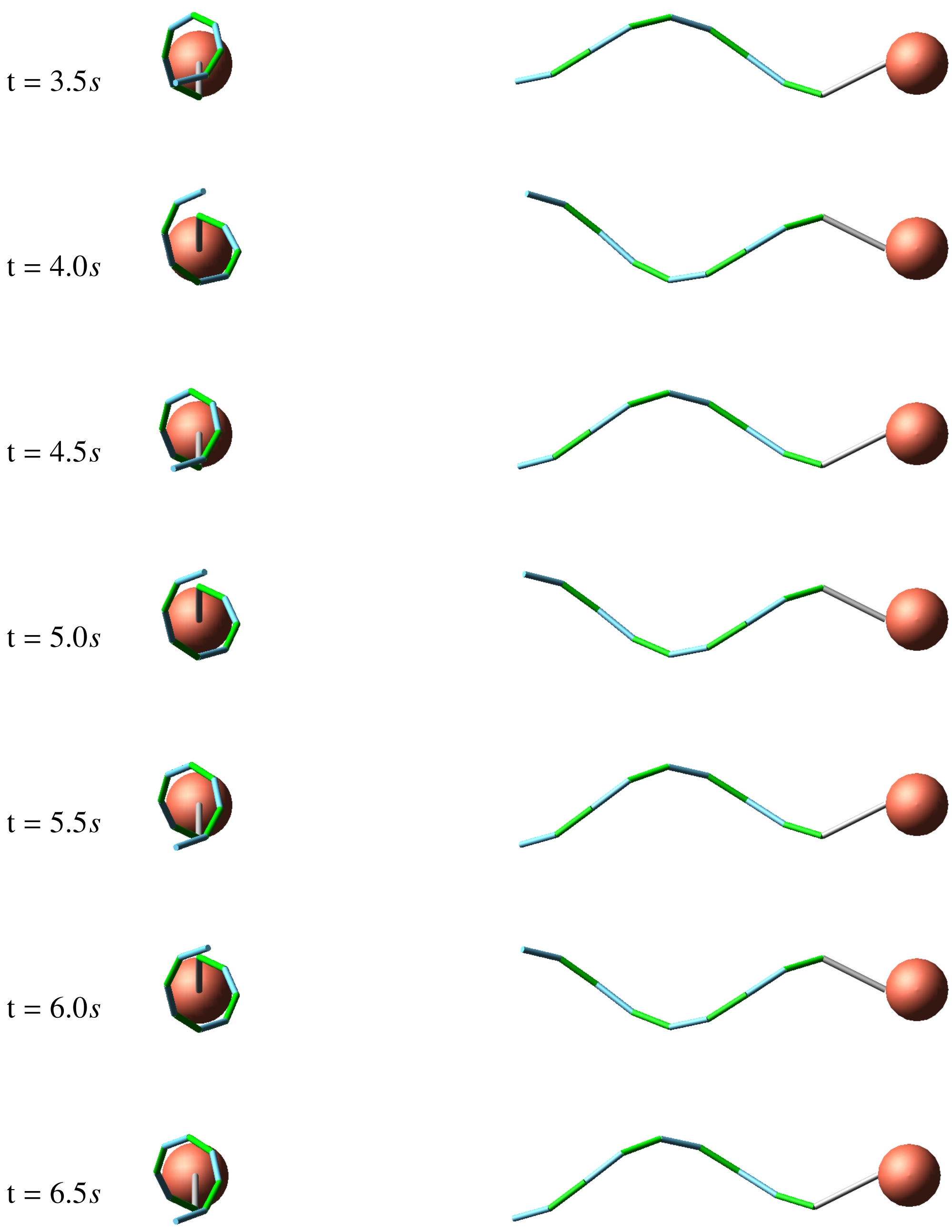

Figure 4.26: Tail position with body fully constrained (b)

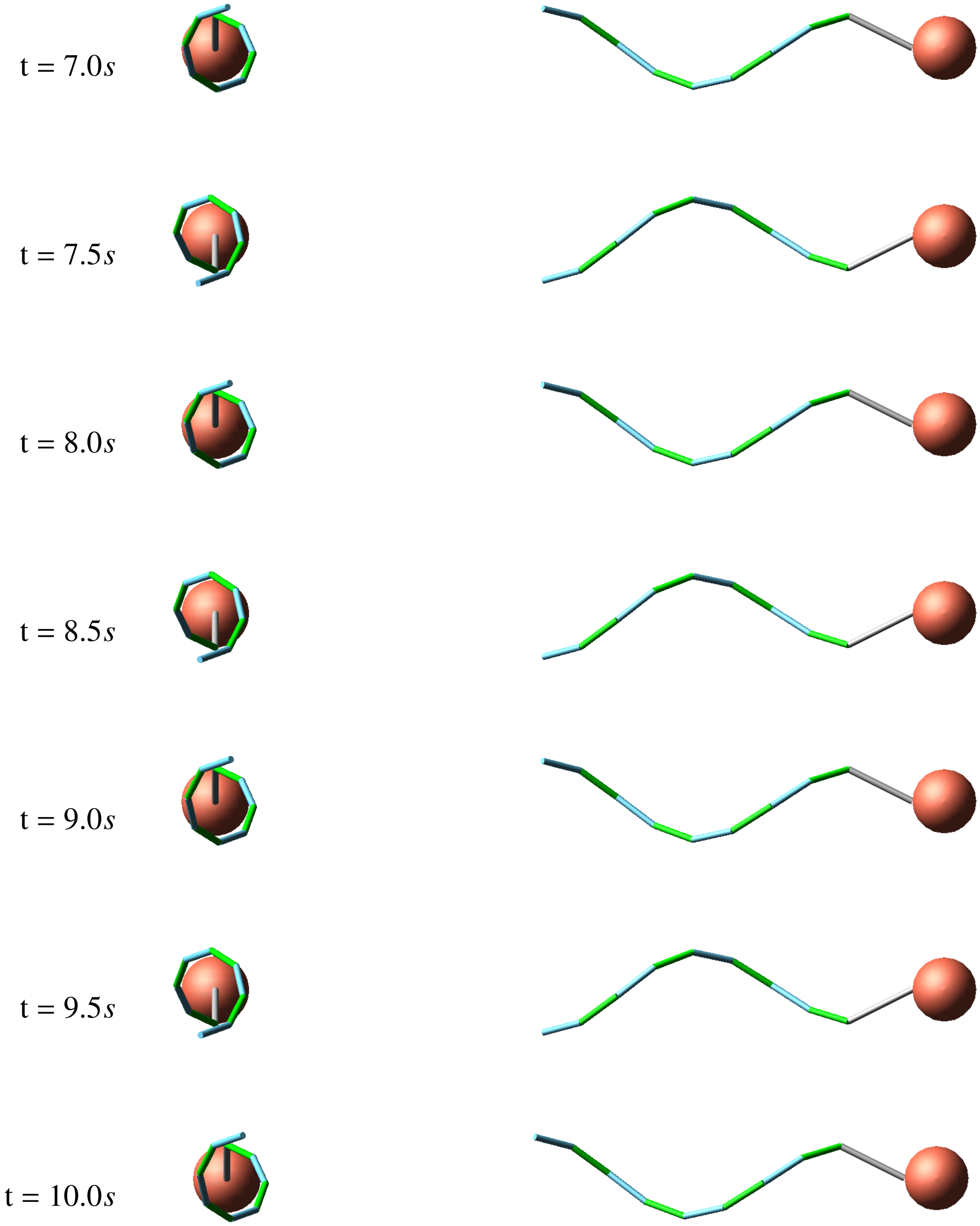

Figure 4.27: Tail position with body fully constrained (c)

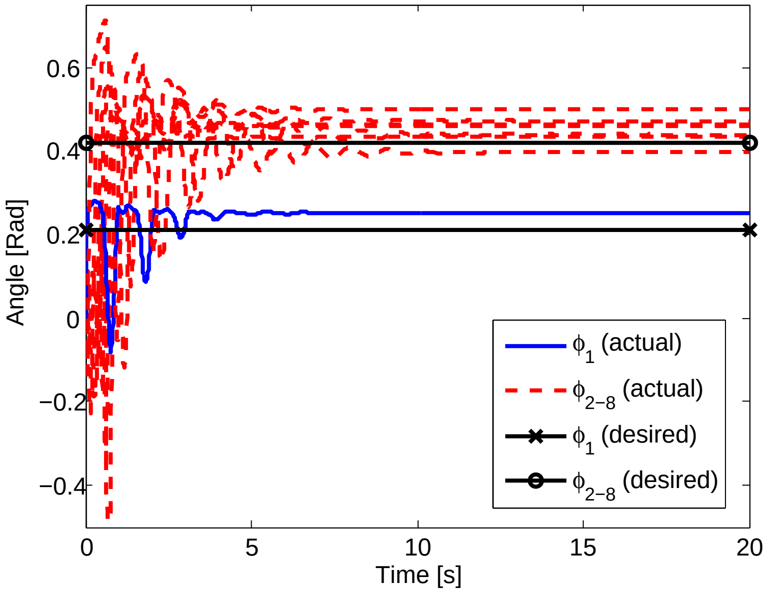

Figure 4.28: Joint deflection angles versus time: actual and desired

Another notable result seen in Figure 4.28 is that most joints settle into their steady-state values by approximately 5 seconds (or 5 revolutions at $\omega = 2\pi$ $[rad/s]$). This is consistent with the observations made from Figures 4.25 – 4.27. However, two joints continue cycling about their steady-state value until approximately 10 revolutions have passed. While this does not seriously affect performance, to help ensure accuracy all measurements should be taken only after full steady-state behaviour is achieved.

The steady-state performance of the flexible tail is explored quantitatively by comparing it to the fully constrained tail. Figures 4.29 – 4.34 show this comparison. It should be noted that for all simulation data pertaining to the flexible tail, the data is fit with a least squares linear curve. In the models previous to the flexible tail (analytical, and rigid tail configuration in ADAMS) the tail had a linear response so no curve fitting was necessary. However, for the flexible tail, the material stiffness comes into play and, even with the two-stage stiffness profile, as the loads on the tail change the shape of the tail changes slightly as well. Consequently, the performance of the tail is not linear. It is very close though and a linear fit is reasonable. Another assumption regarding the linear fit is that the y-intercept is equal to zero. This is a valid assumption since the tail has zero drag at zero velocity. To accomplish this, the data is biased to travel through zero although some error is present. Statistics pertaining to the accuracy of fit curves, and the parameters for the curves themselves, are given in Appendix A.

Using linear curve data then, with the rigid configuration as a baseline, and the body fixed (0 DOF), the flexible filament generates 14.5% more propulsive force (F_{R0}) and requires 11.5% more torque to drive (M_{R0}). When the body is free to move (2 DOF), the two configurations are virtually indistinguishable. The forward velocity (U) is 0.49% less, and the propulsive force is 0.52% less. In fact, the data is so close that the curves cannot be seperated when plotted (Figures 4.31 and 4.33). The body rotation rate is 2.94% greater as is the required driving torque. The efficiency of the system is 0.074%, compared to 0.077% for the rigid tail.

These results are incredibly positive in that they strongly support the flexible filament as a feasible propulsion system. The flexible filament, after contorting into a complete helix, has no discernible loss in performance compared to its rigid counterpart. It has yet to be shown, however, whether or not a complete helix can form since restrictions are still in place on the body.

The last configuration explored involves removing all restrictions on the body (6 DOF). The intent of this configuration is to simulate the final operating conditions of a free floating capsule propelled by a flexible filament. The motion of the head is dictated purely by drag forces and the forces exerted on it by the tail. In this configuration the transient, and steady-state behaviour of the filament are explored.

Figure 4.35 shows the position of the body and tail at the start of the simulation and 10 seconds into the simulation ($\omega = 2\pi$ $[rad/s]$). It can be seen that the flexible filament is successful. A helix is formed and propulsive force is generated. This is true for the entire speed range of interest ($\omega = 2\pi - 7\pi$ $[rad/s]$).

Further examination of Figure 4.35 illuminates a point of interest seen during the simulation. The body is moving along the positive y and negative z-axes. In fact, after reaching steady-state behaviour, the body, in general, is moving along the direction described by the tail in the start position. In other words, the body has aligned itself to the tail. The dominance the tail exerts over the body is also evident in the transient behaviour of the body. As the tail is formed, the body is pulled toward the relatively stationary tail, rather than remaining stationary as the tail curls. This is evident in the top view of Figure 4.36. The body starts at the origin but immediately tracks back into the north-east quadrant: toward the tail.

Since drag forces are largest here, the dominance of the tail is the opposite of what was expected. It was thought that the head would dominate, the tail would curl about the z-axis, and the final trajectory of the body would be along the negative z-axis. The absence of this situation is not a disadvantage though. In fact, it is speculated that this could be used as a steering mechanism

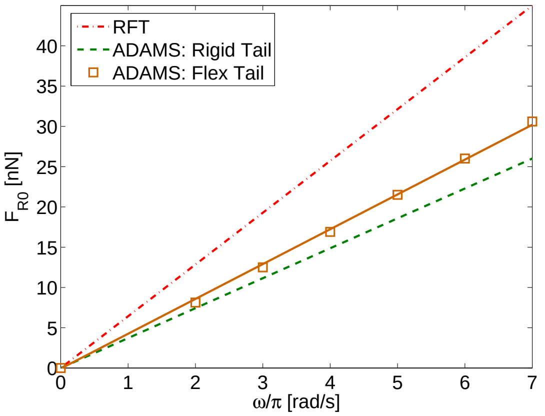

Figure 4.29: Propulsive Force (O DOF)

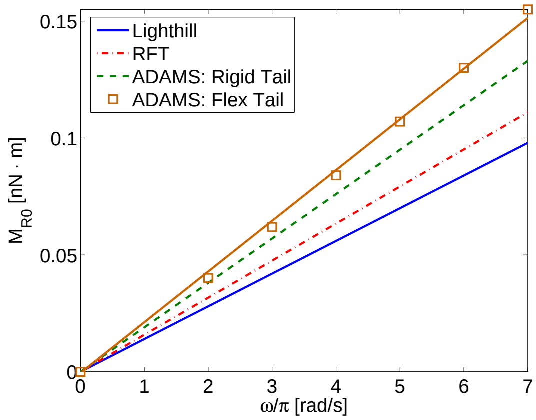

Figure 4.30: Driving Torque (O DOF)

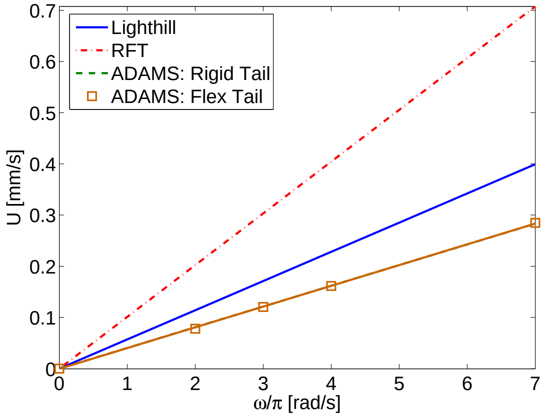

Figure 4.31: Forward velocity (2 DOF)

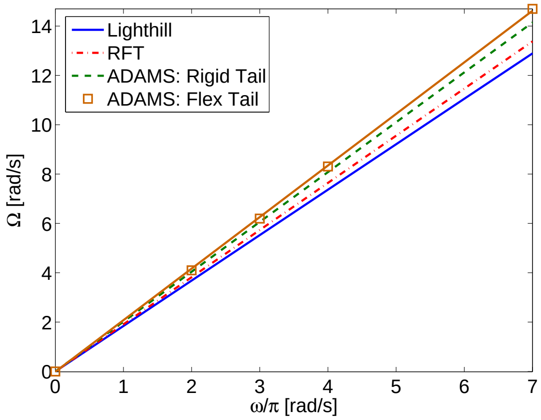

Figure 4.32: Rotation Rate (2 DOF)

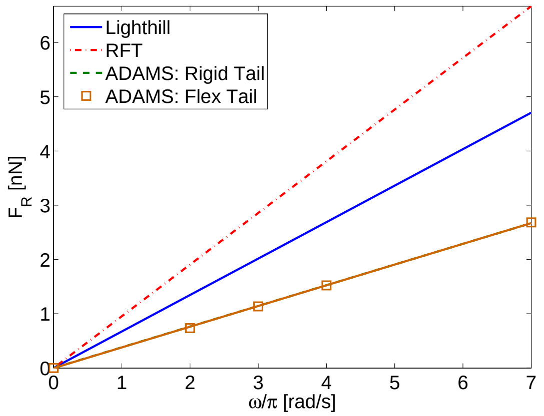

Figure 4.33: Propulsive Force (2 DOF)

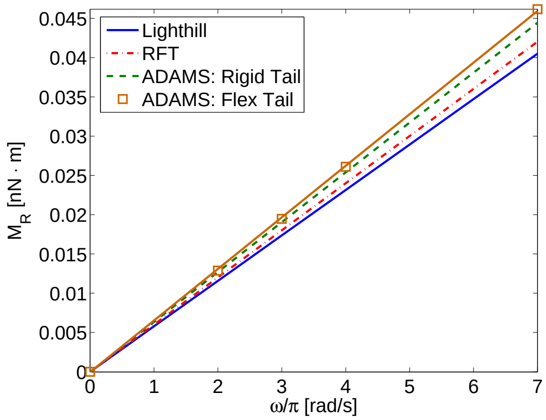

Figure 4.34: Driving Torque (2 DOF)

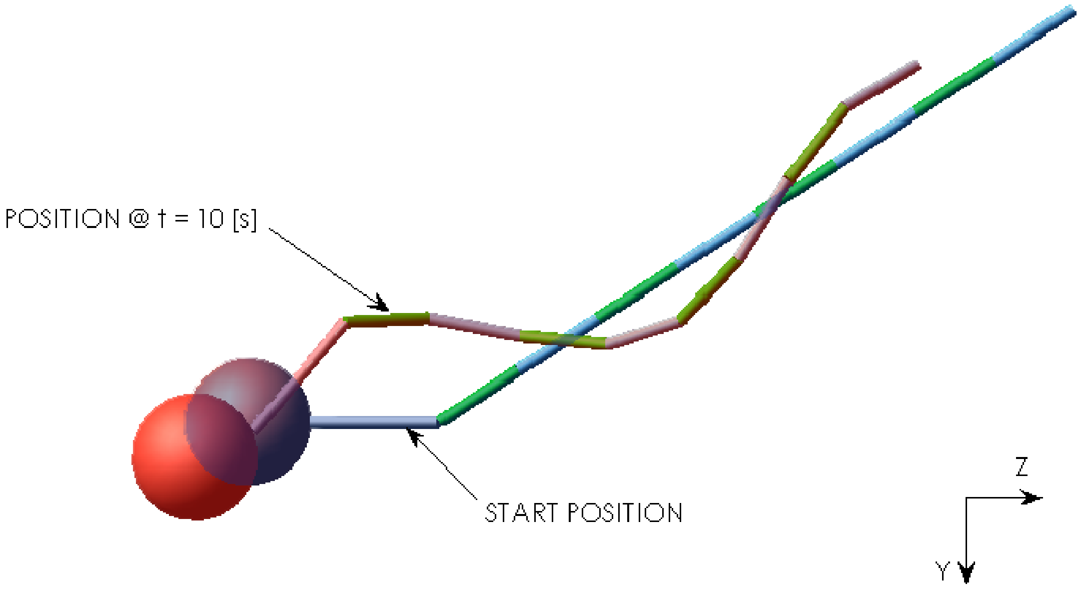

Figure 4.35: 6 DOF ADAMS model shown at t = 0 and t 10 [s]

for the final capsule. By changing the relative axis of rotation between the body and the tail, the final trajectory of the capsule could be modified.

If the trajectory of the body along the initial tail direction is considered the primary motion of the body, a secondary motion is the way the body traces the path of a helix about its primary direction of travel. This motion is clearly seen in all views of Figure 4.36. This helical motion is caused by the eccentric rotating mass of the rigid link. Accordingly, the amplitude of the helical motion increases as the rotational speed of the tail increases. This helical motion could be an issue for the system if it seriously effects forward propulsion. This aspect is discussed later in this section.

The ability of the filament to form a helix in this configuration is examined by performing the same analysis done for the other two configurations. Figure 4.37 shows the actual joint deflection angles, compared to the desired angles, with respect to time at $\omega = 2\pi\ [rad/s]$. A numerical comparison shows that the maximum difference is 11% and average difference is 5.4% (see Appendix A). This is an acceptable margin of error.

Figure 4.37 also shows how long it takes for the system to reach steady-state behaviour. Recall that in the 2 DOF, flex tail model, steady-state is reached in roughly 5-10 tail revolutions. For the 6 DOF model, steady-state behaviour is evident within 1-2 revolutions. The reason for this is that the body is now free to move in all directions and, since the tail dominates the body,

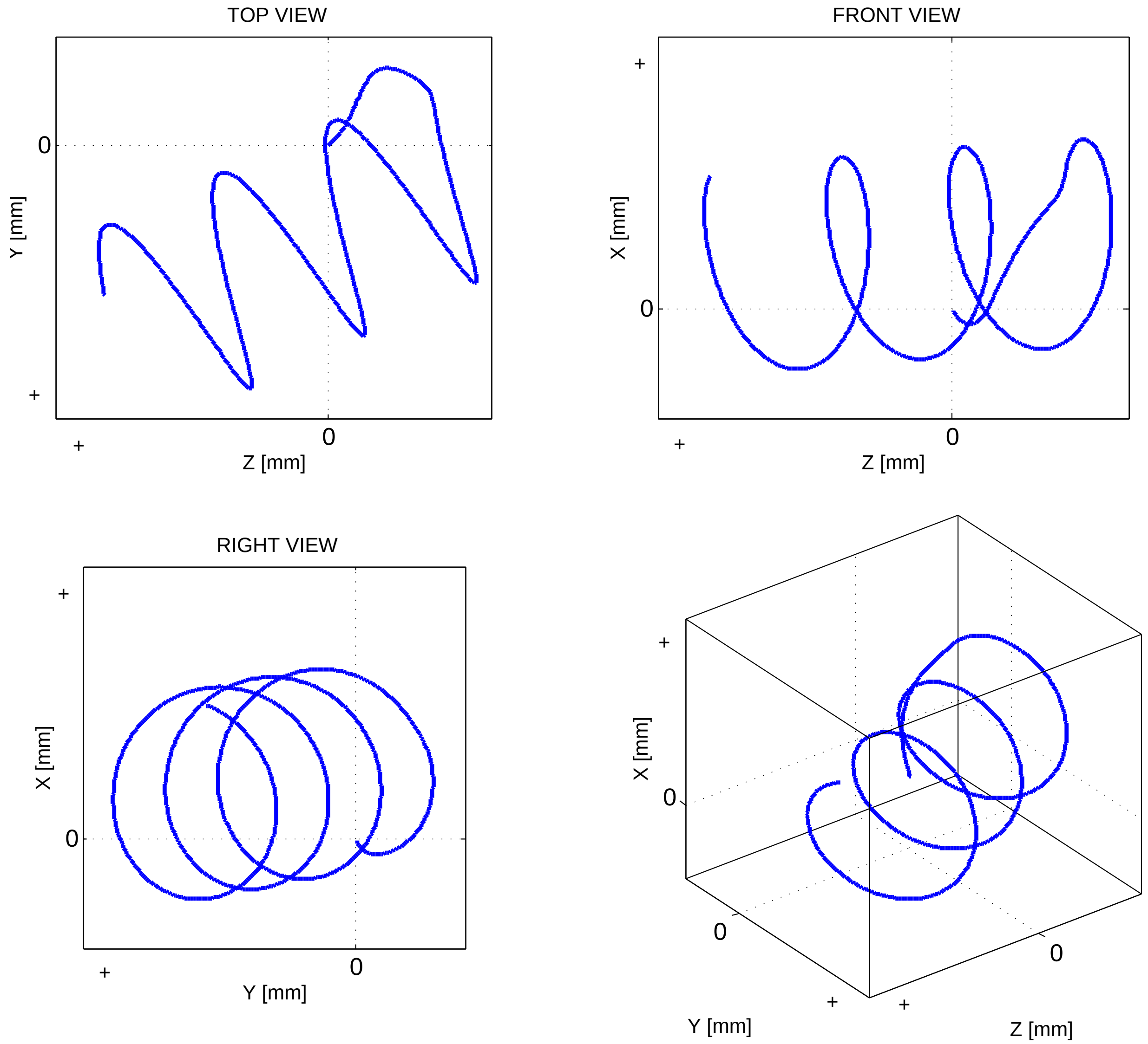

Figure 4.36: Body trajectory over 10 [s] simulation at $\omega = 2\pi$)

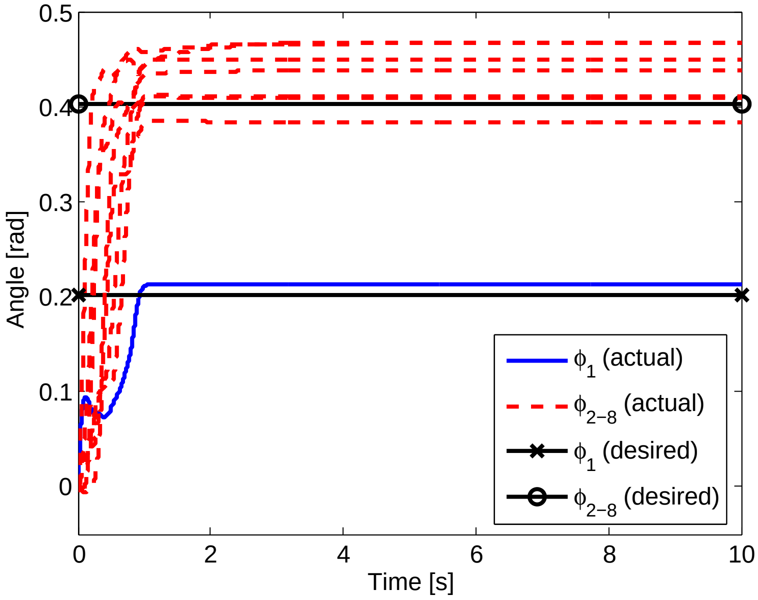

Figure 4.37: Joint deflection angles versus time: actual and desired

the body moves quickly into an equilibrium position. In the 2 DOF model, the tail has to move to equilibrium and consequently the process takes much longer.

To explore the performance of the tail in a 6 DOF situation, the forward velocity, body rotation rate, propulsive force, and required driving torque are measured and compared against the other two configurations and the analytical models. Once again the data collected is fit with a linear curve biased to travel through a y-intercept of 0. Data for these curves are given in Appendix A. Figures 4.38 – 4.41 show the comparison. The forward velocity (U) shows an increase over the 2 DOF configuration of 14.2% as a result of an increase in propulsive force (F_R) of 14.2%. The body rotation rate (Ω) and required driving torque (M_R) are both increased by 6.56%. The efficiency of the 6 DOF configuration is 0.095% compared to 0.077% for the rigid tail.

Once again the results are extremely positive. Even with the head completely free the flexible filament, with two-stage elastic stiffness, contorts into a complete helix under rotational load. Furthermore, there is no loss in performance when compared to an equivalent rigid tail. In fact, gains have been achieved in the key parameters of forward velocity and efficiency. It is speculated that these gains are a result of the marginally different steady-state deflection angles. However, it shows that the tail parameters are by no means optimized and this is a consideration for future work.

Also, the performance characteristics of the model show that the secondary helical motion of the head does not affect the forward velocity of the body. Therefore, unless this secondary motion is an issue for other systems, from a purely propulsive point-of-view, it is perfectly acceptable.

4.2.4 Summary

In the previous two sections, a lumped parameter multi-body dynamic model of the proposed propulsion system, as outlined in Section 3.6, is developed in ADAMS and evaluated. The purpose of this model is to characterise the steady-sate performance of the system as well as its transient behaviour.

First the ADAMS model is directly compared to two analytical models as outlined in Section 4.1. The results are not close enough to validate the ADAMS model in terms of quantitative accuracy. However, all three models give order-of-magnitude accurate results and as such, the ADAMS model is deemed acceptable from a qualitative view.

Second, the ADAMS model is modified to have a flexible tail yet the body is constrained according to assumptions made in the analytical models. The purpose of this configuration is to determine how the flexible filament performs compared to its rigid counterpart. The results show that the two versions are virtually indistinguishable.

Lastly, all constraints on the body are removed. This simulates the expected operational conditions of the system proposed in Section 3.6. Results from this simulation showed that even with the head free the flexible filament forms a complete helix that displays no loss in performance when compared to the rigid tail. This shows that the concept of a flexible filament propulsion system is feasible.

As a last note, an interesting observation from the final configuration is that the tail dominates the body. Accordingly, the final forward trajectory of the body is in-line with the initial direction of the tail. It is not, as was expected, in-line with the initial axis of rotation of the tail. It is hoped that the dominance of the tail over the body can be used to eventually develop a steering system.

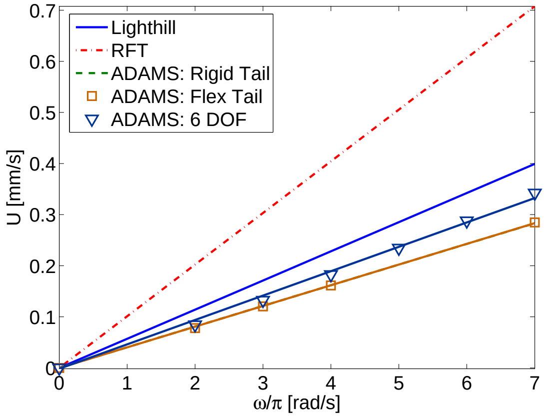

Figure 4.38: Forward Velocity

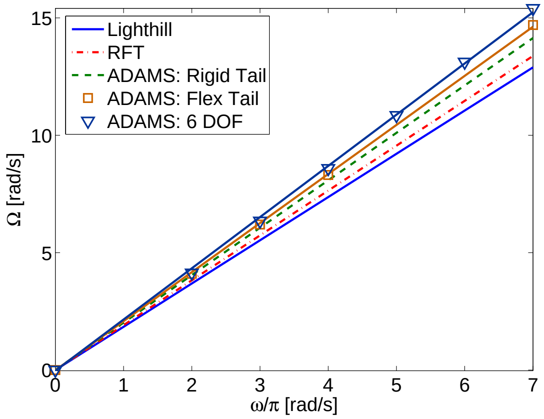

Figure 4.39: Body Rotation Rate

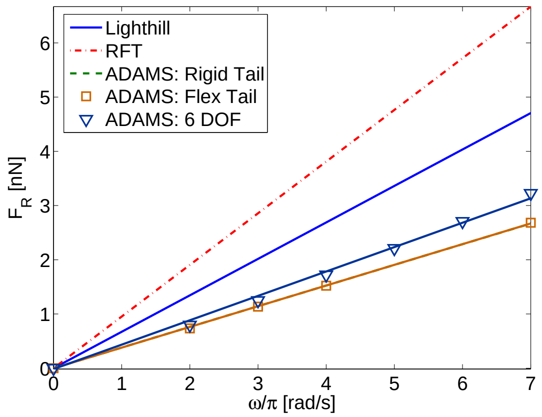

Figure 4.40: Propulsive Force

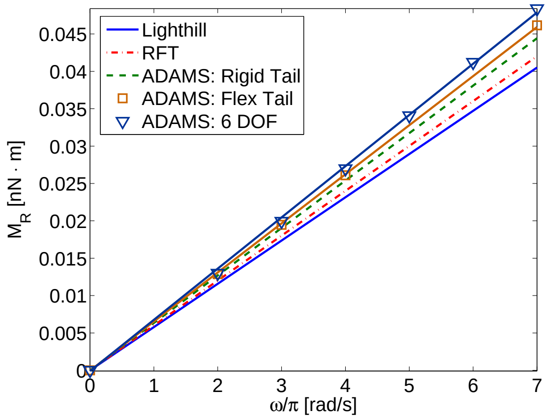

Figure 4.41: Driving Torque

4.3 Finite Element Model

The multi-body dynamic model outlined in Section 4.2 provides strong evidence supporting the feasibility of the flexible filament propulsion system. However, the simplifications made may cause uncertainty regarding the quantitative validity of the model. Consequently, it was decided that a finite element model (FEM) be created in an attempt to provide validation for the models previously developed.

The software package LS-DYNA is used to create the FE model. It is chosen because it has provisions for multi-body dynamics, fluid-structure interaction, and large deformation structures. However, the forte of LS-DYNA is its structural capabilities; the other two domains are recently introduced and are not advanced. Other software packages that may have been used include ANSYS-10 and the Immersed Boundary General Software Package (IBGSP) (see Section 4.3.2 for more information).

LS-DYNA constructs models from an input deck. The input deck is simply a text file containing input cards. Each card is a command read by LS-DYNA. Within each card is a series of values dictating the parameters for that particular card. For instance, a material model card might contain values for density, Young's modulus, and tensile limit. LS-DYNA itself is simply solver code for input decks. The input deck can be built by any number of third party pre-processing packages. For this work, FEMB Pre-Processor, a LS-DYNA specific pre-processor as built by ETA[3], is used.

The general make-up of a LS-DYNA input deck starts with control cards. These cards define parameters such as time-step size, simulation termination time, and various other simulation issues. The control cards are followed by the part, section, and material cards. For each part card a material and section must be defined. The material card defines the physical properties of the part (e.g. Young's modulus, material density, ...). The section card defines the finite element properties (e.g. constant stress solid element) of the part. The next section of the input deck contains cards specific to the model. For instance, in models with multi-body dynamics, the cards in this section would define the joints, initial velocities, and motions; the possibilities are virtually endless. The last section of the input deck contains the cards pertaining to node information and element information: the geometry of the model.

---

[3] Available for download from www.eta.com.

4.3.1 Model Setup

The finite element model simulates the configuration where the body is fully constrained (0 DOF). This was done because the model is less difficult to construct yet still allows for pertinent information to be drawn from it. A fully functioning, free-floating body model could be made if required, however, this would be extremely computationally expensive.

Since the body is fixed, the model must contain a ground. Accordingly, the ground is assigned to Part 1 (PID = 1) using the *PART card. The ground is constructed from a single beam element aligned with the z-axis. The section card (*SECTION_BEAM, SID = 1) defines the beam as a Hughes-Lie type with cross-section integration: the default configuration. However, this is simply a place-holder since the material card (*MAT_RIGID, MID = 1) over-rides the section properties and defines the part as rigid [55]. Also defined in the *MAT_RIGID material card is the degrees-of-freedom of the part. In this case the part is fully constrained and has no degrees of freedom (CMO = 1, CON1 = 7, CON2 = 7).

The *MAT_RIGID card requires the material density (ρ), Young's modulus (E), and Poisson's ratio (ν) to be specified. However, these values are, like the element specification, place-holders since the part is both fixed and rigid. If the beam were to come into contact with another part, these values would be used by the contact model. Regardless, the material chosen for the ground is brass, therefore the required values are as listed in Table 4.2.

Variable	LS-DYNA Card Label	Value
ρ_{brass}	RO	8545 $[kg/m^3]$
E_{brass}	E	101 $[GPa]$
ν_{brass}	PR	0.35

Table 4.2: Physical properties of brass

Part 2 (PID = 2) is the rigid link. In this instance, the part is a collection of rigid beam elements that attach from a common node to all the base nodes of the flexible filament. To define the part the *PART_INERTIA card is used. This card allows for the mass and inertia of the body to be directly defined rather than calculated from the geometry of the beams [55]. The mass and inertia information for the rigid beam, with respect to the coordinate system shown in Figure

4.42, is imported directly from a Solidworks model of the beam:

$$
\begin{aligned}
m_{rigid} &= 3.57\ [g] \\
I_{xx:rigid} &= 1.47 \times 10^{-7}\ [kg\ m^2] \\
I_{yy:rigid} &= 1.47 \times 10^{-7}\ [kg\ m^2] \\
I_{zz:rigid} &= 9.65 \times 10^{-9}\ [kg\ m^2]
\end{aligned}
$$

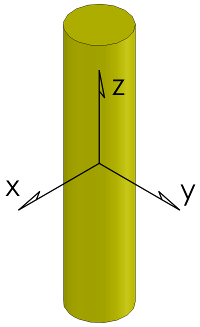

Figure 4.42: Rigid link Solidworks geometry

The section card for the rigid link is the same as the ground: *SECTION_BEAM (SID = 2). The default values are also used meaning that the beams of the rigid link are also classified as Hughes-Lie type beams. Like the ground, this is merely a place-holder because the material card (*MAT_RIGID, MID = 2) defines the beams as rigid. The only difference between the ground and the rigid link is the degrees-of-freedom allowed in the material card. To allow for rotation of the rigid link, the part has three degrees of freedom: z-rotation, x-translation, and y-translation (CMO = 1, CON1 = 3, CON2 = 4). The rigid link is made of brass so the other required material parameters are as listed above.

The rigid link (Part 2) and the ground (Part 1) are joined together using a revolute joint. This is done by using the *CONSTRAINED _JOINT _REVOLUTE card. Joints in LS-DYNA are implemented using the penalty method meaning that forces experienced by a joint are counteracted by forces generated by the software so that the constraint equations are adhered to. The constraint equations for each joint is defined in terms of its individual nodes. Furthermore, only the the translational degrees of freedom are used in the constraint equations. Accordingly, a revolute joint is constructed by adding together two spherical joints [55].

The desired motion of the tail assembly is accomplished by prescribing a motion to the rigid link (Part 2) using the *BOUNDARY _PRESCRIBED _MOTION _RIGID _ID card. Within the card, the part is specified (PID = 2), as is the degree of freedom (DOF = 7, Z-Rotation), the type of motion (VAD = 0, Velocity), and finally the load curve for motion (LCID = 1).

The load curve for motion is a curve card (*DEFINE_CURVE) that defines a generic curve. For motions, the load curve describes the motion value to be used with respect to time. The motion value can either be displacement, velocity, or acceleration as set by the VAD parameter. LS-DYNA constructs a load curve by linearly interpolating between given data points. For this instance, the load curve is simply a constant value with time. The magnitude of the value is arbitrary but should be in line with the speed range of interest as set in Section 4.1.3.

To reduce the shock on the system, the rigid link is given an initial velocity. This is implemented using the *INITIAL _VELOCITY _RIGID _BODY card. The card requires that the part be specified (PID = 2) and that the initial velocity, in the desired direction, be given. The card has provisions for motion in all six possible directions. To specify rotation about the z-axis, the appropriate flag must be non-zero (e.g. VZR $\neq$ 0). To be consistent with the aforementioned prescribed motion, the value for VZR should be equal to the initial load curve value.

The third part (PID = 3) of the LS-DYNA model is the flexible filament. It is created using the *PART card. This means that its mass and inertial properties are calculated by the software. The filament is modeled as a continuous structure with the same geometry as outlined in 3.6. To create this geometry, a Solidworks model is created and the data is imported into FEMB. The geometry is then used to create a mesh of eight-sided, solid elements. The section card (*SECTION_SOLID, SID = 3, ELFORM = 1) for the filament dictates that each solid element acts as a constant stress solid element. Also created for the flexible filament part is an *HOURGLASS (HGID = 1) card. This card implements hourglass control on the part in an attempt to control any zero-energy modes that may arise in the part [55]. Hourglass control is recommended on any part using single point integration solid elements.

The material for the flexible filament is a representation of Dow Corning® 3112 silicone RTV rubber based on the Arruda-Boyce (or eight-chain) rubber model (*MAT _ARRUDA _BOYCE _RUBBER, MID = 4). The material was used because of its availability at the research facility and its suitability for creating a prototype filament (see Chapter 5). The material model was chosen because it has the ability to accurately predict the equilibrium behaviour of rubbers experiencing large strain [56].

The Arruda-Boyce rubber model, as implemented in LS-DYNA, requires that the material density (ρ), shear modulus (G), number of statistical links (N), and bulk modulus (K) be specified. The material density is listed taken from the product literature as $\rho_{3112} = 1300$ $[kg/m^3]$. Ngai *et. al.* claim that the Young's modulus for the material is approximately 2.6 $[MPa]$ [57]. For the other required parameters, Bergström provides a graphical technique by which experimental data can be used to approximate the required parameters [56]. Figure 4.43 shows the results of compression testing (load to 25% strain at 0.07 mm/s) on three material samples. The results have been plotted in as stretch versus true stress as required by Bergström. Then, according to the procedure:

Variable	LS-DYNA Card Label	Value
G_{3112}	G	0.87 $[MPa]$
K_{3112}	K	87 $[MPa]$
N_{3112}	N	3

Table 4.3: Approximate physical properties of Dow Corning® 3112 silicone RTV rubber

The flexible filament is also given an initial velocity in an attempt to reduce shock in the system. For non-rigid bodies, an initial velocity is assigned using the *INITIAL _VELOCITY _GENERATION card. The procedure by which the motion is assigned is different than the rigid body. First, the part is identified (PID = 3). Then, for angular rotations, the rate of rotation is defined (OMEGA $\neq$ 0), and a rotation vector is defined by specifying a point and a direction. For the model created, the desired vector is along the z-axis and through the origin. Therefore, to define this vector in the card, the only parameter to be set, other than the rate of rotation, is the value of the z-axis direction cosine: NZ = 1.

Together the ground, rigid link, and filament simulate the proposed propulsion system. The three together can be seen in Figure 4.44. The fourth part of the model, defined by the *PART card (PID = 4), is the fluid. It is a cube of eight-side elements that engulfs the rigid link and filament. The material card for the fluid is *MAT_NULL. This material card informs the software that an equation of state should be called instead of calculating the deviatoric stresses in the element [55]. A required parameter of the *MAT_NULL card is the material density (RO) which, for water, is $RO = 1000\ [kg/m^3]$. The *MAT_NULL also allows for a viscosity coefficient (MU) to be specified. This value is the same as was used in the other models: MU = 0.001 $[Pa \cdot s]$.

The equation of state for a fluid defines the pressure in the material as it is compressed. For this model, the *EOS _GRUNEISEN card is used to define a Mie-Gruneisen equation of state (EOS). Although the forte of this EOS is its ability to simulate pressure as shock waves ripple through a material it is valid for slow strain rates as encountered in this model [58]. The values required for the EOS, as listed in Table 4.4, are the speed of sound in the material (C), and two Gruneisen constants (S and γ).

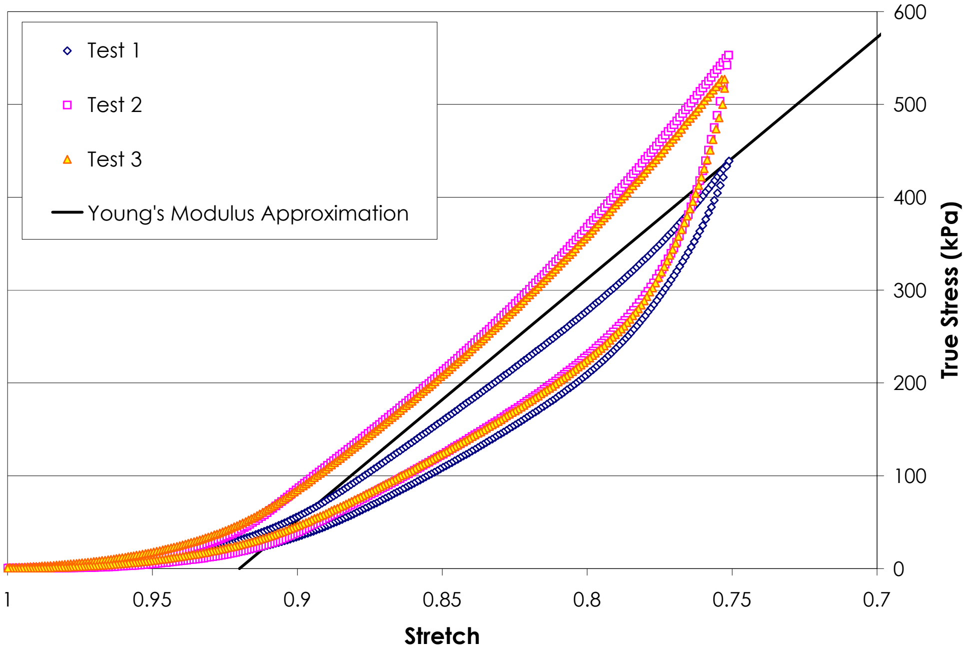

Figure 4.43: Compression testing of 3112 silicone RTV rubber

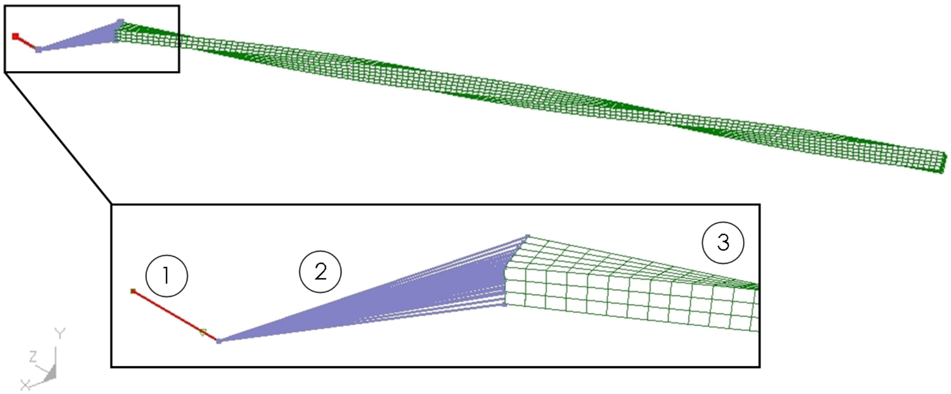

Figure 4.44: FEM model showing 1) Ground, 2) Rigid Link, and 3) Flexible filament (fluid not shown)

The section card for the fluid (PID = 4) defines the elements as single point Arbitrary Lagrangian-Eulerian (ALE) solid elements (*SECTION_SOLID, SID = 4, ELFORM = 5). Using this distinction means that the solid will be treated with an ALE formulation meaning, in simple terms, that material is allowed to flow from one element to another. The formulation accomplishes this by first allowing the mesh to deform and then stopping the calculations. At this point an advection step calculates the amount of material transported between elements and then remaps the mesh to its original position. Calculations are then restarted. In this way, a fluid can flow through a mesh thus simulating a control volume.

The ALE formulation is controlled using the *CONTROL _ALE card. In the card, two parameters need to be set: the continuum treatment, and the cycles between advection. The continuum treatment parameter is set such that the fluid is treated with the ALE formulation: therefore DCT = 3. The number of cycles between advection is set (NADV = 2) so that advection happens after every other Lagrangian step. This is done to reduce the computational time since typically the advection step costs 2-5 times more than the Lagrangian step [55].

Coupling of the fluid to the filament uses the *CONSTRAINED _LAGRANGE _IN _SOLID card. In this card, the slave Lagrangian part (filament, PID = 3) and the master solid part (fluid, PID = 4) are identified. The type of coupling is identified using the CTYPE flag. In this instance a penalty coupling is used (CTYPE = 4, Penalty Coupling). The penalty coupling algorithm tracks the distance between nodes on the filament and a point in the fluid. A force, proportional to this distance, is applied to both parts, in equal and opposite directions [59]. The proportionality constant is based on the constitutive material properties of the slave part. In this way, drag on the body is simulated.

There are two other cards used in the model to perform certain functions. The simulation termination time is set by the *CONTROL _TERMINATION card by setting the ENDTIM flag to a non-zero value. The timing interval for graphical output for the model is set using the *DATABASE _BINARY _D3PLOT card. The time between graphical output frames is set by modifying the DT/CYCL flag to a non-zero value.

Variable	LS-DYNA Card Label	Value
C_{water}	C	1650 $[mm/ms]$
S_{water}	S1	1.92
γ_{water}	GAMA0	0.1

Table 4.4: Mie-Gruneisen equation of state parameters for water

4.3.2 Results and Discussion

The model is run over the speed range required starting with $\omega = 2\pi$ $[rad/s]$: initial velocities are set accordingly. The model consists of 1 rigid beam element for the ground, 24 rigid beam elements for the rigid link, 2250 hexagonal, solid elements for the flexible filament, and 5120 hexagonal, solid elements treated with the ALE formulation for the fluid. 24 rigid beam elements are used for the rigid link so that the base of the flexible filament is well supported.

To reduce simulation time, the simulation is initially set to run for 250 $[ms]$. The initial time-step for the simulation is set automatically by the software at 7.54×10^{-5} $[s]$. This value is dynamic and will change as required by the software. The deciding factor for the time-step is such that no pressure wave will travel through an element in a time-step. Therefore, the time-step is limited by the smallest element and the maximum speed a wave can travel through that element [55]. Eventually, for full comparison to the ADAMS model, a 10 $[s]$ simulation will be required. For this work, however, this was not done since the results from the FEM are very disappointing.

The FE model fails to run successfully almost as soon as the simulation begins. Problems begin with the velocity distribution of the fluid. Figures 4.45 – 4.48 show four frames, with velocity vectors shown, from the first 2.1 $[ms]$ of simulation. At $t = 0$ $[s]$ the rigid link and filament are moving at the initial velocity and the fluid is completely stationary. Over the next two frames (Fig. 4.46 and 4.47) the fluid begins to stir slightly but the velocities are very low. However, during the 7 $[ms]$ jump between Figure 4.47 and 4.48 the fluid velocity profile develops as if an explosion has occurred in the middle of the control volume. This is very different from the expected behaviour. The fluid should, in a pattern that propagates out from the filament, slowly gain momentum as time progresses. The final behaviour of the fluid should be, as intuition suggests, like when one stirs a pot: a vortex-like pattern propagating out from the rotating object.

Further problems with the model are evident by observing the flexible filament. Figure 4.49 shows a close up progression of the filament as it rotates. It can be seen that, by 50 $[ms]$, the elements near the base of the filament are drastically, yet very locally, deformed. It was expected that the entire filament would undergo minor deformation and not experience the localized deformation seen. The deformation appears to be similar to hourglassing and this may indicate that the *HOURGLASS card needs modification.

Another possible reason for the drastic deformations is the presence of higher than expected forces. In fact, nodal forces obtained during post-processing estimate that the forces are 5–10 times greater than the forces predicted by the ADAMS model. A positive note from this analysis is that the material model is most likely correct. However, what is causing the large forces?

There are two suspected causes or, at the very least, avenues to explore.

The first possible cause is the coupling algorithm responsible for the fluid structure interaction. As mentioned, the coupling algorithm applies a force to a filament node based on the distance it has traveled from a point in the fluid mesh. The magnitude of the force is set using a proportional gain based on the material models (fluid and structure). It is possible that this proportional gain is tuned for pressure drag based system (e.g. large Reynolds number flow). In that case, the forces applied to a filament under low Reynolds number flow could be grossly inaccurate.

The second possible cause is the boundaries of the fluid part. The fluid control volume is large enough that it envelopes the entire filament. That said, the control volume should simulate a semi-infinite environment and, considering the properties of low Reynolds number flow, is not large enough to do so. The reason the control volume is not made larger is because of the computation cost. The advection step required for the ALE formulation is expensive. As is, the simulation takes roughly 9 hours on a P4, 3.2 GHz, 1 Gb RAM, desktop PC for roughly 80 [ms] of simulation time. Increasing the size of the mesh until a semi-infinite environment is properly modeled would make simulation times too large to be feasible. Therefore, since the control volume is undersized, if the software does not treat the boundary as if it were attached to more fluid the accuracy of the model would be seriously affected.

There is evidence that the required boundary conditions are not being adhered to. The model fails to run past the 80 [ms] mark due to an error citing a negative volume in one of the boundary fluid elements. It is speculated that the boundary is not allowing for more material to be drawn into this element and, as such, the element reaches a zero density state causing the error.

It should be noted that these avenues have been investigated by the author; however, inexperience with finite element code in general has proven to be a road-block. A person with more experience in the field may be able to adequately simulate the flexible filament. If so, it could prove to be a very useful design tool for future, filament-based, propulsion systems.

There may arise the possibility that LS-DYNA is not able to solve this problem correctly. If so, other software could be explored and a strong option is the Immersed Boundary General Software Package (IBGSP). Developed by researchers at the Courant Institute of Mathematical Sciences at New York University, the IBGSP is free for academic use. This software is tailored for simulating flexible bodies immersed in a semi-infinite fluid medium and has been used to solve similar problems as this [60]. It could be valuable in creating a continuous model of the flexible filament. The IBGSP was not used for this work because it was discovered too late in the project time line. However, a copy was procured and is available at the research facility.

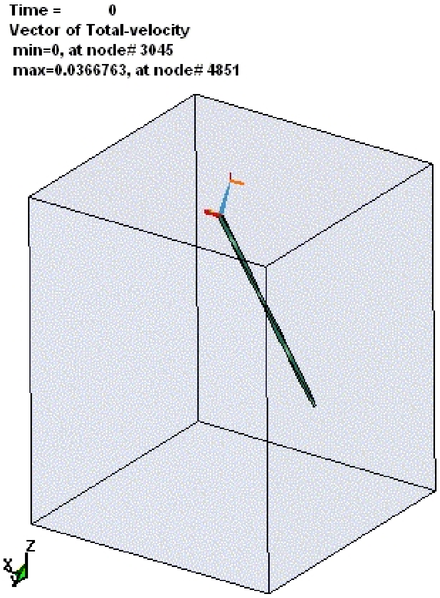

Figure 4.45: t = 0 [ms]

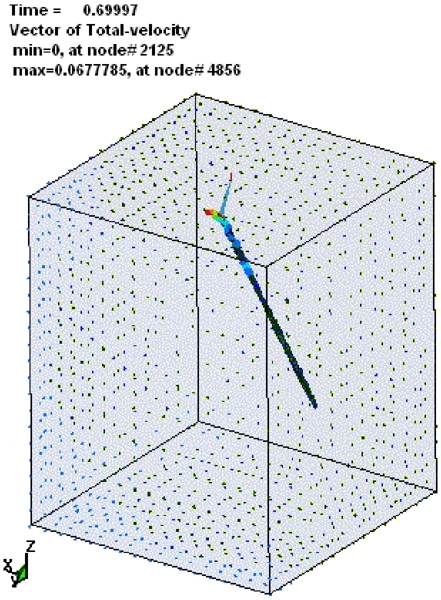

Figure 4.46: t = 7 [ms]

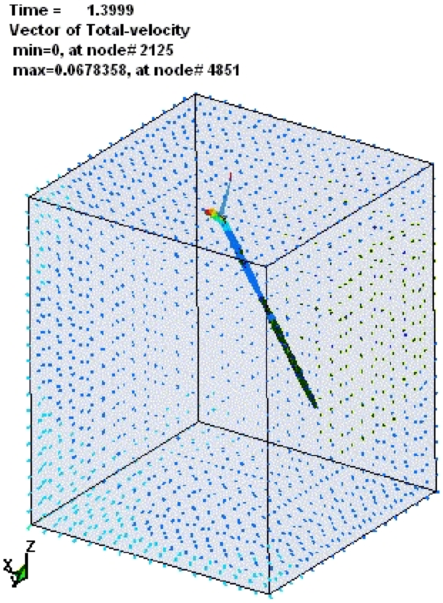

Figure 4.47: t = 1.4 [ms]

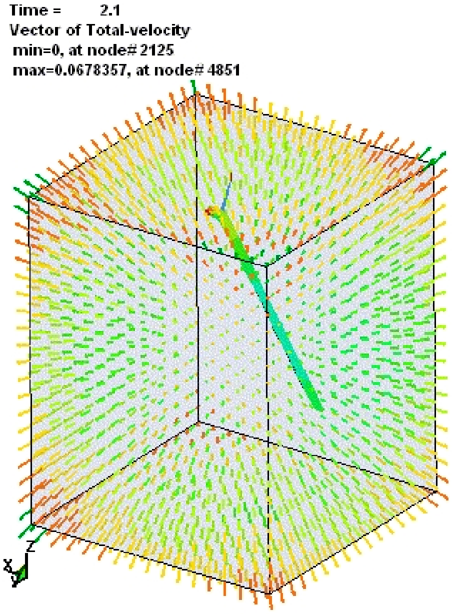

Figure 4.48: t = 2.1 [ms]

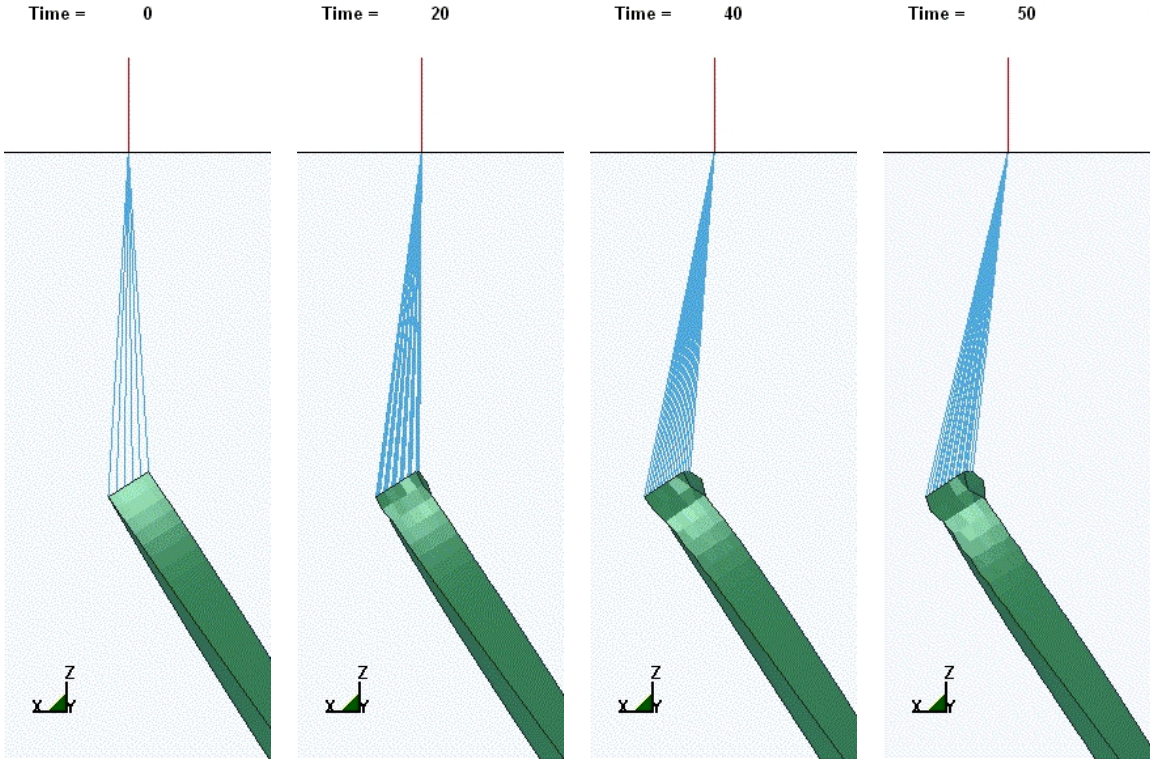

Figure 4.49: LS-DYNA simulation from 0–50 [ms]

Chapter 5

Experimental Validation

Without a physical system to establish the real-world behaviour of the design, the results generated by the models outlined in the previous chapter are useless as a design tool. Accordingly, a test bench was built to explore the behaviour of the system proposed in Chapter 3. Also explored is the performance of a rigid tail design and a simplified flexible filament design.

Due to the difficulty of developing a complete swimming robot, it was decided that the test bench use a fixed body. Accordingly, the swimming velocity (U), and rotational speed (Ω) of the body are equal to 0 and only the propulsive force (F_{R0}) and required driving torque (M_{R0}) are measured.

5.1 System Scale

At roughly 6 [mm] long and only 0.12 [mm] in diameter, the flexible filament proposed in Chapter 3 cannot be manufactured using common techniques. Also, a suitably sized actuator to rotate the filament is not readily available. Furthermore, the forces predicted in Chapter 4 are so small that measuring them would be very difficult. To eliminate these challenges, the size of the system is scaled up to a more manageable level.

However, scaling of the geometric parameters cannot be done without modifying the other system variables. This is evident in Section 4.2.2 where the ADAMS model was scaled up to circumvent software limitations. Unfortunately, the same scaling technique cannot be used here because of real-world limitations. In the virtual world any parameter can easily be modified by any amount; in the real world this is not the case. For instance, in Section 4.2.2 length is scaled by 1000, which then requires density to be scaled by 1×10^{-9}. In a physical sense, this would require materials lighter than air. Consequently, a different scaling technique called dimensional analysis must be used.

Dimensional analysis allows for a system to be condensed from an original list of variables into a minimal list of non-dimensional combinations of variables called dimensionless products. The basic theorem of dimensional analysis is called the Buckingham Pi Theorem. It states that [43]:

> If an Equation involving k variables is dimensionally homogeneous, it can be reduced to a relationship among $k - r$ independent dimensionless products, where r is the minimum number of reference dimensions required to describe the variables.

The dimensionless products are called the ‘Pi terms’ and are denoted by Π. The process by which the Pi terms for a given system are procured is well described in many texts (see [43] as example) and as such is not described here.

In terms of experimental validation, the useful property of the Pi terms is their similitude between systems of different scales. Consider the flexible filament propulsion system proposed in Chapter 3; it is desired to compare a physical version of this system to the analytical and ADAMS models developed in Chapter 4. As mentioned, developing the physical system at the original scale is very difficult. However, it is assumed that the system can be built, denoted by the letter A, and described by the following Pi terms:

$$\Pi_{1A} = \Phi(\Pi_{2A}, \Pi_{3A}, ..., \Pi_{nA}),$$

where Π_{1A} is a function (Φ) of the other Pi terms. Now consider a scaled version of the same system, denoted by the letter B, described by the Pi terms:

$$\Pi_{1B} = \Phi(\Pi_{2B}, \Pi_{3B}, ..., \Pi_{nB}).$$

Under the following conditions:

$$\begin{aligned} \Pi_{2A} &= \Pi_{2B}, \\ \Pi_{3A} &= \Pi_{3B}, \\ &\vdots \\ \Pi_{nA} &= \Pi_{nB}. \end{aligned}$$

and, assuming that the form of Φ is the same for both systems, it follows that [43]:

$$\Pi_{1A} = \Pi_{1B},$$

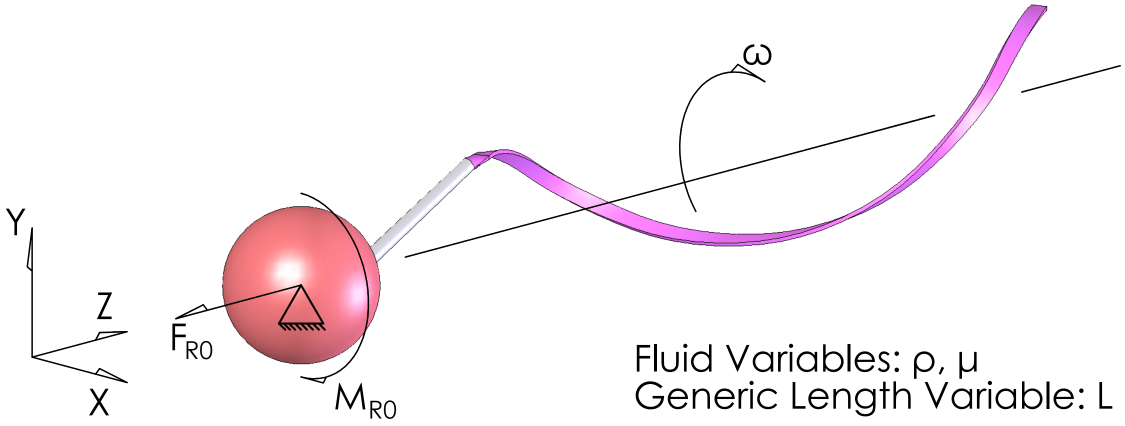

Figure 5.1: Generic system layout

thus indicating that the measured value of Π_{1B} obtained from System B will be equal to the corresponding Π_{1A} of System A as long as the other Pi terms are equal. Accordingly, we can consider the system as shown in Figure 5.1.

As previously mentioned, only the propulsive force and the driving torque are considered since the head is fixed. In the absence of external forces, these forces are generated by drag on the body and are functions of the geometry (L as a generic length term), the fluid density (ρ), the rotational velocity of the shaft (ω), and the fluid viscosity (μ) as shown in Equation (5.1) [43].

$$\begin{aligned} F_{R0} &= f_1(L, \rho, \omega, \mu), \\ M_{R0} &= f_2(L, \rho, \omega, \mu). \end{aligned} \tag{5.1}$$

Applying the Buckingham Pi theory, with L, ρ, and ω, as the repeating variables results in the following:

$$\begin{aligned} \Pi_2 = \Phi(\Pi_1) &\rightarrow \frac{F_{R0}}{\rho\omega^2 L^4} = \Phi\left(\frac{\mu}{\rho\omega L^2}\right), \\ \Pi_3 = \Phi(\Pi_1) &\rightarrow \frac{M_{R0}}{\rho\omega^2 L^5} = \Phi\left(\frac{\mu}{\rho\omega L^2}\right), \end{aligned}$$

which gives the similarity requirements for scaling the proposed system as:

$$\frac{\mu_A}{\rho_A \omega_A L_A^2} = \frac{\mu_B}{\rho_B \omega_B L_B^2}, \tag{5.2}$$

$$\frac{F_{R0A}}{\rho_A \omega_A^2 L_A^4} = \frac{F_{R0B}}{\rho_B \omega_B^2 L_B^4}, \tag{5.3}$$

$$\frac{M_{R0A}}{\rho_A \omega_A^2 L_A^5} = \frac{M_{R0_B}}{\rho_B \omega_B^2 L_B^5}. \tag{5.4}$$

Using these similarity requirements, a test bench prototype of the proposed system can be made at any scale. Then, by modifying the other variables in the system and scaling measurements accordingly, the test bench system can be used to represent a smaller scale system which, in turn, can be compared to the models presented in Chapter 4. The development of such a test bench system is outlined in the following section.

5.2 Test Bench Setup

The following section outlines the creation of a test bench used to gather results on a large scale prototype of the flexible filament propulsion proposed in Section 3.6. Also tested is a simplified (constant cylindrical cross-section) version of the flexible filament and a rigid helix version of the tail. The rigid tail provides a benchmark for the two flexible designs. The simplified flexible filament is tested to determine the importance of the criteria required to form a helix as outlined in Section 3.6.1. Covered in this section is the determination of the scaling parameters, the fabrication of the tails, the design of the apparatus to facilitate force measurement, an analysis of possible wall effects, and motor control.

5.2.1 Scaling

The first step in designing the test bench is to determine its scale. So that the test bench could be built using common manufacturing techniques, it was decided that the test bench be twenty times larger than the proposed system. Based on this scaling factor, Table 5.1 shows the original system dimensions, denoted by the letter A, compared to the test bench dimensions, denoted by the letter B (Fig. 4.1 for variable definitions). The twenty times scaling factor corresponds to the following relationship for the generic length variable (L):

$$L_B = 20 L_A. \tag{5.5}$$

Variable	**System** A	**System** B
λ	5 $[mm]$	100 $[mm]$
b	0.5 $[mm]$	10 $[mm]$
a	0.06 $[mm]$	1.2 $[mm]$

Table 5.1: Comparison of original system (a) and scaled test bench system (b) geometry.

With the geometric scaling factor set, the Pi terms can now be evaluated to determine the required values of the system variables. Recall that the values for the proposed system are:

$$\begin{aligned}\rho_A &= 1000\ [kg/m^3],\\ \mu_A &= 0.001\ [Pa/s],\\ \omega_A &= 0 - -7\pi\ [rad/s],\end{aligned}$$

where ρ is fluid density, μ is fluid viscosity, and ω is the rotational velocity of the tail. Accordingly, a fluid must be chosen and a speed range set for the test bench that ensures the similarity requirement is met. To do so, assume that the velocity range and fluid density is the same for both systems. The first assumption is valid as the velocity range is fully controllable. The second assumption is also valid as the density of many fluids differs little from that of water. Equation (5.5) is then substituted into Equation (5.2) and the results rearranged to solve for the desired test bench fluid viscosity (μ_B):

$$\mu_B = \left(\frac{\cancel{\rho_B}}{\cancel{\rho_A}}\right)\left(\frac{\cancel{\omega_B}}{\cancel{\omega_A}}\right)\left(\frac{20L_A}{L_A}\right)^2 \mu_A.$$

Therefore, the desired test bench fluid viscosity is 400 times that of μ_A. However, it is also desired that the fluid be readily available. Accordingly, Shell Tellus® 100 hydraulic oil was chosen as it was available at the research facility. It has the following properties (Appendix B):

$$\begin{aligned}\rho_B &= 875\ [kg/m^3],\\ \mu_B &= 0.299\ [Pa/s] \text{ at } 20^\circ\text{C}.\end{aligned}$$

Since the oil viscosity is not 400 times that of μ_A, and the two fluid densities are not equal, Equation (5.2) must be re-evaluated to solve for the only unknown left, ω_B.

$$\begin{aligned}\omega_B &= \left(\frac{\rho_A}{\rho_A}\right)\left(\frac{\mu_B}{\mu_A}\right)\left(\frac{L_A}{L_B}\right)^2 \omega_A,\\ \omega_B &= 0.853\omega_A.\end{aligned} \tag{5.6}$$

In summary, to ensure similarity between the test bench and the proposed system, the test bench, at 20 times scale, is to be run in Shell Tellus® 100 oil at 85.3% speed.

With the variables defined, the scaling factors pertaining to the propulsive force and required driving torque can be evaluated. First, Equation (5.3) is rearranged to determine the scaling factor for the propulsive force:

$$\begin{aligned} F_{R0A} &= \left(\frac{\rho_A}{\rho_A}\right)\left(\frac{\omega_A}{\omega_B}\right)^2\left(\frac{L_A}{L_B}\right)^4 F_{R0B}, \\ F_{R0A} &= \frac{1}{102236} F_{R0B}. \end{aligned} \tag{5.7}$$

This indicates that forces measured on the test bench are 102236 times larger than those generated by the proposed system. Similarly, Equation (5.4) is also rearranged to determine the scaling factor for driving torque:

$$\begin{aligned} M_{R0A} &= \left(\frac{\rho_A}{\rho_B}\right)\left(\frac{\omega_A}{\omega_B}\right)^2\left(\frac{L_A}{L_B}\right)^5 M_{R0B}, \\ M_{R0A} &= \frac{1}{2044716} M_{R0B}. \end{aligned} \tag{5.8}$$

Here, it can be seen that test bench torque values are 2044716 times larger than those generated by the proposed system. The large scaling factors for torque and force are positives since it means that the values generated by the test bench are in a range that is easier to measure.

5.2.2 Tail Fabrication

With the scale of the test bench in place, and the required scaling factors determined, the physical side of the test bench can be considered beginning with the rotary actuator. The test bench uses a DC motor (model number: 0816P006S) procured from MicroMo Electronics of the Faulhauber Group. Attached to the motor, to reduce speed and increase torque, is a Series 08/1 64:1 planetary gear-reducer. Also attached to the motor, to allow for closed loop control, is a HEM1016, 10 cycle per revolution, magnetic digital encoder. For more information on these three components, see Appendix B.

The motor/gearhead/encoder combination was chosen for two reasons. First, the small package size fits well with the scale of the test bench. The motor and gearhead have a diameter of only 8 [*mm*]; the encoder diameter is 10 [*mm*]. The components stack together to make a package 43.3 [*mm*] long.

The second reason is the capabilities of the motor match well with the requirements of the test bench. The motor has a maximum recommended torque rating of 0.15 [*mNm*]. Coupled with the 64:1 ratio in the gearhead, at an efficiency rating of 70%, the motor/gearhead package can deliver a maximum recommended torque of 6.72 [*mNm*]. Figure 4.29 estimates the maximum required driving torque for the proposed system at 0.15×10^{-6} [*mNm*]. This value, when modified by the moment scaling factor calculated in Equation (5.8), estimates that the test bench will require approximately 0.30 [*mNm*] of driving torque. Therefore, the motor/gearhead package has sufficient torque to drive the test bench.

Similarly, the maximum recommended operating speed for the motor is $13,000$ [*rpm*]. The proposed system is analyzed through a speed range of 7π [rad/s]. Modifying this number by the scaling factor for speed listed in Equation (5.6), and accounting for the 64:1 speed reduction, the test bench motor is to be operated at an approximate maximum rotational velocity of $11,500$ [*rpm*] — an acceptable value.

The next section of the test bench to consider is the tail. It was decided to test three possibilities. The first is a rigid helix intended to provide a benchmark for the two flexible designs. The second is a flexible filament with a simple cylindrical cross section (Flex Tail: Cyl). The third is the flexible filament with a twisting, rectangular, cross-section as proposed in Chapter 3 (Flex Tail: Rec).

The rigid helix is fabricated out of 2.38 [*mm*] ($3/32$ [*in*]) diameter aluminum rod bent to match the required helix shape. The diameter of the aluminum rod is 99% of the filament diameter used in the ADAMS model. The difference between this and the desired 20 times scaling factor is small enough that negligible error is expected. The aluminum rod is used because it is readily available at the research facility.

A sensitivity analysis conducted using the rigid tail ADAMS model supports the claim that error should be negligible. With all other parameters held constant, the filament diameter is varied. The results show that a 1% increase in filament diameter leads to approximately 0.5% difference in propulsive force.

A bending die is built to ensure that the shape is correct (λ and a). It should be noted that, although a bending die is used, the imprecision of the manufacturing technique will cause the helix to be slightly different from the desired shape. However, once again, the difference is small enough that the error should be minimal. The initial rigid link of the tail is created by bending the aluminum rod to the desired shape. The base of the rigid link is glued to a brass motor couple designed to mate with the gearhead. Brass was chosen because of its availability at the research facility. A set screw holds the tail assembly to the motor. Figure 5.2 shows the rigid tail.

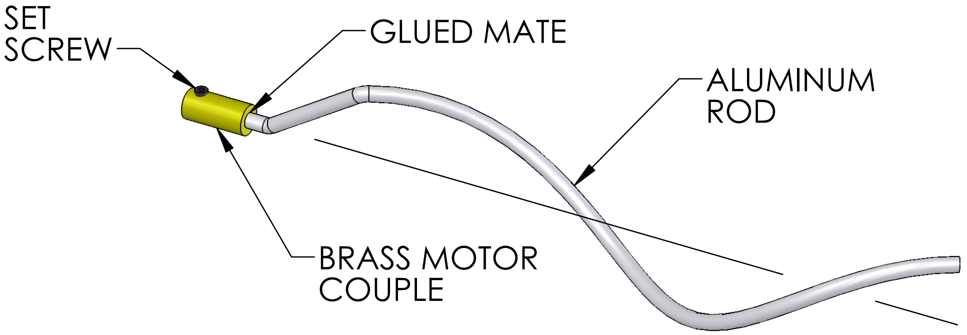

Figure 5.2: Rigid tail assembly

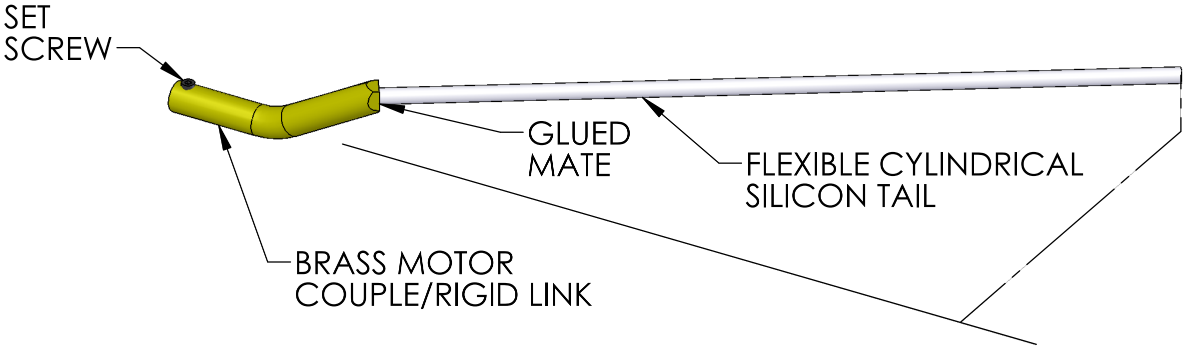

Figure 5.3: Flexible, cylindrical cross-section tail assembly (Flex Tail: Cyl)

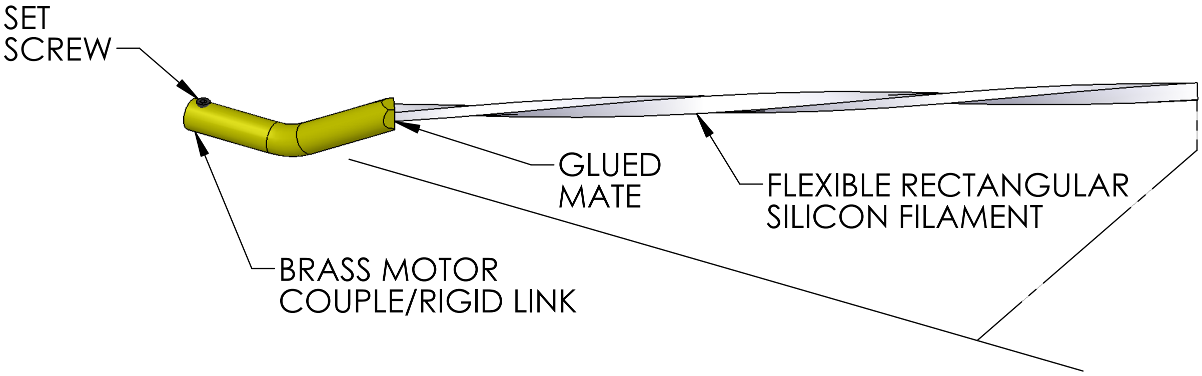

Figure 5.4: Flexible, rectangular cross-section tail assembly (Flex Tail: Rec)

The flexible, cylindrical cross-section and flexible, rectangular cross-section tails are very similar. Both tails have moulded silicone filaments glued to a brass rigid link. The rigid link contains the required geometry to mount to the gearhead. Like the rigid tail, the two are fastened together using a set screw. The cylindrical filament is 2.38 [*mm*] (3/32 [*in*]) in diameter. The rectangular filament is 2.5 [*mm*] wide and 1.25 [*mm*] tall: a direct 20 times scaling of the dimensions decided upon in Section 3.6.2. The rectangular filament twists 0.857 turns along its length of 118 [*mm*]. The cylindrical filament is also 118 [*mm*] long. The cylindrical tail and rectangular tail assemblies are shown in Figures 5.3 and 5.4 respectively.

The material used for the filaments is Dow Corning® 3112 silicone RTV rubber. The material is a combination of two liquid rubbers that solidify when combined. Its main advantages for this application are that it cures at room temperature, is easily poured into moulds, and releases well. The rubber has a Shore A durometer hardness of 60 and an approximate elastic modulus of 2.6 [*MPa*] [57]. For more information see Appendix B. It is speculated that this material stiffness will allow for the filament to conform easily under the drag loads. The actual performance of the material is discussed in Section 5.4.

Both the rectangular and cylindrical filaments have a constant cross-section. This was chosen because it is easier to manufacture. It was also chosen because not enough information was available to design a tapered filament as discussed in Sections 3.6.2 and 4.2.3. The disadvantage of the constant cross-section is that the filament will not exhibit the two-stage stiffness profile proposed in the initial design and implemented in the flexible filament ADAMS model. The assumption, especially regarding the rectangular filament, is that the constant stiffness of the filament can be balanced with a specific rotational velocity to form a complete helix. However, the evidence toward the need for a taper may invalidate this assumption.

5.2.3 Force Measurement

At this point, the apparatus around the motor and filament must be considered. As mentioned, the test bench emulates a situation where the swimming velocity and rotational velocity of the body are equal to 0. Accordingly, the test bench must hold the motor securely while allowing for the propulsive force and required driving torque to be measured.

There is considerable challenge in doing so. First, the eccentricity of the proposed system induces torsional loads onto whatever is holding the motor. These loads must be eliminated as to not interfere with the measurement of the propulsive force. Second, earlier it was shown that the expected maximum driving torque is only 0.30 [*mNm*]. A similar analysis of the propulsive

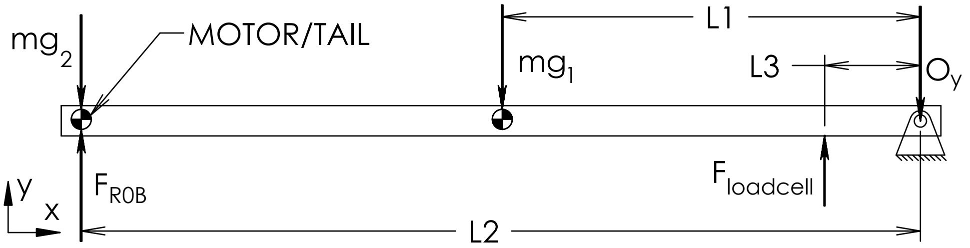

Figure 5.5: FBD of Test Bench Configuration

force, using Figure 4.33 and the force scaling factor derived in Equation (5.7), estimates that the propulsive force to be measured by the test bench is roughly 50 [*mN*]. This value is extremely small and difficult to measure accurately. Furthermore, any external influences on the system such as friction could severely alter the results.

With regards to measuring the propulsive force, to account for the aforementioned challenges, the test bench utilizes a pivoting, cantilever beam. The motor/tail is mounted at the far end of the beam. The beam itself rests on a Honeywell, Model 13, 25 lbs load cell (order code: AL322BL, Appendix B) situated close to the pivot.

In this configuration, assuming negligible deflection at the load cell[1], the test bench is essentially static. The cantilever beam is heavy and stiff enough, relative to the maximum propulsive force of the tail, that the tail does not have the ability to lift or bend the beam from its resting position. Therefore, dynamic loads can be neglected when analyzing the forces of the test bench.

Figure 5.5 shows a free body diagram of the test bench. From the free body diagram the sum of the moments about the origin (pt. O) and the sum of the forces in the y-direction can be taken:

$$+ \circlearrowleft \quad \Sigma M_O = 0 = mg_1(L1) + mg_2(L2) - F_{R0B}(L2) - F_{loadcell}(L3) - \mu_s O_y R_p, \tag{5.9}$$

$$+\uparrow \quad \Sigma F_y = 0 = F_{R0} + F_{loadcell} - mg_1 - mg_2 - O_y, \tag{5.10}$$

where F_{R0B} is the propulsive force of the tail, $F_{loadcell}$ is the measured force at the load cell, mg_1 is the constant weight of the beam, and mg_2 is the constant, combined weight of the motor, tail, and mounting apparatus. The friction term ($\mu_s O_y R_p$) in Equation (5.9) is based on a simple Coulomb model for friction where R_p is the radius of the pivot joint. The static coefficient of friction (μ_s) is used since, as mentioned, the system is essentially static. Combining equations (5.9) and (5.10) gives:

$$0 = mg_1(L1 - \mu_s R_p) + mg_2(L2 + \mu_s R_p) - F_{R0B}(L2 - \mu_s R_p) - F_{loadcell}(L3 - \mu_s R_p). \tag{5.11}$$

---

[1] Max load cell deflection = 0.0004 [*in*], Appendix B.

There are two points of interest when considering propulsive force measurement. The first is when the system is at rest and F_{R0} is equal to zero. The second is when the motor is on and the tail is generating a steady-state propulsive force. The weights of the different components remain constant for both of these points of interest. By evaluating Equation (5.11) at the two points of interest a relationship between the changing propulsive force and the observed change in force measured at the load cell can be established:

$$\Delta F_{loadcell} = \Delta F_{R0B} \frac{L2 - \mu_s R_p}{L3 - \mu_s R_p}. \tag{5.12}$$

Equation 5.12 shows that the cantilever beam configuration amplifies, with respect to the load cell measurement, any change in propulsive force by a factor of $(L2 - \mu_s R_p)/(L3 - \mu_s R_p)$. This amplification factor is one of the main advantages of the cantilever beam configuration. It will decrease the difficulty in measuring the propulsive force simply because the values are larger. The other main advantage is that, if μ_s is assumed constant at both points of interest, friction in the system does not change with the propulsive force. Therefore, friction is simply a scalar that is accounted for when the system is characterized (Section 5.4).

The torsional loads are accounted for in the cantilever beam configuration by choosing a beam with adequate torsional stiffness. The beam used is a 19.05 $[mm]$ (0.75 $[in]$) square tube with 1.78 $[mm]$ (0.07 $[in]$) thick walls. It is assumed that this beam will be stiff enough that the beam twist will be negligible; however, confirmation of this hypothesis must be explored during the experiments (Section 5.4).

With the beam cross section set, the various lengths can be set to ensure that the force at the load cell does not exceed its maximum load capacity of 111 $[N]$ (25 $[lbs]$). The cantilever beam is 698.5 $[mm]$ (27.5 $[in]$) long and made from Aluminum 6061-T6 ($\rho = 2710$ $[kg/m3]$) Accordingly, mg_1 is approximately 2.26 $[N]$. The mass of the motor, tail, and housing (described below) is approximately 25 $[g]$ meaning that $mg_2 \approx 0.25$ $[N]$. The pivot is set in from the beam end by 9.5 $[mm]$ (3/8 $[in]$). Likewise, the motor/tail is also set in from the beam end by 9.5 $[mm]$ (3/8 $[in]$). Therefore, $L2$ is approximately 679.5 $[mm]$ (26.75 $[in]$) and $L1$ is approximately 339.7 $[mm]$ (13.38 $[in]$). The load cell placement is arbitrary and is initially set at $L3 = 20$ $[mm]$. Figure 5.6 shows the general layout for this configuration.

The pivot for the beam is a smooth, polished steel shaft, press fit into the beam, running on two bushings (Fig. 5.6). The bushings are iglide® J, JFI-0405-04, Linear Plain Bearings (Appendix B). Each bushing is press fit into a piece of aluminum angle on each side of the cantilever beam. The pieces of angle are fixed. The bearings have a coefficient of friction (μ_s) of 0.04 when used with oil, as they are (Appendix B). The shaft is 6.35 $[mm]$ (1/4 $[in]$) in diameter therefore $R_p = 3.175$ $[mm]$ ($1/8$ $[in]$). This means that the length modifier $\mu_s R_p$ present in equations (5.11) and (5.12) is equal to 0.13 $[mm]$. This value is small enough that the length modifier, given the values for $L1, L2,$ and $L3$, will have little effect when estimating the force at the load cell. Accordingly, from Equation (5.11), with $\mu_s R_p$ and F_{RO} set to 0, the force measured by the load cell is:

$$\begin{aligned} F_{loadcell} &\approx \frac{mg_1(L1) + mg_2(L2)}{L3}, \\ &\approx 46.9\ [N]. \end{aligned} \tag{5.13}$$

This is less than the maximum load capacity of the load cell as desired. It should also be noted that, using the values given for $L2$ and $L3$, the cantilever beam will amplify the propulsive force by a factor of almost 36.

The motor/tail package is not mounted directly to the cantilever beam. Instead, it is held in a housing as shown in Figure 5.6. This was done because the motor has few mounting features. The housing is essentially a sleeve, made of aluminum, with a shoulder on it. The motor is fixed to the housing simply by sliding it into place and tightening a set-screw. The housing is attached to the beam by passing through both a spring and a hole in the beam. The spring is contained by the housing shoulder and the beam. The spring is compressed and an aluminum collar is fixed to the housing using a set screw. The forces exerted by the tail are small enough that this configuration holds the motor firmly in place under friction alone.

There are two disadvantages to this cantilever beam configuration. The first is that the system is under-damped. Excitation from the tail will cause the beam to oscillate and slowly settle to the equilibrium position. To speed up the settling time a damper was added to the beam. As seen in Figure 5.6, the damper is simply a large aluminum plate suspended in the oil. The second disadvantage is that any vibrations experienced by the fixed pieces of aluminum angle are amplified at the end of the cantilever beam. To isolate the system, the test bench, minus the fluid reservoir, is mounted on a heavy graphite slab. In turn, the graphite slab, rests on rubber mounts. The combination of a large mass and flexible mounting ensure that negligible vibrations pass through the test bench.

5.2.4 Wall Effects

The oil container is an essentially cylindrical 8 $[l]$ Nalgene bottle procured at the research facility[2]. The top of the bottle has been cut off to increase the opening size. The bottle, as cut, has a

---

[2] Chemistry Stores (ESC 109)

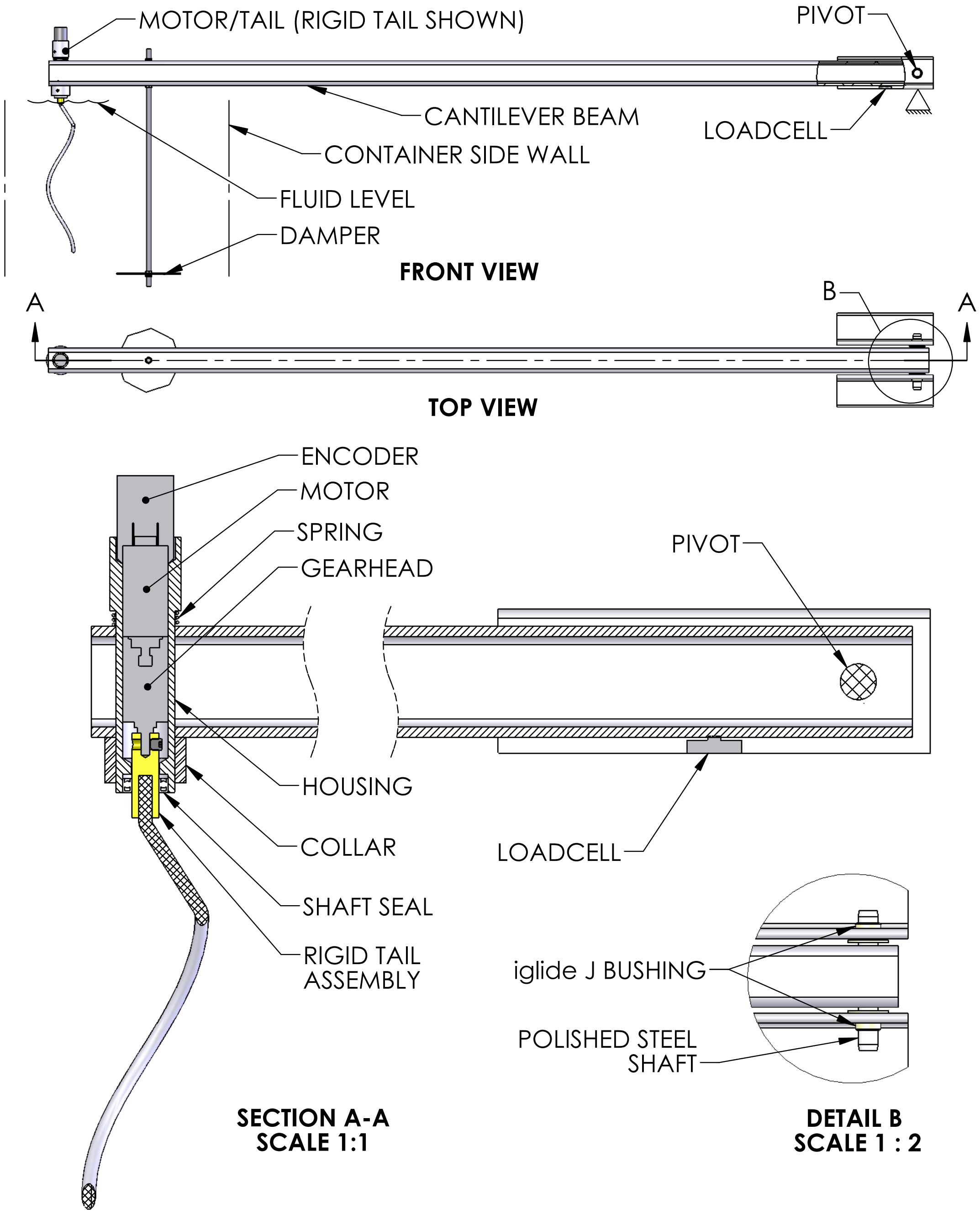

Figure 5.6: Test Bench Proposed Layout

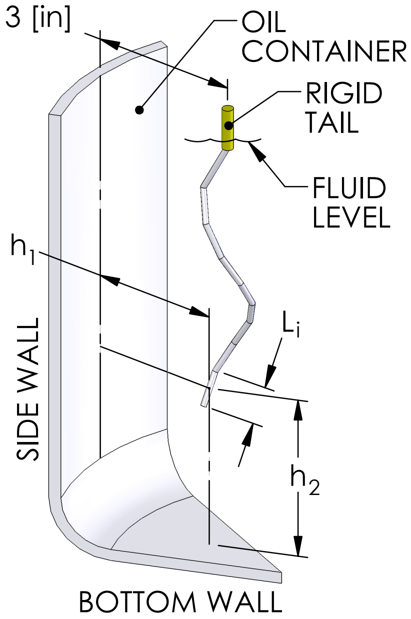

Figure 5.7: Slender cylinder with relation to fluid container walls (Not To Scale)

diameter of 7.5 [*in*] (190.5 [*mm*]) and a height of 12.5 [*in*] (317.5 [*mm*]). The container is filled with oil up to the lip.

This size of bottle was used so that the walls are a sufficient distance from the tail. In low Reynolds number flow the dominate nature of viscous forces means that drag is affected by the presence of walls far from the mover. Therefore, if the tail is to close to the fluid container walls, the tail will not adequately simulate the system considered in the analytical and ADAMS models.

Brennen and Winet provide a summary of the effects of walls on slender cylinders moving through a fluid [25]. According to their work, given the layout in Figure 5.7, the drag coefficients for a moving cylinder, influenced by the walls, are:

With respect to the side wall:

$$\text{For motion along the cylinder :}\quad K_{s:sw} = \frac{2\pi\mu}{\ln(L_i/a) - \frac{3}{2} + \ln(2) - \frac{3L_i}{16h_1}},$$

$$\text{For motion across the cylinder :}\quad K_{n:bw} = \frac{4\pi\mu}{\ln(L_i/a) - \frac{1}{2} + \ln(2) - \frac{3L_i}{4h_1}},$$

With respect to the bottom wall:

$$\begin{aligned} \text{For motion along the cylinder :} \quad K_{s:bw} &= \frac{2\pi\mu}{\ln(L_i/a) - \frac{3}{2} + \ln(2) - \frac{3L_i}{8h_2}}, \\ \text{For motion across the cylinder :} \quad K_{n:bw} &= \frac{4\pi\mu}{\ln(L_i/a) - \frac{1}{2} + \ln(2) - \frac{3L_i}{8h_2}}. \end{aligned}$$

Recall that Cox claims that the drag coefficients for the cylinder, in the absence of walls, are [54]:

$$\begin{aligned} K_s &= \frac{2\pi\mu}{\ln(L_i/a) - \frac{3}{2} + \ln(2)}, \\ K_n &= \frac{4\pi\mu}{\ln(L_i/a) - \frac{1}{2} + \ln(2)}. \end{aligned} \tag{4.56}$$

If the oil container is large enough, there will be negligible difference between the Brennen and Winet coefficients and the Cox coefficients. A rough analysis can be performed to show that this is likely the case. First, the unknown variables for the equations, namely h_1, and h_2, must be set. Since the drag coefficients given are for straight, slender cylinders, assume that the helix section of the rigid tail is discretized into 8 sections as was done to create the ADAMS model (Section 4.2). The axis of rotation of the tail is 76.2 [*mm*] (3 [*in*]) from the container side wall. This configuration can be seen in Figure 5.7. At 20 times scale, the tail helix has an amplitude of 20 [*mm*] and a total length, including the rigid link, of 120 [*mm*]. The individual links are such that:

$$L_i = 14.76 \text{ [}mm\text{]}.$$

The last section of the tail is the one of interest as it comes as close to both the bottom and side walls of the container as any of the other links. The analysis is performed under the assumption that the link, as shown in Figure 5.7, is as close to both the walls as it will ever get. All other links are subjected to lesser wall effects. The centroid of the last link is approximately 113 [*mm*] below the fluid level. Given the position of the tail within the oil container:

$$\begin{aligned} h_1 &= 66.2 \text{ [}mm\text{]}, \\ h_2 &= 204.5 \text{ [}mm\text{]}. \end{aligned}$$

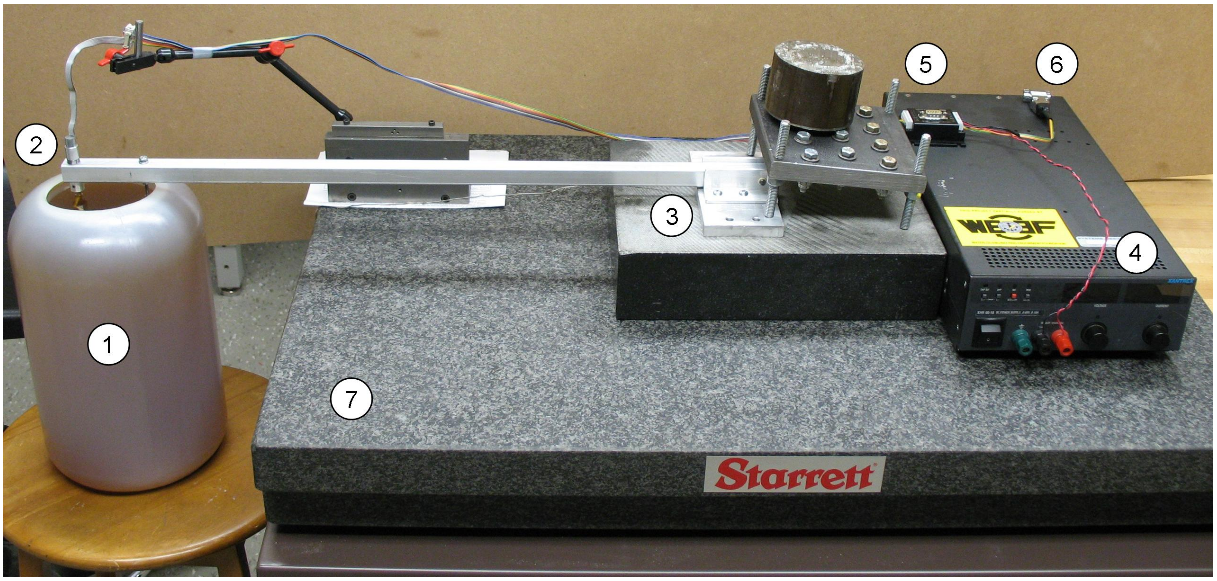

Figure 5.8: Test Bench Layout: 1) Oil Container, 2) Motor and Tail, 3) Load Cell/Beam Pivot, 4) Power Supply, 5) Motor Controller, 6) PC Communications, 7) Granite Table

Therefore, the difference between the Brennen/Winet and Cox coefficients are:

With respect to the side wall:

$$\left(\frac{K_{s:sw}}{K_s} - 1\right) \times 100\% = 2.64\%,$$

$$\left(\frac{K_{n:sw}}{K_n} - 1\right) \times 100\% = 6.90\%,$$

With respect to the bottom wall:

$$\left(\frac{K_{s:bw}}{K_s} - 1\right) \times 100\% = 0.90\%,$$

$$\left(\frac{K_{n:bw}}{K_n} - 1\right) \times 100\% = 1.06\%.$$

It is assumed that these values are low enough that the wall effect on the tail is minimal and will not severely influence the propulsive force of the tail.

5.2.5 Motor Control

Rotational speed control is essential for the test bench to work properly. The test bench must allow for the propulsive force to be measured at a known constant speed. To accomplish precise speed control, a controller was purchased from MicroMo. It is a series MCDC 2805 controller designed to interface with both the motor and a PC. Communication with the PC is accomplished via the RS-232 (serial) port and a proprietary software program: FAULHABER Motion Manager Version 3.3[3]. For the test bench, velocity control is accomplished using the default proportional/integral controller. The controller module is powered by a 24 $[VDC]$ supply. For more information on the controller please see Appendix B.

The required driving torque is measured by analyzing the current passing through the motor at a known speed. To accomplish this, a small resistor, of known resistance (R), is placed in series with the motor. When the motor is on, the voltage drop across the resistor (V $[VDC]$) is measured using an oscilloscope. The well known relationship $I = R/V$ is then used to calculate the current passing through the motor. Once the current is known, it can be multiplied by the torque constant of the motor (k_M) and the motor efficiency (η_m) to give the torque output at the motor shaft. In turn, the torque output of the motor can be multiplied by the gear ratio (G_r) and the gearhead efficiency (η_g) to calculate the torque at the output shaft. Together, this chain is represented as:

$$M_{net} = M_G + M_{R0B} = V\left(\frac{1}{R}\right)k_M\eta_m G_r\eta_g \ [N/m], \tag{5.14}$$

where M_G is the torque required to drive the motor without a tail and M_{ROB} is the torque required to drive only the tail. For the motor/gearhead chosen, $k_M = 3.35$ $[mNm/A]$, $G_r = 64$, $\eta_m = 0.51$, and $\eta_g = 0.7$ (Appendix B). The resistor chosen has a value of $R = 1.118\Omega$. This value is roughly 2% of the motor terminal resistance and, as such, is expected to have little effect on the measurements.

5.3 Experimental Procedures

This section outlines the procedures followed to gather the experimental results presented in Section 5.4.

5.3.1 Cantilever Beam Characterization

To measure the propulsive force of the tail, the cantilever beam must first be characterized so that any changes in force observed by the load cell can be accurately represented as changes in the

---

[3] Available for download at micromo.com

propulsive force exerted by the tail. There are at least two possible methods to achieve characterization. The first is to accurately measure all variables and model the beam accordingly. The second method is to characterize the beam through experimental procedure. For this work the second method was chosen because 1) it is quicker, and 2) it is less susceptible to error since a direct relationship between load at the motor and load seen by the load cell can be established without the need to measure relevant distances and weights. This is especially valuable because the test bench apparatus was not precision manufactured and the precise, actual distances between, for example, the pivot point and the centre of mass, are difficult to establish.

To characterize the beam the following procedure is followed:

1. Remove the motor/tail/housing from the cantilever beam.
2. Unload the load cell.
3. Under zero-load conditions, calibrate the load cell.
4. Lower the cantilever beam onto the load cell.
5. Select a known mass.
6. Begin collecting load cell data.
7. Load the beam with a known mass such that the load is coincident with the axis of rotation of the tail. To accomplish this, a conical basket, of known mass, is constructed. The additional mass is contained within the basket and the basket is lowered into the motor housing mounting hole (Fig. 5.9).
8. Unload the beam.
9. Repeat steps 7 and 8 multiple times (8–15).
10. Stop sampling data and save results.
11. Repeat steps 6–10 with several different (5–8) known masses to sufficiently characterize the beam.

The result of the proceeding procedure is a data file for each known mass. Each file contains two columns of data: time and measured force. Figure 5.10 shows a typical graph of one of these files. As can be seen, the force jumps between the unloaded condition to the loaded condition. In post-processing, the leading and trailing edges of each step are tracked and the force data between each edge is averaged. In this way, the graph shown in Figure 5.10 provides 24 data points: 12 unloaded points at 0 [g], and 12 loaded points at known mass (m [g]).

For the test bench, the beam was characterized using 7 different known masses. Post-processing the raw data files from these 7 weights produced 160 data points. Table 5.2 provides a breakdown of the different masses used and the data points each provided.

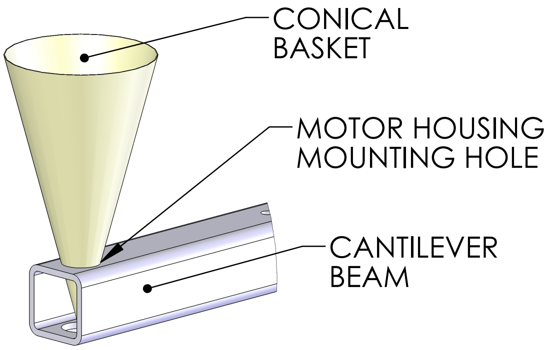

Figure 5.9: Conical basket lowered into the motor housing mounting hole

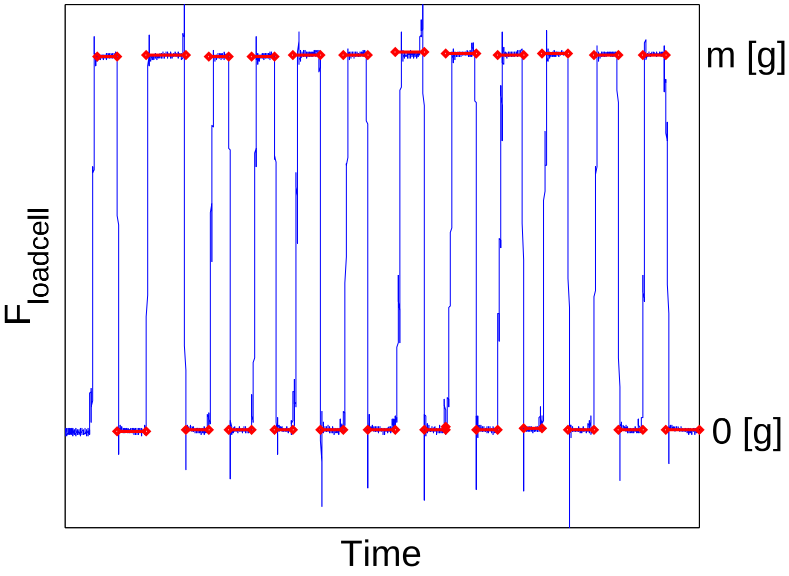

Figure 5.10: Cantilever beam characterization raw data (typical)

Mass (m) [g]	**Data Points**
0	80
23.86	9
24.90	13
25.94	10
28.03	12
34.89	12
36.26	12
43.22	12

Table 5.2: Results of beam characterization post-processing

The data points, after the mass values are converted to weights, are condensed into one graph that can be used to characterize the beam (Fig. 5.11). The results are linear, which is expected. Least squares linear approximation of the data provides a characteristic equation for the beam. It is:

$$F_{net} = mg_1 - F_{R0B} = 0.0347(F_{loadcell}) - 1.22, \tag{5.15}$$

with the maximum difference between actual and fitted data points being 0.93% and the average difference being 0.25%. Therefore, given Equation (5.15), any measured force present at the beam tip can be calculated by measuring the reaction force at the load cell.

5.3.2 Propulsive Force Measurement Procedure

Measuring the propulsive force requires the comparison of F_{net} when $F_{R0B} = 0$ and when $F_{R0B} \neq 0$. In this way, mg_1 can be eliminated thus leaving only the propulsive force F_{R0B}. To accomplish this, the following procedure is used.

1. Choose a tail configuration and mount it to the motor.
2. Fasten the motor and motor housing to the cantilever beam as described in Section 5.2.
3. If not already calibrated, unload the load cell and calibrate.
4. Begin sampling data.
5. After roughly 5 seconds, turn motor on to desired speed.
6. After roughly 5 seconds, turn motor back to 0 speed condition.
7. After roughly 5 seconds, stop sampling data, save the results, and record the rotational speed of the motor.

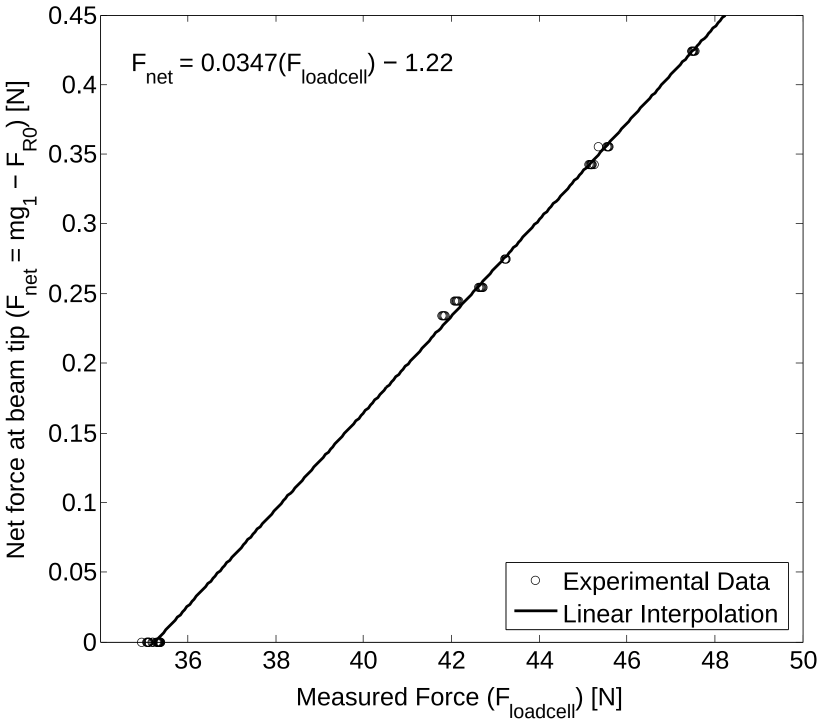

Figure 5.11: Net force at beam tip versus measured force at load cell.

8. Repeat steps 4–7, 5–15 times. The number of times depends on the variability of the data being collected.
9. Choose another desired speed and repeat steps 4–8. Repeat this step for as many different speeds as required to adequately capture the desired speed range.
10. Choose another tail configuration and repeat the entire procedure until all configurations are tested.

This procedure requires p different tails to be tested. For each tail, q speeds are tested. And for each speed, r measurements are taken. The result is a set of data files, one file for each measurement, showing the measured load cell force versus time. Also, each data file has a corresponding rotation velocity (ω_{motor}) associated with it. Figure 5.12 shows a graph of a typical data file procured during the propulsive force measurement procedure. To calculate the propulsive force of the tail and modify it for scale, the following series of post-processing steps are taken.

The first post-processing operation to the raw data is to take a 100 point moving average. This removes much of the noise and allows for the true behaviour of the system to be seen. As Figure 5.12 shows, it is obvious that the motor is initially off (‘motor off’ condition), turned on (‘motor on’ condition), and turned off again.

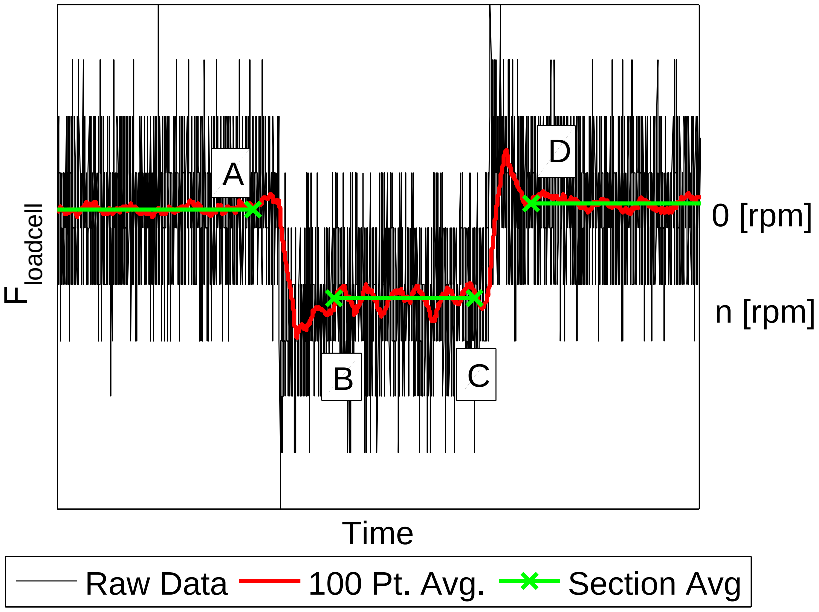

Figure 5.12: Propulsive force measurement procedure raw data (typical)

The second post-processing step requires the user to pick four x-axis coordinates. By picking these coordinates, the post-processing algorithm is told which sections of data pertain to transient behaviour. This data is ignored: only steady-state behaviour is of importance. The points to be picked are:

A The end of the first 'motor off' stage.
B The end of transient behaviour at the beginning of the 'motor on' stage.
C The end of the 'motor on' stage
D The end of the transient behaviour at the beginning of the second 'motor off' stage.

The third step is to average the raw data between the first data point and point A, between points B and C, and between point D and the last data point. This provides three values. Two give the average, steady-state, load cell force during the 'motor off' condition. In other words, this is the average, steady-state, load cell force as influenced only by the weight of the motor/tail assembly (i.e. $F_{loadcell}$ when $F_{R0B} = 0$ @ $\omega_{motor} = 0\ [rpm]$). The other value gives the average, steady-state, load cell force during the 'motor on' condition (i.e. $F_{loadcell}$ when $F_{R0B} \neq 0$ @ $\omega_{motor} = n\ [rpm]$.

The forth step is to transform the average load cell force values into propulsive force values using Equation (5.15). The result is three average net force values: two pertaining to the 'motor off' condition and one pertaining to the 'motor off' condition.

The fifth step is to calculate only the propulsive force (F_{R0B}). It is the difference between the average net force during the 'motor off' condition and the average net force during the 'motor on' condition. Accordingly, the two 'motor off' values are averaged together and the 'motor on' condition is subtracted from the results.

Before the test bench propulsive force results can be accurately compared to the analytical and ADAMS models, the rotational speed must also be transformed. For each data file, the rotational speed of the motor at large scale ($\omega_{motor} = n\ [rpm]$) is recorded. It is required to have the rotational speed of the tail at the small scale ($\omega_A\ [rad/s]$). The transformation is completed by incorporating Equation (5.6), the gear ratio (G_r), and various unit transformations. The result is:

$$\omega_A\ [rad/s] = \omega_{motor}\left(\frac{1}{60}\right)\left(\frac{1}{G_r}\right)\left(\frac{1}{0.853}\right)2\pi. \tag{5.16}$$

The final post-processing operation is to scale the values. The average propulsive force value (F_{R0B}) is scaled by applying the force scaling factor derived in Equation (5.7). The rotation speed value (ω_B) is scaled using the scaling factor derived in Equation (5.6). These two operations gives the propulsive force of a tail 20 times smaller (F_{R0A}) running at an equivalent rotation speed (ω_a): these values are directly comparable to the analytical and ADAMS models. The results of the propulsive force measurement procedure, as compared to the analytical and ADAMS models, are given in Section 5.4.

5.3.3 Required Driving Torque Measurement Procedure

Measurement of the required drive torque for the tail is accomplished by analyzing the voltage drop across a resistor in series with the motor. From the voltage, first the current, then the motor torque, and finally the gearhead torque may be calculated. To gather the required data to perform these calculations the following procedure is followed:

1 Choose a tail configuration and mount it to the motor.
2 Fasten the motor and motor housing to the cantilever beam as described in Section 5.2.
3 Turn motor on and, using input voltage, adjust speed until it is close to the desired speed. It is assumed that the input voltage is constant while the measurements are taken.
4 Measure nominal voltage drop across the resistor (V) using an oscilloscope. Adjust the level on the oscilloscope to correspond with nominal voltage: record the results. A screen capture of a typical oscilloscope screen, with nominal voltage displayed, is given in Figure 5.13. The spikes in the screen capture are attributed to the fact that a switching power supply is used. However, the affect the nominal voltage minimally.

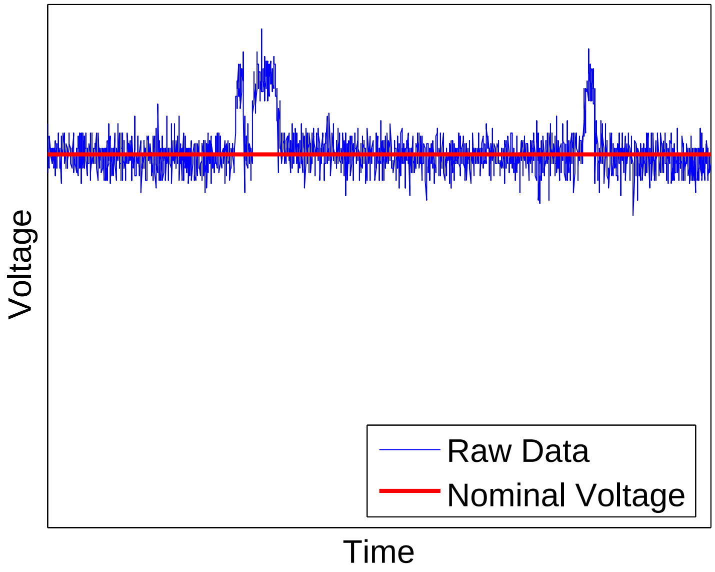

Figure 5.13: Typical oscilloscope output: voltage versus time

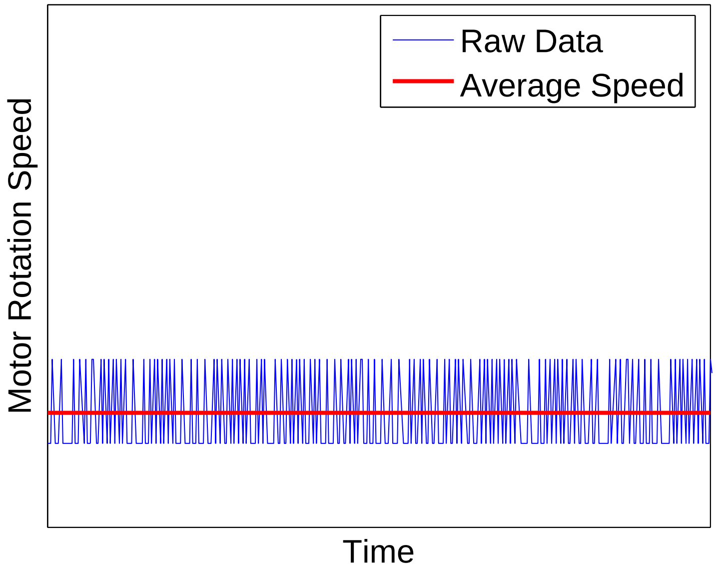

Figure 5.14: Motor rotational speed versus time (typical)

5 Record actual speed (ω_{motor} $[rpm]$). For the test bench setup used this entails taking saving a data snapshot of the actual speed as measured by the Faulhauber Motion Manager software. The noise seen in the snapshot is attributed to the limited resolution of the software when reporting actual motor rotational velocity.

6 Adjust motor speed to zero and then readjust back to desired speed. Repeat steps 4–5. Repeat this step 5-10 times depending on variability of results.

7 Choose another desired speed and repeat steps 3–6. Repeat this step until all desired speeds are tested.

8 Choose another tail configuration and repeat the entire procedure until all tail configurations are tested. Then repeat the procedure with no tail attached to capture data pertaining to the no-tail condition.

Similar to the propulsive force procedure, this procedure requires p tails to be tested plus the no-tail condition. For each of the $p + 1$ configurations, q_p speeds are tested. For each speed, r_p measurements are recorded. The result is one data file containing motor rotational speed data for each measurement and a corresponding nominal voltage. A graph of a typical data file for rotational speed is shown in Figure 5.14. Post-processing steps are required to convert the voltage (V) into a driving torque (M_{R0B}), calculate the rotational speed of the tail (ω_B), and modify both values for scale.

With regards to the nominal voltage conversion, applying Equation (5.14) to the recorded nominal voltage will result in M_{net}: the torque required to drive the tail and overcome the losses of the motor. It is desired to have only the required driving torque for the tail (M_{R0B}). To do this, the results from the no-tail configuration are subtracted from the other configurations. Then by applying the scaling factor for torque, as given in Equation (5.8), M_{R0A} is calculated from M_{R0B}.

To determine the large scale rotational speed of the tail (ω_b), the data files gathered are processed by averaging the data to give the average motor rotation speed. Equation (5.16) is then applied to determine the small scale rotational speed of the tail (ω_A).

The results of driving torque measurement procedure, as compared to the analytical and ADAMS models, are given in Section 5.4.

5.4 Results and Discussion

The force measurement procedure, as outlined in Section 5.3.2, was carried out with each of the three tails (Rigid Tail, Flex Tail: Cyl, Flex Tail: Rec). The rigid tail was tested at 8 different speeds and a total of 46 data points were procured from post-processing. The flexible, cylindrical

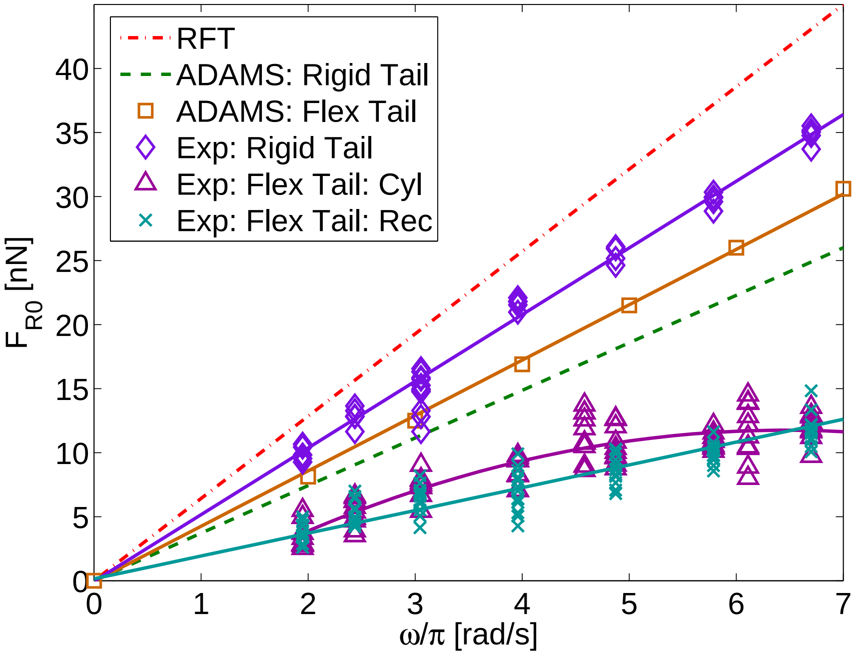

Figure 5.15: Propulsive Force (0 DOF)

cross-section tail was tested at 9 different speeds for 88 data points. The flexible, rectangular cross-section tail was tested at 7 different speeds for a total of 101 data points. The difference in data points and speed is a result of observed variability in the measurements while the data was being procured. In other words, as the experiment was carried out, if the tester felt that the data was scattered, more data points were taken. The results of the force measurement procedure, including application of the scaling factors, are given in Figure 5.15. It should be noted that the test was not run until the fluid was calm.

Comparing the experimental results to the models tested previously yields interesting results. For the experimental rigid tail, the propulsive force (F_{R0}) is approximately 40% greater than the ADAMS rigid tail and 20% less than the resistive-force theory (RFT) model[4]. These values are significant enough that neither model can be considered accurate as is. The differences between these the models can and the experimental results are attributed to a combination of experimental error and modelling error.

On the experimental side, factors that contribute error begin with the manufacturing impre-

---

[4] body is fixed (0 DOF) for both models

cision associated with the rigid tail. Namely, the small difference between the actual helix shape (λ and a) and the desired helix shape. This may be significant because of evidence that shows that the propulsive force is sensitive to the helix shape. Consider Section 4.2.3 where the ability of the flexible filament to form a complete helix is explored. In the 0 DOF case the average discrepancy between the desired joint deflection angle (ϕ) and the desired angle is 10%. For the 2 DOF case the discrepancy is 4% and for the 6 DOF case it is 5.4%. Yet the difference between the propulsive force of the flexible tail and its rigid counterpart for each case is 14.5% greater, 0.52% less, and 14.2% greater respectively. It can be seen that the propulsive force of the tail is very dependent on the position of the tail and that slight differences can be magnified.

Further error associated with manufacturing imprecision is an eccentric axis of rotation observed on the experimental tail; the rigid link is not perfectly concentric with the motor shaft due to manufacturing imprecision. Error is also added to the comparison by small differences between the actual fluid parameters (ρ_B and μ_B) and the values, as taken from the product literature (Appendix B), used in Section 5.2.1 to calculate the scaling factors. There is also error added during the beam characterization procedure. While these instances of error are assumed to be small, their cumulation could be significant.

Another source of error on the experimental side is measurement error. As mentioned, the force measured by the load cell contains significant noise that must be filtered before meaningful data can be interpolated. This noise can be seen in Figure 5.3.2. The result of this noise is variability, as seen in Figure 5.15, in the data procured during the experimental procedure for propulsive force measurement. The data pertaining to the rigid tail and the flexible, rectangular cross-section tail is fit with a linear curve (Appendix B for details). The average difference between the actual data and the data predicted by the curve fit for the rigid tail is 4.74%. The average difference for the flexible, rectangular cross-section tail is 13.57%. The flexible, cylindrical cross-section tail is fit with a parabolic curve (Appendix B). The average difference between the two sets of data for this tail is 13.34%. These numbers are significant and must be considered when discussing error in the system. For future work, reduction of the measurement error could be accomplished by reducing signal noise and by taking more measurments during the experimental procedure to increase the accuracy of the linear curve fit.

With regards to the RFT model, there is evidence that, as is the case here, the propulsive force of a helical filament is consistently over-predicted due to error in the model. Recall that Behkam *et. al.* at Carnegie Mellon University have compared the RFT model to their experimental results with different rigid helix configurations [22–24]. Despite the fact that there are questions surrounding their results (Chapter 2), one of their most consistent observations is an over-prediction of propulsive force by the RFT model. This is positive for the results given here and provides evidence that, while experimental error is certainly present, the experimental results ‘fall where they should’ if you will.

An interesting aside regarding the experimental results pertains to the Lighthill model. As mentioned, the experimental results for the rigid tail (0 DOF) fall in between the RFT model and the ADAMS model. Looking back to Figure 4.23 it can be seen that the Lighthill model predicts a propulsive force, under 2 DOF conditions, in between the RFT and ADAMS model. On the surface this seems insignificant until one examines the results for driving torque under 0 DOF conditions (Figure 4.24) and the results for driving torque under 2 DOF conditions (Figure 4.20. It can be seen that the relative position of the results is consistent for both graphs. Consequently, it can be conjectured that this trend would also be true for the results pertaining to propulsive force. In other words, under 0 DOF conditions, assuming the relative position of the data remains consistent from the 2 DOF condition, the Lighthill results for propulsive force should fall in between the RFT and ADAMS model. This would place the Lighthill results closer to experimental results than the other two models. Accordingly, there is admittedly slim evidence that the Lighthill model is the most accurate of the three. This hypothesis could be examined further if a test bench simulating the 2 DOF condition was built.

Returning to the ADAMS model, even with the aforementioned experimental error, likely the largest contributer to the 40% discrepancy between the ADAMS model and the experimental results is modelling error. As mentioned in Section 4.2.3, the accuracy of the Cox drag coefficients increases as the slenderness ratio increases. The links used in the ADAMS model have a relatively low slenderness ratio of 12.3, which are likely translating into inaccurate drag coefficients.

Unfortunately, the slenderness ratio of the ADAMS links cannot be increased without causing other difficulties. Increasing the slenderness ratio requires the link length to be increased. This ultimately decreases the total number of links, which, in turn, decreases the ability of the ADAMS model to properly replicate the shape of a helix. It is not recommended that the number of links be less than the eight.

One positive aspect of the discrepancy between the experimental rigid tail and the ADAMS counterpart is the consistency of the error across the entire speed range. Therefore, without addressing the experimental error, it may be possible to account for the inaccuracy of the drag coefficients by simply applying a scaling factor, based on slenderness ratio, to the drag coefficients. Another solution to account for the inaccuracy in the drag coefficients is to use a completely different drag model. An advantage of this approach is that, if the new drag model is not based on the slenderness ratio, the number of links (N) could be increased to more accurately represent a continuous filament. Either way, if these solutions are explored in the future, the author has confidence that the lumped parameter ADAMS model can be tuned to accurately (±10%) simulate the experimental setup.

For the flexible, rectangular cross section tail, the experimental results are compared to the ADAMS model flexible tail with the head fixed (0 DOF, Flex Tail). Unlike the rigid configuration, where the ADAMS model predicted less propulsive force, the flexible configuration ADAMS model predicts a propulsive force approximately 57% more than the experimental measurements. While this large discrepancy is, in part, likely caused by the aforementioned experimental and modelling errors, the larger issue is the difference in the shape of the two filaments.

Figures 5.16 – 5.18 overlays results from the flexible filament ADAMS model onto high-speed video of the experimental, flexible, rectangular cross-section filament. It can be seen that the two filaments trace very different paths. An observation to note is that the experimental tail is rotating slightly faster than the ADAMS model. This accounts for the misalignment seen between the two in later frames. The desired rotation rate (ω) for both systems is 1.56 [rev/s].

Recall that the ADAMS model filament is implemented with a two-stage elastic stiffness response to joint deflection that varies from joint to joint. On the other hand, the filament has constant stiffness down its length. It was hoped that an optimal rotational speed would be found that caused the filament to form a complete helix that would trace the same path as the ADAMS model. This is not the case. In fact, the overall steady-state shape of the experimental filament, from qualitative observations, was very similar for all speeds tested. Support of this is seen in the linear response of the tail with regards to propulsive force (Fig. 5.15): a changing filament shape would cause a non-linear response. This implies that the operating margin for a constant stiffness filament may be larger than initially expected (Section 3.6.1).

The reasons for the shape discrepancies are likely three-fold. First, consider the section of the experimental filament closest to the rigid link particular at 1/4 turn captures (i.e. 2.25 rev, 2.75 rev, etc.). It can be seen that the experimental filament is under-rotating even at the rigid link. Therefore, it is believed that the experimental filament is too stiff. The second reason is the lack of a taper in the filament. The evidence of this is the increase in the curvature as one moves down the length of the filament. It is hard to see in two-dimensional space; however, the curvature increase is evident at the free end of the filament where the filament is essentially straight.

As the ADAMS model showed in Section 4.2.3, an ideal flexible filament has the ability to generate propulsive forces equal to a rigid filament. It is speculated that by eliminating these two issues the flexible filament will perform closer to the ideal state. Therefore, it is recommended

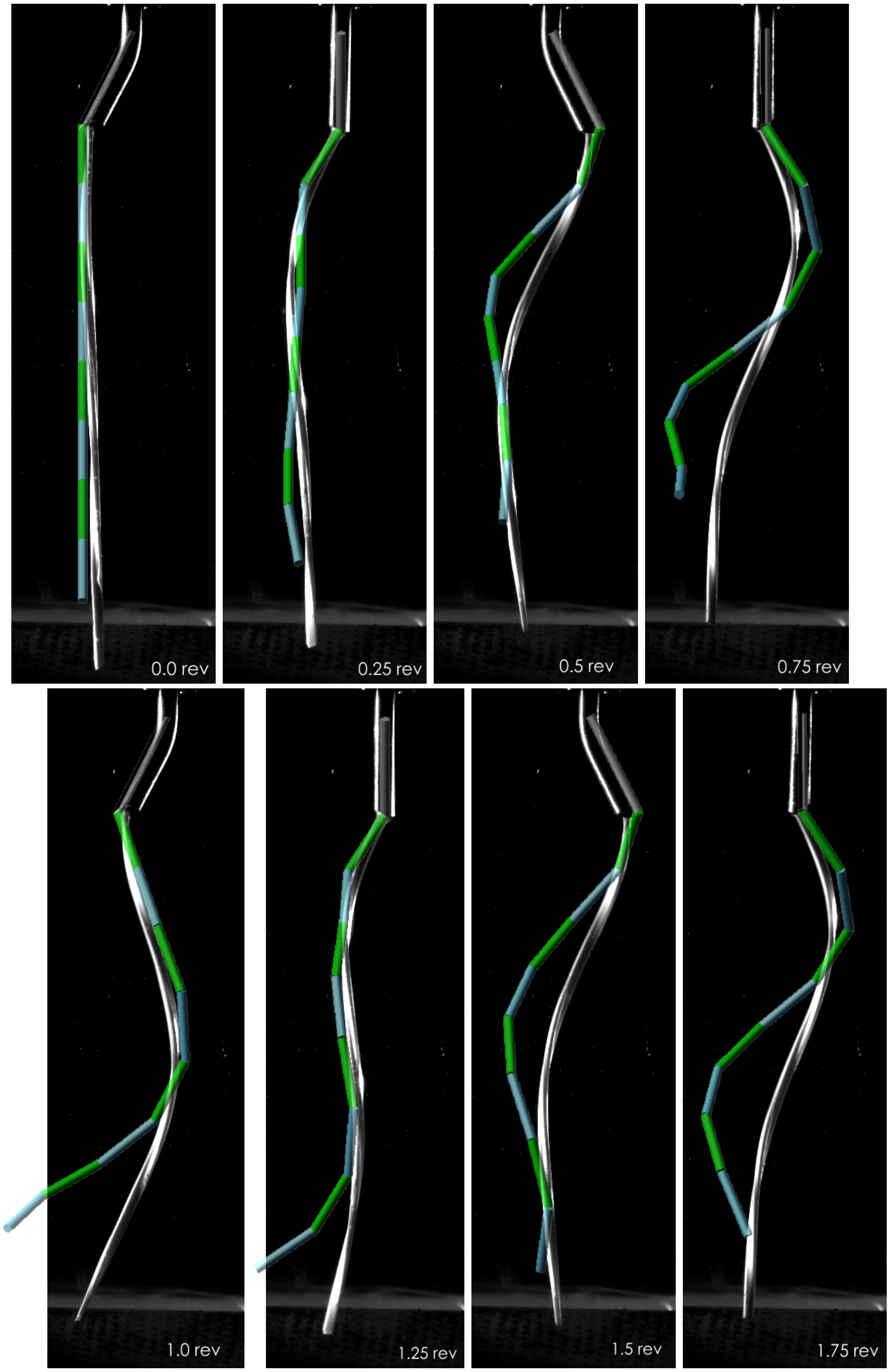

Figure 5.16: ADAMS model overlaid on flexible tail with rectangular cross-section (a)

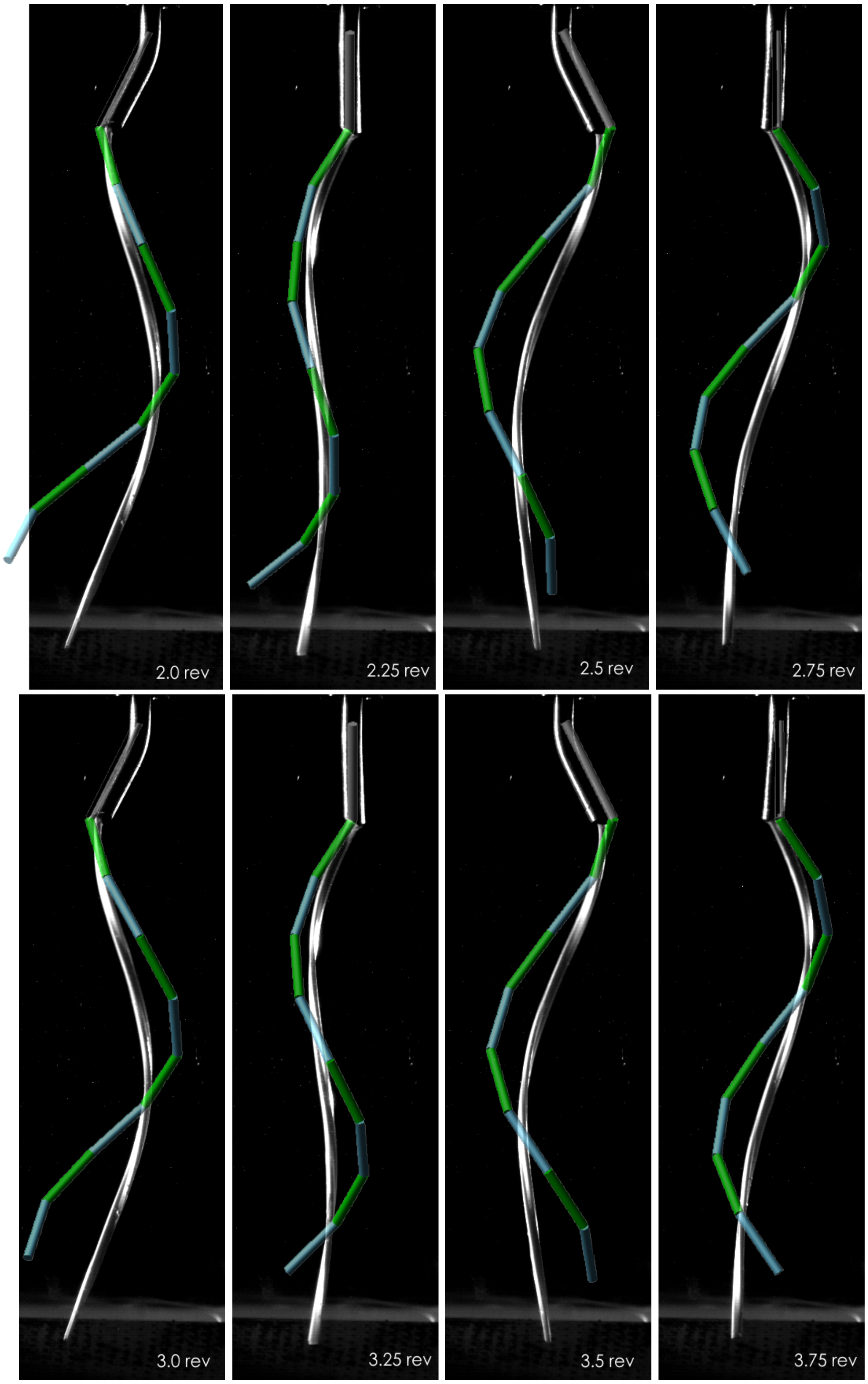

Figure 5.17: ADAMS model overlaid on flexible tail with rectangular cross-section (b)

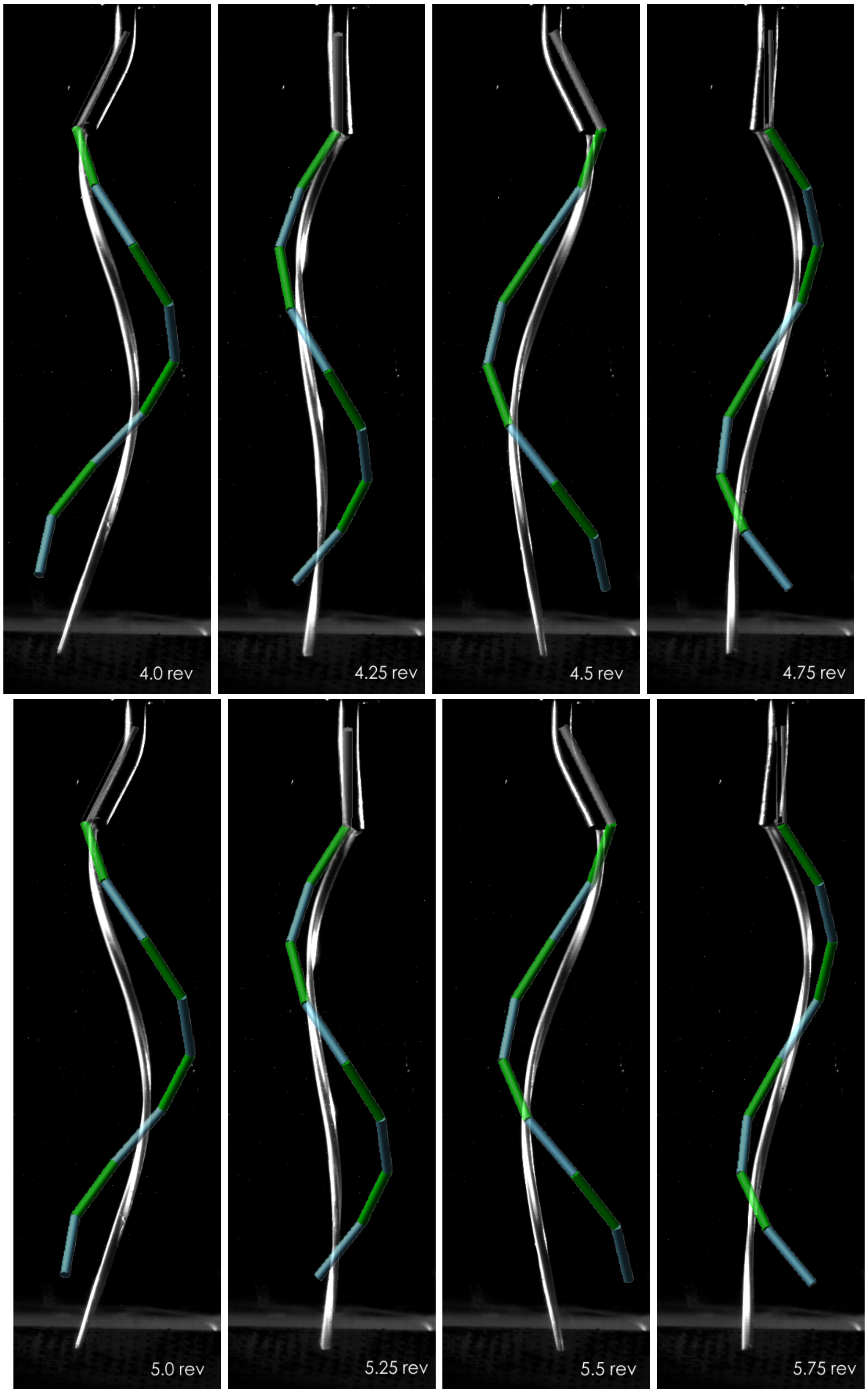

Figure 5.18: ADAMS model overlaid on flexible tail with rectangular cross section (c)

that the filament be designed to have a smaller initial stiffness that varies along the length of the filament by means of a cross-section taper. Whether the taper be thinning, as intuition suggests, or thickening, as the ADAMS models suggests, is still a question to be explored. It is believed that two-stage stiffness is not required because of the small variations in overall shape seen in the experimental filament.

The third issue causing the shape discrepancy is gravity. Recall that the initial design called for a neutrally buoyant tail. The ADAMS model was created assuming that condition would be met. However, the experimental tails are roughly 30% more dense than the fluid they are in and gravity is a factor. Therefore, gravity, and appropriate densities, must be implemented in the ADAMS model to help reduce the discrepancies seen.

That said, despite the correlation issues, the flexible, rectangular cross-section filament, in its current form, does create a propulsion force, albeit, one significantly less than the rigid filament. However, if it is not possible, or desirable, to perform the recommended changes to the design, the system could be used as is. This may be attractive if a thinning taper is required since as the tail thins, less drag force, and consequently less propulsive force, will be generated. This may create a situation where the added propulsive force generated from a more helical shape is not as large as expected.

The flexible, cylindrical cross-section filament also produces propulsive force. In fact, as can be see in Figure 5.15, the cylindrical tail generates more force than its rectangular counterpart. This is most likely due to the difference in shape between the two tails. Accordingly, if the recommendations pertaining to the rectangular tail are not carried out, the cylindrical cross-section filament would be a better choice as a propulsive element.

A point of interest seen from observing the cylindrical filament is that the twisting rectangular cross-section does promote the generation of a helix. Figure 5.19 shows a single revolution of the cylindrical filament during steady-state behaviour. It can be seen that the filament, at best, only contorts into a half-wavelength helix; the rectangular filament contorts into a three-quarter-wavelength helix.

Another point of interest is that the cylindrical filament shape is more dependent on the rotation rate of the rigid link. This is evident in Figure 5.15, which shows that the propulsive force generated by the cylindrical filament is non-linear in nature.

The experimental results show that when dealing with low Reynolds flow propulsion, as stated by Purcell [41], “turn anything–if it isn’t perfectly symmetrical, you’ll swim”. The problem then turns to one of optimizing the effectiveness of the propulsion system. Accordingly, design tools such as a dynamic ADAMS simulation of the propulsion system prove useful. How-

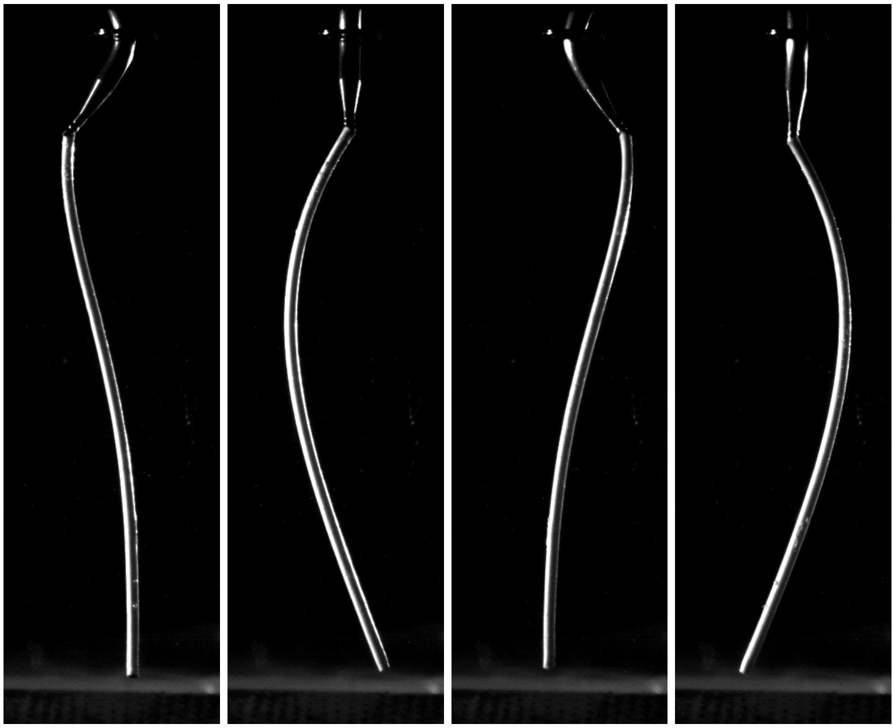

Figure 5.19: A single revolution of the experimental cylindrical filament

ever, at this point, the flexible filament ADAMS model presented does not properly simulate the flexible, rectangular cross-section, experimental filament. This is likely due to inaccurate drag coefficients, the implementation of two-stage stiffness profiles, and the lack of gravity in the ADAMS model.

To determine if the fidelity of the ADAMS model could be increased it was decided to briefly explore a second ADAMS model (ADAMS 2: Flex Tail) that simulates the experimental setup directly (i.e. no scaling). Furthermore, the model utilizes constant stiffness profiles at the joints and contains gravity. The model is built identically to the model described in Section 4.2.1 with two modifications: 1) the torque at each joint is replaced with a torsional spring, and 2) a constant stiffness coefficient is implemented for each torsional spring.

Given the larger scale of the second ADAMS model, the geometric parameters are as listed in Table 5.3. The rotational stiffness coefficient of the joints is derived using a ‘back of the envelope’ approach. First, the silicone used to make the filament, despite being a visco-elastic elastomer, is assumed to be a linear elastic material with a Young’s modulus (E) of 2.6 [MPa] [57]. Second, the continuous filament is assumed to be under small-angle elastic deflection, which is not the case. Then, the deflection of the discrete filament is compared to the deflection of the continuous

Variable	Value
N	8
L_i	14.76 $[mm]$
a	1.2 $[mm]$
β	32.14°
ξ	38.16°
ϕ_1	12.05°
ϕ_{2-8}	24.1°

Table 5.3: Geometric values for second ADAMS model

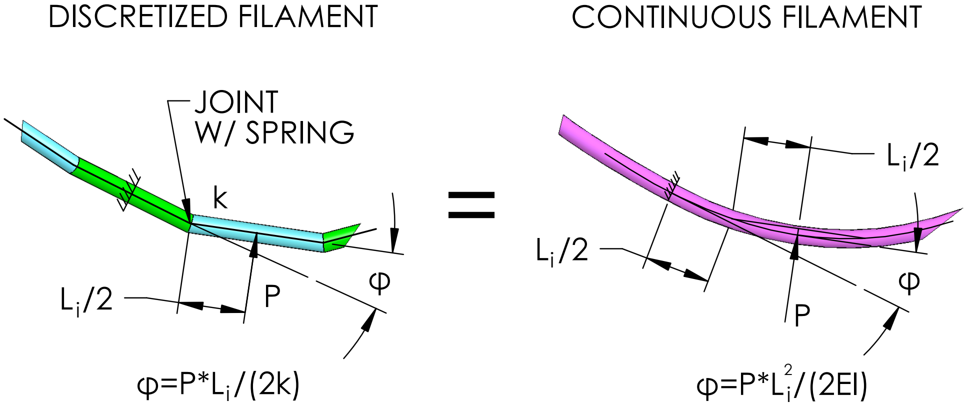

Figure 5.20: Deflection: discretized filament vs. continuous filament

filament (Fig. 5.20). The two situations are equated and the rotational stiffness coefficient (k_{2-8}), for all but the first joint, is solved for:

$$k_{2-8} = \frac{EI}{L_i}, \tag{5.17}$$

where I is the second moment of area for the rectangular cross-section filament. Given the dimensions of the large scale filament, $k_{2-8} = 7.17 \times 10^5$ $[N \cdot m/rad]$. To account for the fact that ϕ_1 is half of ϕ_{2-8}, $k_1 = 2 * k_{2-8}$.

Gravity is implemented, along the appropriate axis, using ADAMS built-in functionality and default values.

Results pertaining to the second ADAMS model are compared to the experimental results for

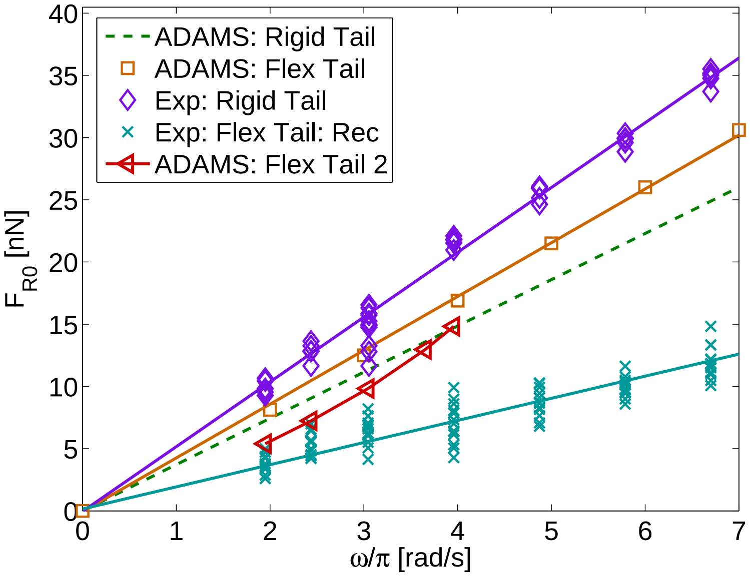

Figure 5.21: Propulsive Force (0 DOF)

the rigid tail and rectangular flexible tail in Figure 5.21. It should be noted that all results, despite being collected at large scale, have been modified to represent small scale values. In this way Figure 5.21 is comparable to all other figures in this work pertaining to 0 DOF propulsive force.

Figure 5.21 shows that the modifications have significantly changed the ADAMS model results. The most positive sign of the changes is that propulsive force generated is much lower than the original ADAMS model filament. Ideally, to be consistent with the rigid tail comparison, the second ADAMS model would have forces 40% less than the experimental setup. Since this is not the case it is evident that the second ADAMS model, while performing closer to the experimental setup, is not perfectly mimicing the dynamics of the experimental set-up. Further evidence of this can be seen in the non-linear response of the filament. It should also be noted that past the $4/\pi$ $[rad/s]$ mark the data is not valid since the ADAMS tail contorted into a secondary steady-state position that does not correspond at all with the results seen during experimental testing.

Figures 5.22 – 5.24 overlay results from the second flexible filament ADAMS model onto high-speed video of the flexible, rectangular cross-section filament. It can be seen that the second ADAMS model more closely models the experimental setup: the two tails trace more similar paths than shown in Figures 5.16 – 5.18. It can also be seen that, like the first ADAMS model, the second ADAMS model filament shows signs of over-rotation. This is due to the ‘back of the envelope’ calculations used to generate rotational stiffness coefficient. It is speculated that the coefficient value predicted is less than the actual tail stiffness.

The results of the second ADAMS model create a feeling of optimism. It is believed that an eight-link lumped parameter approximation using accurate body stiffness coefficients and an accurate drag force model could simulate an experimental filament with good accuracy. This model could then be used as a design tool for fine-tuning of the proposed propulsion system.

Measurement of the required driving torque was carried out using the procedure outlined in Section 5.3.3. Each of the three tails is tested as is the baseline, or no-tail, condition. For each configuration, 15 data points are collected. One data point was eliminated from the flexible, rectangular cross-section tail data because it was an extreme outlier. Once again, the tests were not run until the fluid was calm.

Figure 5.25 shows the raw data along with linear curve fits for each configuration. It can be seen that there is a fair amount of scatter across the data points especially those pertaining to the no-tail configuration. However, positive observations are that the linear curves do not intersect for the testing range and that all tail configurations exhibit, as expected, higher voltage drops than the no-tail configuration. One negative observation is that the difference between the ‘loaded’ curves and the no-tail curve is approximately two orders of magnitude less, at any speed, than the baseline no-tail voltage drop at that speed. In other words, the torque required to overcome friction in the motor and gearbox is two orders of magnitude larger than the torque required to drive the tails. This may cause a situation where signal noise could wash out the small difference being measured. The overlap of data points seen in Figure 5.25 adds evidence that this may be the case.

Nevertheless, the required tail driving torque for each tail is analyzed by subtracting the baseline no-tail voltage. The results are given in Figure 5.26 but the results are not positive. The predicted values for all three tails do not correlate well with the analytical and ADAMS models. Furthermore, the differences are not consistent across the speed range as was seen, for example, in the propulsive force predictions for the rigid tail. Another observation that supports the inaccuracy of the experimental data is that the required driving torque for the rigid tail is less than the ADAMS model predicted. This is a contradiction to the propulsive force comparison: a greater propulsive force should require a greater driving torque. Based on these observations, it is believed that the required driving torque values obtained from the experimental data cannot be considered accurate.

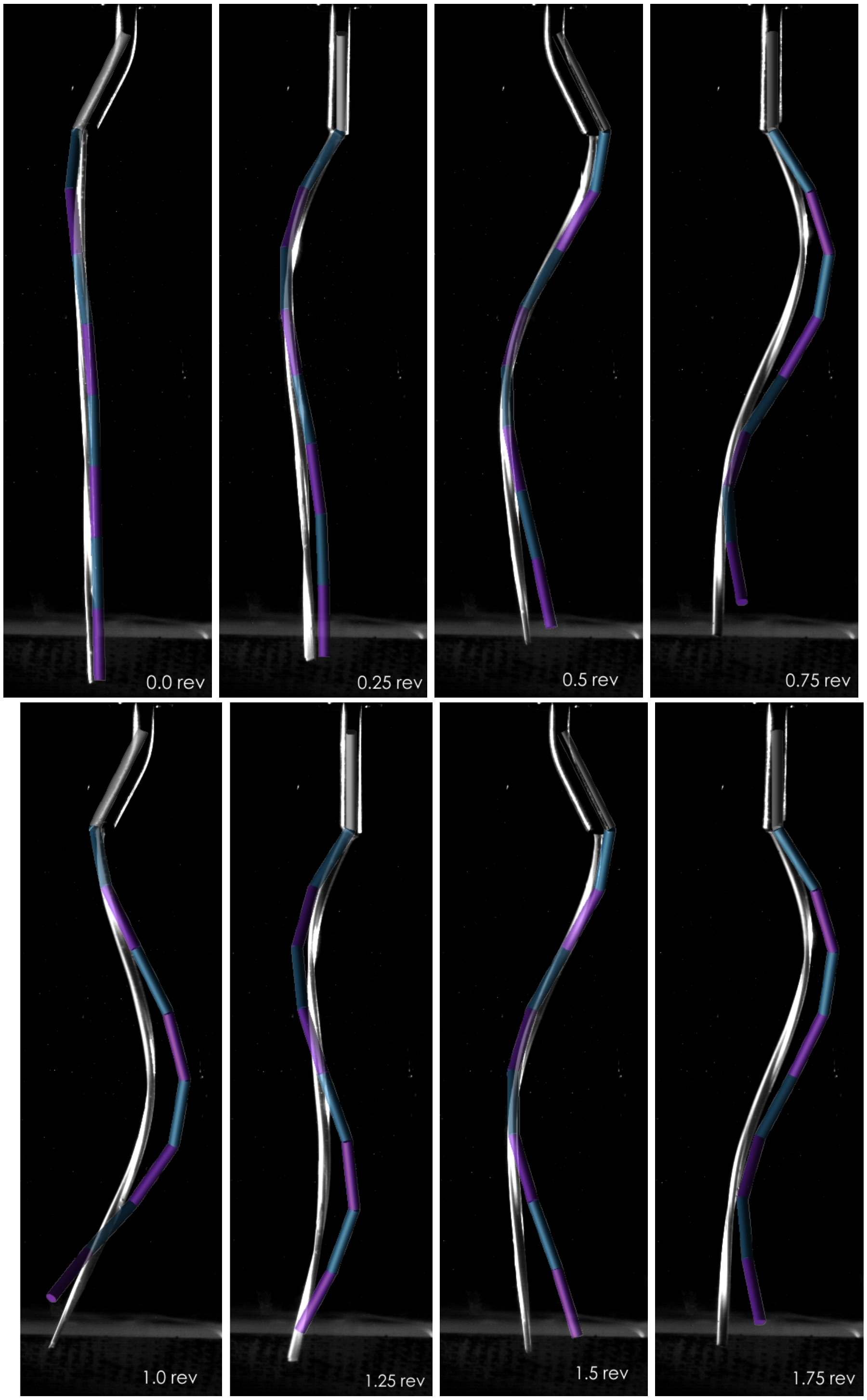

Figure 5.22: ADAMS model with constant stiffness overlaid on flexible tail with rectangular cross-section (a)

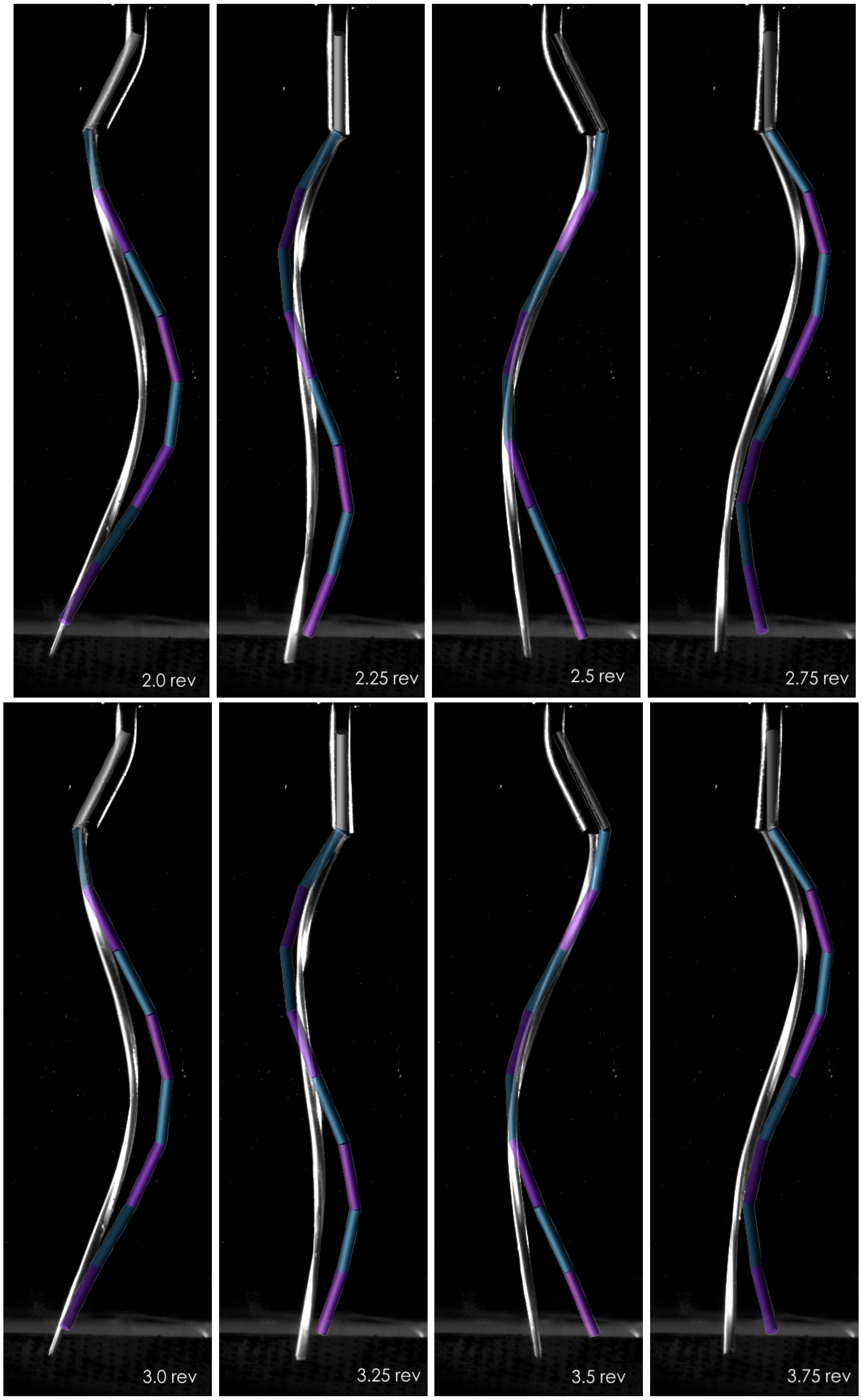

Figure 5.23: ADAMS model with constant stiffness overlaid on flexible tail with rectangular cross-section (b)

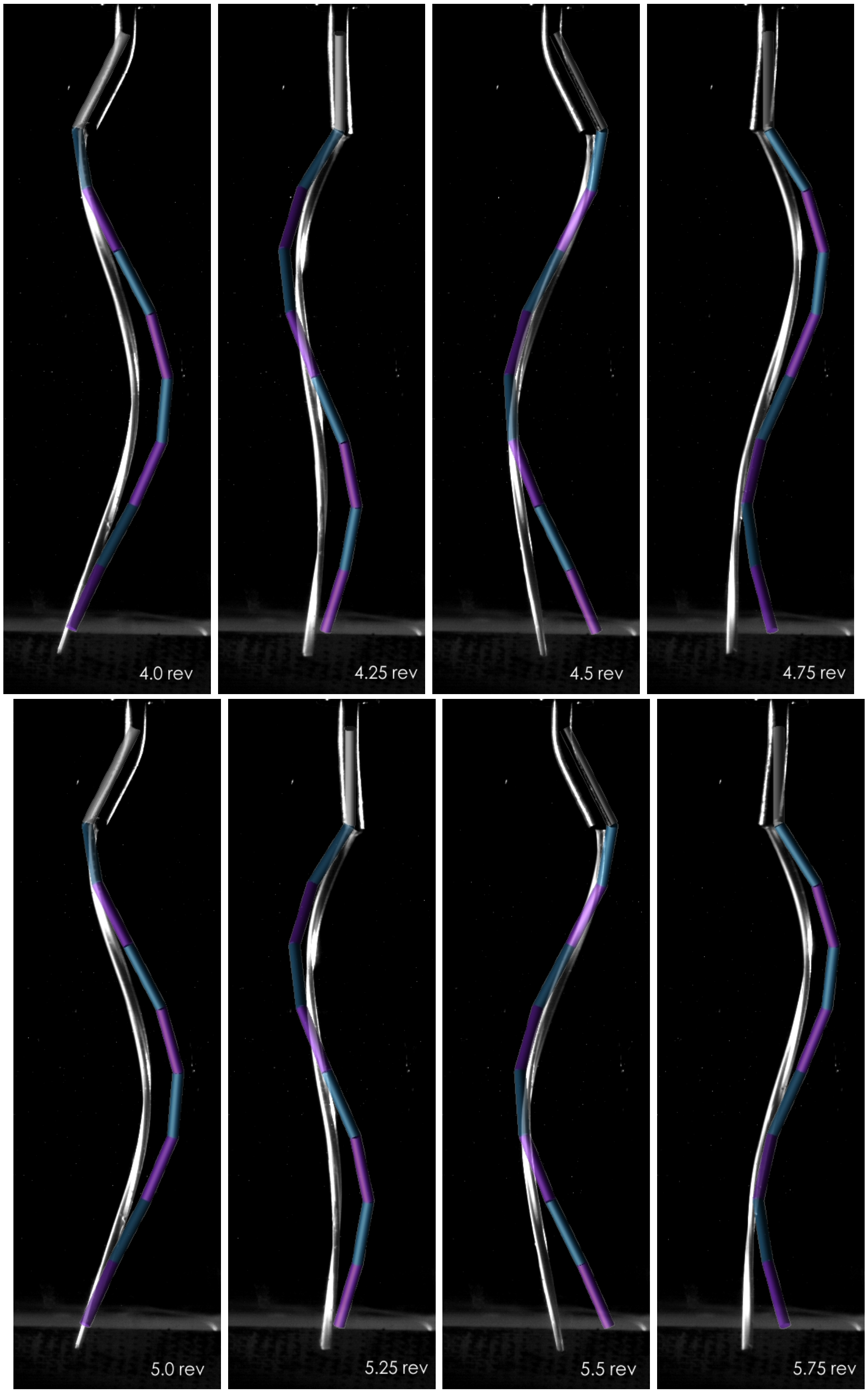

Figure 5.24: ADAMS model with constant stiffness overlaid on flexible tail with rectangular cross-section (c)

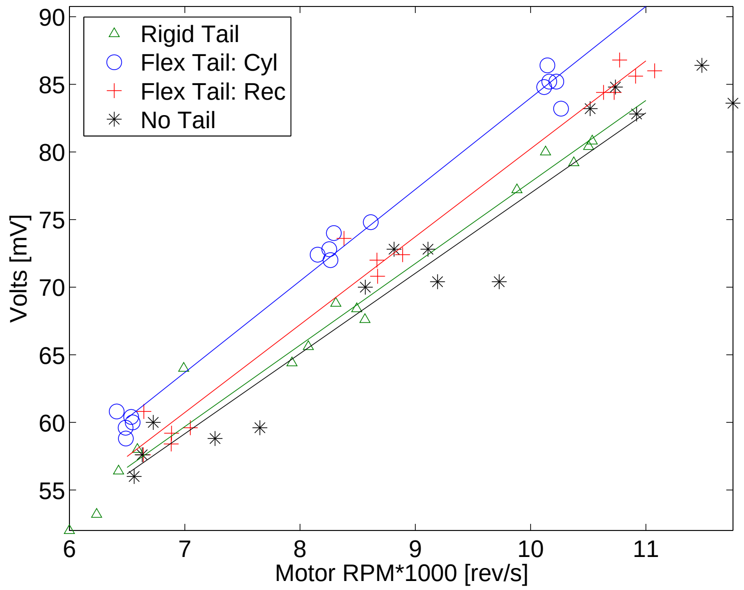

Figure 5.25: Voltage drop across in-line resistor versus motor speed

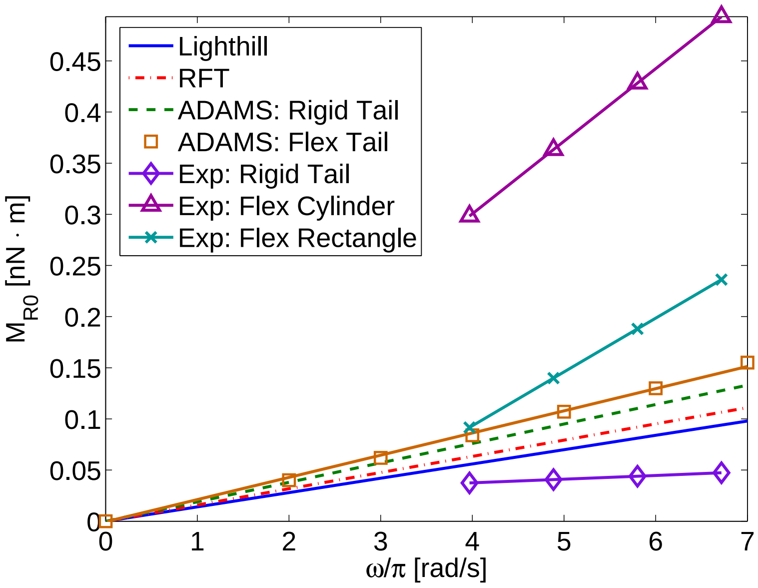

Figure 5.26: Driving Torque (0 DOF)

Chapter 6

Conclusions and Recommendations

This chapter outlines the conclusions and recommendations made throughout the entirety of this report. The information is broken up in terms of the propulsion system design and the modelling and experimental testing. Under the modelling and experimental testing section the information is further split to correspond to the rigid tail and the flexible tail. Lastly, directions for further research are given.

6.1 Propulsion System Design

The original intent of this work was to develop a capsule endoscope system capable of actively exploring the human gastro-intestinal tract. However, based on a literature review, it was decided that current research into this area is well advanced almost to the point of saturation. Accordingly, the focus was shifted to general propulsion through *in vivo*, fluid-filled environments. Further review resulted in the conclusion that, as of yet, no safe, simple propulsion system for swimming micro-robots exists. The development of such a system became the goal for this work.

In addition to the requirement for a safe yet simple system, other design requirements are identified. The largest of these is that the scale of the possible environments dictates that the system must be able to function in a low Reynolds flow environment. From a propulsion point of view this means that the system must utilize a drag-based propulsion system that incorporates non-reciprocal motion. These systems exist in nature and are drawn upon for inspiration. The result is that any proposed system should be based on a prokaryotic flagellum.

One issue with the prokaryotic flagellum is that it is essentially a rigid corkscrew. At larger scales, this type of filament could pose a piercing threat when used inside the human body. To eliminate this danger, it is proposed to use a flexible filament that contorts into a helix under rotational load. This system should have the ability to generate propulsion while being able to simply bend out of the way when it comes into contact with tissue.

The ability of the flexible filament to contort into a complete helix is dependent on three criteria:

1 A balance between viscous drag forces and body stiffness must be achieved so that the desired helix may form under rotational load.
2 Bending of the filament must be predisposed to a predetermined axis. This orientation of this axis twists as one travels down the length of the filament.
3 The base of the helix must be able to adequately resist the reaction loads placed upon it.

The proposed propulsion system uses a flexible, rectangular cross-section filament that twists down its length. The filament is attached to a rigid link which, in turn, is mounted to a large robot body via a rotary actuator. In this configuration the three aforementioned criteria are satisfied.

It should be noted that the proposed rotary actuator is based on the principles of a wobble plate pump. Using this type of actuator could allow for the axis or rotation of the helix to be varied through a conical volume. In this way, it is hoped that the robot could be steered through its environment. It is recommended that any future work regarding steering of a robot utilizing the flexible filament propulsion system should explore this option.

6.2 Modelling and Experimental Testing

To assess the feasibility of the flexible filament design and to explore its capabilities, extensive modeling and experimental testing is carried out. Two analytical models are explored: the resistive-force theory (RFT) model and the Lighthill model. A multi-body dynamic computer model, implemented in MSC.ADAMS, is also explored along with a full finite element (FE) model, implemented in LS-DYNA. Lastly, a scaled-up prototype of the proposed design, along with two other designs (rigid tail and flexible filament with cylindrical cross-section), is tested.

The least successful of these was the FE model; it failed to provide results due to its inability to simulate past the 80 [ms] mark. Furthermore, the results procured during the short simulation time are inconsistent with expected behaviour. There are two possible causes for this failure that should be explored if further work is to be done on the model. First, the boundaries of the fluid control volume may not be simulating the required semi-infinite environment. Second, the coupling algorithm responsible for generating drag force could be based on pressure based drag rather than, as required, viscous force drag. If this is the case, it is likely that LS-DYNA is unable to properly simulate the desired system. A possible alternative is to use the Immersed Boundary General Software Package (IBGSP). This software has been specially developed to computer flows over immersed bodies and is available at the research facility.

6.2.1 Rigid Tail

The experimental results are the benchmark against which the remaining models are measured against. Due to the difficulty in developing a free-swimming robot, the experimental tests are conducted with the robot body fixed. Consequently, only the propulsive force and required driving torque can be recorded. Furthermore, the data procured for the required driving torque is not valid as a result of significant signal noise and the need to measure differences that are two orders of magnitude less than the baseline data. It is recommended that methods to procure the driving torque data be explored since this information will be required when designing a rotary actuator to drive the flexible filament.

The lack of driving torque data means that the experimental results only provide valid propulsive force data. First covered here is the results pertaining to the rigid tail design. As is the case with any experiment there are several identified issues that could add error into the measurements. At the end of each point is a comment, in parentheses, on the assumed severity of the error:

1 A small difference in shape [helix wavelength (λ), filament radius (a), and helix amplitude (b)] between the desired helix and the actual helix (minor).
2 A slightly eccentric axis of rotation for the tail. The tail axis of rotation is not concentric with the axis of the motor (minor).
3 Variation between the actual fluid parameters [fluid viscosity (μ), and fluid density (ρ)] and those used (minor).
4 Error introduced during characterization of the cantilever beam (minor).
5 Error introduced by signal noise (medium).

Items 1 and 2 could be reduced by increasing the precision of the manufacturing techniques used to create the prototype. Item 3 could be reduced by measuring the actual parameters of the fluid and implementing those values in the models. Items 4 and 5 could be reduced by taking more measurements to increase the sample size and increase the accuracy of the curve fit. It is recommended that item 5 be investigated first since the error is most significant.

The RFT model over-predicts the propulsive force of the rigid tail by approximately 20% over the speed range tested ($\omega = 2\pi - 7\pi$ $[rad/s]$). This is qualitatively consistent with work done by Behkam *et. al.* [22–24]. The Lighthill model cannot be compared with the experimental results since, when the body is fixed, the model inaccurately predicts a propulsive force of 0. However, there is thin evidence that suggest that the Lighthill model may be quite accurate. This evidence is based on the relative position of the results when the body is not fixed. The results of the Lighthill model fall close to where intuition suggests experimental results from a 2 degree of freedom experimental set-up would. Validation of the accuracy of the Lighthill model could be accomplished by creating a new test bench that utilizes the previously mentioned 2 degree of freedom (DOF) configuration.

Another conclusion pertaining to the RFT model is that the type of flagella (eukaryotic or prokaryotic) is important to the analysis. The difference between the two types of flagella is explored and quantified, in terms of swimming velocity, in Equation (4.49). The equation shows that as the filament diameter (a) or helix wavelength (λ) increases, so does the difference between the predicted swimming velocity for each system. Furthermore, as the body radius (R) decreases, the difference between the swimming velocity of the two systems increases. This difference can be significant (for this work the difference is 6%) and should be taken into account when modelling using RFT.

It should also be noted, that in RFT the ratio between the tangential resistive force coefficient (C_s) and the normal resistive force coefficient (C_n) is quantified as γ. It has been shown that γ is loosely proportional to the system's efficiency [1]. For cylindrical cross-section filaments γ has an approximate value of 2. It is recommended that other cross-sections be explored to try and increase the value of γ.

The ADAMS model under-predicts the propulsive force of the rigid tail, across the speed range tested, by approximately 40%. This large discrepancy is attributed to modelling error in the form of likely inaccurate drag coefficients. The drag model used was developed by Cox [54] and its accuracy is dependent on a large slenderness ratio (L_i/a) where L_i is the length of the individual link. The slenderness ratio for the links in the ADAMS model is roughly 12. This value is likely too small to create accurate drag coeffients. Recommendations to solve this problem include exploring the use of a scaling factor on the drag coeffients or the implementation of a new drag model.

6.2.2 Flexible Tails

Experimental testing of the flexible, rectangular cross-section tail shows that the proposed design is feasible. When actuated, the filament contorts into a ‘helix-like’ shape that provides propulsive force. However, a complete helix is not created and this causes a discrepancy with the ADAMS model for the flexible filament which over-predicts the propulsive force of the experimental flexible filament by approximately 235% across the speed range tested. Also, the experimental rigid tail generates approximately 280% more propulsive force than the experimental, rectangular cross-section tail.

When the ADAMS model flexible filament is compared to its rigid counterpart, it is evident that the proposed flexible filament design solution has strong potential. The two systems are virtually indistinguishable. In other words, if a flexible filament can be made to contort into a complete helix there is evidence that there will be no loss in performance, compared to the rigid tail, when propulsive force/forward velocity is the goal. This is true even when the body is completely unconstrained, thus simulating a free floating robot. This evidence provides a goal for the experimental system: a flexible filament that can develop similar propulsive force when compared to a rigid helix. Therefore, the existing experimental, flexible, rectangular cross-section filament is analyzed to discover the factors that are limiting the system.

To accomplish this, the experimental filament is compared to the ADAMS model filament to try and identify the source of the 235% discrepancy. The desire is to have the ADAMS model accurately simulate the existing flexible filament. Then, the ADAMS model can be used as a design tool to develop a flexible filament that performs similarly to a rigid tail. While the aforementioned error certainly exists for the experimental setup, the majority of the discrepancy is caused by modelling error. A comparison of the shape of the experimental filament and the shape of the ADAMS flexible filament shows that the two trace very different paths. The main cause for this is the fact that the ADAMS model uses a two-stage elastic stiffness response that varies along the length of the filament while the experimental filament has a constant stiffness down its length. The two-stage profile allows the filament to contort into a complete helix under virtually any load. When designing the experimental filament it was hoped that a full helix would form at an optimal rotational rate. This was the reason for testing at a range of different rotational rates. Unfortunately, this did not happen; the experimental filament was too stiff to ever form a complete helix. Furthermore, the lack of a taper, as was feared, caused the filament to straighten along its length.

Another reason for the shape discrepancy is the lack of gravity in the ADAMS model. When designing the propulsion system it was assumed that the system could be made neutrally buoyant. This assumption is carried over when creating the ADAMS model for the flexible filament. Unfortunately, this requirement could not be met when the experimental filament was made.

To test these hypotheses, a second ADAMS model, attempting to more accurately model the experimental set-up is created. It uses a 'back-of-the-envelope' approach to estimate the experimental flexible filament stiffness. Gravity is also implemented. The results are positive. A qualitative comparison of the second ADAMS model and the experimental filament shows that the two trace paths that match better than the previous comparison. A qualitative comparison also provides positive results; the second ADAMS model predicts propulsive force values that are more in line with the experimental values.

Discrepancy still exists however, and it can be attributed to the 'back-of-the-envelope' modelling technique utilized. It is recommended that more precise methods be used to estimate the stiffness of the filament. Once this is done, and combined with the aforementioned recommendations regarding the ADAMS model drag force coefficients, the author has confidence that the ADAMS model will simulate the experimental filament to a degree of accuracy that will allow for the model to become a useful design tool. If this is not the case, an avenue to explore is the difference between the drag coefficient for a rectangular cross-section filament and the drag coefficient for a circular cross-section filament with equal surface areas. Earlier it is assumed that these values should be similar; however, this has not been verified and may be a source of modelling error.

Some other conclusions regarding the flexible filament can be drawn as well. First, a taper in cross-sectional area is necessary if a complete helix is to be created. This is an addition to the first criteria for helix generation as listed in Section 3.6.1. That said, more testing must be done to determine whether the taper should be thinning, as supported by intuition, or thickening, as supported by the first ADAMS model. If a thinning taper is required it should be noted that the reduction in cross-section will likely reduce the propulsive force of the filament. Therefore, propulsive force gains pertaining to the creation of a complete helix may be less than expected.

Second, it is believed that a two-stage elastic stiffness response is not as necessary as initially thought. The linear response of the experimental, flexible, rectangular cross-section filament shows that the operating margin for the filament is larger than initially expected. Accordingly, it should be possible to tune a filament that generates acceptable propulsive force under varying loads due to varying fluid (μ and ρ) and operational (ω) parameters. Using a constant stiffness profile reduces the complexity of the propulsion system and is more desirable.

Third, based on the ADAMS model results, the drag forces experienced by the tail dominate over the body drag forces. This is evident in the final trajectory of the robot when all constraints are removed from the body; it is in-line with the initial position of the tail. It is believed that the dominance of the tail drag forces may be useful when designing a steering system for the robot and it is recommended that this be examined further.

Lastly, there are several observations regarding the experimental flexible circular cross-section tail that should be mentioned. Like the rectangular cross-section tail, the circular tail also generates propulsive force when actuated. In fact, in the current configuration the circular tail generates more propulsive force. Therefore, if none of the recommendations outlined in this work are implemented, it is recommended that the circular cross-section tail be used. Also, it should be noted that the circular cross-section tail displays a non-linear propulsive force curve meaning that it is more dependent on rotational speed than the rectangular cross-section tail. This may be attributed to the twisting of the cross-section for the rectangular tail, which, as expected, does promote bending along the desired axis.

6.3 Directions for Future Research

The short-term objective for future research should be centred squarely on developing the ADAMS model until the existing flexible filament can be accurately simulated. Then, a new, large-scale filament can be designed that exhibits increased propulsive force — ideally similar in magnitude to the force generated by the rigid tail. It is hoped that this new filament will show definitive proof regarding the abilities of the proposed propulsion system.

At that point, it is foreseeable that the research would branch into two directions. The first direction involves moving toward a free-swimming robot. This requires that a body, rotary actuator, and steering system be designed and fabricated. Once built, the next step is to establish the behaviour of the free-swimming robot so that the required control algorithms can be implemented. Eventually, functionality for exploration, biopsy, and drug-delivery would exist. The second direction would aim at miniaturization of the technology. Techniques need to be explored so that the flexible filament can be manufactured and assembled at the size required for *in vivo* use. This is also true for the body, rotary actuator, steering system, and any required electronics.

Permission to use Copyrighted Material

The following letter was received on August 9, 2006 from the Society for Industrial and Applied Mathematics (SIAM). It gives permission to reuse, from the original source, the image found in Figures 3.6 and 4.4.

Hello,

SIAM is pleased to grant you permission to reprint Figure 12 from Lighthill, J., Flagellar Hydrodynamics, SIAM Review 18 (1976), pp. 161-230 in your master's thesis. Please include the full citation and include the following: "Copyright (C) Society for Industrial and Applied Mathematics. Reprinted with permission."

Please let me know if you have any questions.

Thank you for requesting permission,

Sincerely,

Mary Rose Muccie

Mary Rose Muccie
Publisher, SIAM
P: 215-382-9800 x377
F: 215-386-7999
muccie@siam.org

References

[1] J. Gray and G. J. Hancock, "The propulsion of sea-urchin spermatozoa," *Journal of Experimental Biology*, vol. 32, pp. 802–814, 1955.

[2] J. Lighthill, "Flagellar hydrodynamics," *SIAM Review*, vol. 18, no. 2, 1976.

[3] M. Wybenga, "Developments in in vivo robotic exploration :: A literature review," 2005.

[4] Personal Conversation: Dr. Shane Hadlock, July 2006.

[5] G. Iddan, G. Meron, A. Glukhovsky, and P. Swain, "Wireless capsule endoscopy," *Nature*, vol. 405, p. 417, 2000.

[6] [Online]. Available: http://www.rfnorika.com

[7] [Online]. Available: http://www.givenimaging.com

[8] [Online]. Available: http://www.olympus.co.jp/en/news/2004b/nr041130capsle.cfm?chm=2

[9] M. Sendoh, K. Ishiyama, and K.-I. Arai, "Fabrication of magnetic actuator for use in a capsule endoscope," *IEEE Transactions on Magnetics*, vol. 39, no. 5, pp. 3232–3234, 2003.

[10] [Online]. Available: http://www-crim.sssup.it/research/projects/Emiloc/emiloc.html

[11] B. Kim, Y. Jeong, T. Kim, J. Park, and S. Song, "Micro capsule type robot," US Patent Application 20030092964.

[12] T. S. Kim, B. Kim, D. D. Cho, S. Y. Song, P. Dario, and M. Sitti, "Fusion of biomediacl microcapsule endoscope and microsystem technology," in *Proceedings of the 13th internation conference on Solid-State Sensors, Actuators, and Microsystems*, 2005.

[13] A. Menciassi *et al.*, "Legged locomontion in the gastrointestinal tract," in *Proceedings of 2004 IEEE/RSJ International Conferenct on Intelligent Robots and Systems*, 2004.

[14] C. Stefanini, A. Menciassis, and P. Dario, “Modeling and experiments on a legged microrobot locomoting in a tubular, compliant and slippery environment,” *International Journal of Robotics Research*, vol. 25, no. 5–6, pp. 551–560, 2006.

[15] E. Cheung, M. E. Karagozler, S. Park, B. Kim, and M. Sitti, “A new endoscopic microcapsule robot using beetle inspired microfibrillar adhesives,” in *2005 IEEE/ASME International Conference on Advanced Intelligent Mechatronics*, 2005.

[16] A. Glukhovsky, G. J. Iddan, and G. Meron, “Induction powered in vivo imaging device,” US Patent Application 20020165592.

[17] S. Lewkowicz and A. Glukhovsky, “System and method for controlling a device in vivo,” US Patent Application 20030114742.

[18] G. J. Iddan, “Self propelled device having a magnetohydrodynamic propulsion system,” US Patent Application 20030214580.

[19] ——, “In-vivo extendable element device and system, and method of use,” US Patent Application 20040176664.

[20] ——, “Method and device for imaging body lumens,” US Patent Application 20050004474.

[21] J. Edd *et al.*, “Biomimetic propulsion for a swimming surgical micro-robot,” in *Proceedings of 2003 IEEE/RSJ International Conferenct on Intelligent Robots and Systems*, 2003.

[22] B. Behkam and M. Sitti, “E. coli inspired propulsion for swimming microrobots,” in *Proceedings of 2004 ASME International Mechanical Engineering Conference and R&D Exposition*, 2004.

[23] ——, “Modeling and testing of a biomimetic flagellar propulsion method for microscale biomedial swimming robots,” in *Proceedings of 2005 IEEE/ASME International Conference on Advanced Intelligent Mechantronics*, 2005.

[24] ——, “Design methodology for biomimetic propulsion of miniature swimming robots,” *Transactions of the ASME Journal of Dynamic Systems Measurement and Control*, vol. 128, no. 1, pp. 36–43, 2006.

[25] C. Brennen and H. Winet, “Fluid mechanics of propulsion by cilia and flagella,” *Annual Review of Fluid Mechanics*, vol. 9, pp. 339–398, 1977.

[26] [Online]. Available: http://www.me.cmu.edu/faculty1/sitti/nano/projects/capsules/

[27] J.-B. Mathieu *et al.*, "Preliminary studies for using magnetic resonance imaging systems as a mean of propulsion for microrobots in blood vessels and evaluation of ferromagnetic artefacts," in *IEEE Canadian Conference on Electrical and Computer Engineering*, vol. 2, 2003, pp. 835–838.

[28] J.-B. Mathieu, G. Beaudoin, and S. Martel, "Method of propulsion of a ferromagnetic cor in the cardiovascular system through magnetic gradients generated by an mri system," *IEEE Transactions on Biomedical Engineering*, vol. 53, no. 2, pp. 292–299, 2006.

[29] O. Felfoul, S. Martel, G. Beaudoin, and J.-B. Mathieu, "Micro-device's susceptibility difference based mri positioning system, a preliminary investigation," in *26th Annual Internation Conference of the IEEE EMBS*, 2004.

[30] R. Freitas Jr., *Nanomedicine, Volume II: Biocompatibility*. Landes Bioscience, 2003. [Online]. Available: http://www.nanomedicine.com/NMIIA.htm

[31] ——, *Nanomedicine, Volume I: Basic Capabilities*. Landes Bioscience, 1999. [Online]. Available: http://www.nanomedicine.com/NMI.htm

[32] K. Schmidt, P. Abiodun, and W. Tolckmitt, "Viscosity and electrolyte concentrations in gastric juice from cystic fibrosis children compared to healthy children," *European Journal of Pediatrics*, vol. 136, pp. 193–197, 1981.

[33] M. Grasso and G. Johnson, "Ureteroscopy," 2006, eMedicine. [Online]. Available: http://www.emedicine.com/med/topic3079.htm

[34] R. Burton-Opitz and R. Dinegar, "The viscosity of urine," *American Journal of Physiology*, vol. 47, no. 2, pp. 220–230, 1918.

[35] C. Silberberg, "Urine ph," 2006, medlinePlus Medical Encyclopedia. [Online]. Available: http://www.nlm.nih.gov/medlineplus/ency/article/003583.htm

[36] R. Burton-Opitz and R. Nemser, "The viscosity of lymph," *American Journal of Physiology*, vol. 45, no. 1, pp. 25–29, 1917.

[37] L. Ascari, C. Stefanini, A. Menciassi, S. Sahoo, P. Rabischong, and P. Dario, "A new active microendoscope for exploring the sub-arachnoid space in the spinal cord," in *2003 IEEE International Conference on Robotics & Automation*, 2003.

[38] I. Bloomfielda, I. Johnstona, and L. Bilsont, “Effects of proteins, blood cells and glucose on the viscosity of cerebrospinal fluid,” *Pediatric Neurosurgery*, vol. 28, pp. 246–251, 1998.

[39] H. Gray, *Anatomy of the Human Body*. Lea & Febiger, 1918; Bartleby.com, 2000.

[40] C. S. Nicerson, “Engineering the mechanical properties of ocular tissues,” Ph.D. dissertation, California Institute of Technology, 2005.

[41] E. M. Purcell, “Life at low reynolds number,” *American Journal of Physics*, vol. 45, pp. 3–11, 1977.

[42] A. Bejan and J. H. Marden, “Unifying constructal theory for scale effects in running, swimming and flying,” *The Journal of Experimental Biology*, vol. 209 (Pt. 2), pp. 238–248, 2006.

[43] B. R. Munson, D. F. Young, and T. H. Okiishi, *Fundamentals of Fluid Mechanics*, 4th ed. John Wiley & Sons, Inc., 2002.

[44] P. Cappuccinelli, *Motility of Living Cells*, ser. Outline Studies in Biology. Chapman and Hall Ltd., 1980.

[45] C. J. Brokaw, “Swimming with three-dimensional flagellar bending waves,” September 2003, as Presented at the Second Annual Symposium on Aqua-Biomechanics.

[46] E. Lefison, *Atlas of Bacterial Flagellation*. Academic Press, New York and London, 1960.

[47] E. W. Weisstein, “Helix,” 2006, from MathWorld–A Wolfram Web Resource. [Online]. Available: http://mathworld.wolfram.com/Helix.html

[48] C. J. Brokaw, “Spermatozoan motility: A biophysical review,” *Biological Journal of the Linnean Society*, vol. 7, pp. 423–439, 1975.

[49] C. Brokaw, “Non-sinusoidal bending waves of sperm flagella,” *Journal of Experimental Biology*, vol. 43, pp. 155–169, 1965.

[50] A. Chwang and T. Wu, “A note on the helical movement of micro-organisms,” *Proceedings of the Royal Society of London, Series B, Biological Sciences*, vol. 178, no. 1052, pp. 327–346, 1971.

[51] C. Brokaw, “Bending moments in free-swimming flagella,” *Journal of Experimental Biology*, vol. 53, no. 2, pp. 445–464, 1970.

[52] J. Lighthill, “Helical distributions of stokeslets,” *Journal of Engineering Mathematics*, vol. 30, pp. 35–78, 1996.

[53] R. L. Huston, *Multibody Dynamics*. Butterworth-Heinenmann, 1990.

[54] R. G. Cox, “The motion of long slender bodies in a viscous fluid, part 1. general theory,” *Journal of Fluid Mechanics*, vol. 44, no. 4, pp. 791–810, 1970.

[55] J. O. Hallquist, *LS-DYNA Theory Manual*, 2006. [Online]. Available: http://www.lstc.com/pdf/ls-dyna_theory_manual_2006.pdf

[56] J. S. Bergstrom, “Determination of material parameters for the 8-chain model for use with abaqus, ls-dyna, and ansys.” [Online]. Available: http://polymerfem.com/polymer_files/eightChain_findProperties.pdf

[57] V. Ngai, J. Medley, and L. Jones, “Friction of hydrogel (long-wear silicone and soft disposable) contact lenses,” in *2004 Ontario Biomechanics Conference*, 2004.

[58] M. A. Meyers, *Dynamic Behavior of Materials*. John Wiley & Sons, Inc, 1994.

[59] L. S. T. Corporation, “Ls-dyna advanced course in ale and fluid/structure coupling,” February 2004.

[60] S. Lim and C. S. Peskin, “Simulations of the whilrin instability by the immersed boundary method,” *SIAM Journal on Scientific Computing*, vol. 25, no. 6, pp. 2066–2083, 2004.

Appendix A

ADAMS Model Information

A.1 ADAMS Model Creation

Parameter	Symbol [Units]	Scaling Factor
Mass	$M\ [kg]$	1
Length	$L\ [m]$	1E3
Time	$T\ [s]$	1
Force	$\mathbf{F}\ \left[\frac{kg\,m}{s^2}\right]$	1E3
Torque	$\mathbf{T}\ \left[\frac{kg\,m^2}{s^2}\right]$	1E6
Density	$\rho\ \left[\frac{kg}{m^3}\right]$	1E-9
Velocity	$\mathbf{U}$ or $\mathbf{V}\ \left[\frac{m}{s}\right]$	1E3
Ang. Velocity	ω or $\Omega\ \left[\frac{rad}{s}\right]$	1
Dyn. Viscosity	$\mu\ \left[\frac{kg}{m\,s}\right]$	1E-3
Stiffness Coefficient	$k\ \left[\frac{kg\,m^2}{s^2\,rad}\right]$	1E6

Table A.1: Scaling factors for ADAMS model

A.2 ADAMS Model Results

Joint	ϕ_i $[deg]$ (Actual)	ϕ_i $[deg]$ (Desired)	Actual/Desired
1	14.44	12.05	1.20
2	22.75	24.1	0.94
3	25.15	24.1	1.04
4	27.04	24.1	1.12
5	28.59	24.1	1.18
6	26.30	24.1	1.09
7	24.81	24.1	1.03
8	26.53	24.1	1.10

Table A.2: Joint deflection angles 0 DOF configuration: actual versus desired

Joint	ϕ_i $[deg]$ (Actual)	ϕ_i $[deg]$ (Desired)	Actual/Desired
1	12.61	12.05	1.04
2	22.80	24.1	0.95
3	24.75	24.1	1.03
4	24.64	24.1	1.02
5	25.73	24.1	1.07
6	23.61	24.1	0.98
7	22.23	24.1	0.92
8	23.84	24.1	0.99

Table A.3: Joint deflection angles in 2 DOF configuration: actual versus desired

Joint	ϕ_i [deg] (Actual)	ϕ_i [deg] (Desired)	Actual/Desired
1	12.20	12.05	1.01
2	26.76	24.1	1.11
3	26.76	24.1	1.11
4	25.10	24.1	1.04
5	25.78	24.1	1.07
6	23.43	24.1	0.97
7	22.00	24.1	0.91
8	23.49	24.1	0.97

Table A.4: Joint deflection angles in 6 DOF configuration: actual versus desired

Curve	**Equation**	**Avg. Error**	**Max. Error**
ADAMS: Flex Tail			
F_{R0}	$F_{R0} = 4.32 \times 10^{-9}(\omega/\pi) - 6.88 \times 10^{-11}$	2.1%	5.6%
M_{R0}	$M_{R0} = 2.17 \times 10^{-11}(\omega/\pi) - 4.75 \times 10^{-13}$	2.9%	7.0%
U	$U = 4.05 \times 10^{-5}(\omega/\pi) - 2.71 \times 10^{-7}$	1.3%	3.7%
Ω	$\Omega = 2.09(\omega/\pi) - 0.011$	0.9%	1.7%
F_R	$F_R = 3.82 \times 10^{-10}(\omega/\pi) - 2.55 \times 10^{-12}$	1.3%	3.7%
M_R	$M_R = 6.57 \times 10^{-12}(\omega/\pi) - 3.34 \times 10^{-14}$	0.9%	1.7%
ADAMS: 6 DOF			
U	$U = 4.77 \times 10^{-5}(\omega/\pi) - 1.51 \times 10^{-7}$	4.4%	11.2%
Ω	$\Omega = 2.18(\omega/\pi) - 0.029$	1.8%	4.8%
F_R	$F_R = 4.50 \times 10^{-10}(\omega/\pi) - 1.42 \times 10^{-11}$	4.4%	11.2%
M_R	$M_R = 6.85 \times 10^{-12}(\omega/\pi) - 9.00 \times 10^{-14}$	1.8%	4.8%

Table A.5: Equations, and error analysis, of curve fits for ADAMS model results as plotted in Figures 4.29-4.34, 4.38-4.41, 5.15, 5.21, and 5.26

Appendix B

Test Bench Information

B.1 Product Literature

The following section contains select product literature taken directly from the manufacturer. All documents were obtained from the public domain and are available at the following locations.

- Shell Tellus 100 hydraulic oil: http://www.shell.com/static/ca-en/downloads/shell_for_businesses/oils_lubricants/3-01.pdf
- Faulhauber 0816P006S DC motor: http://micromo.com/uploadpk/e_0816S_MIN.pdf
- Faulhauber series 08/1 64:1 planetary gear-reducer: http://micromo.com/uploadpk/e_081_MIN.pdf
- Faulhauber HEM1016, 10 cycle per revolution, magnetic digital encoder: http://micromo.com/uploadpk/HE.pdf
- Dow Corning 3112 RTV Silicone: http://www.dowcorning.com/applications/search/default.aspx?R=107EN
- Honeywell AL322BL Loadcell: http://www.sensotec.com/pdf_catalog06/13.pdf
- IGUS iglide J, JFI-0405-04, Linear Plain Bearings: http://www.igus.com/pdf/j.pdf
- Faulhauber MCDC2805 motion controller: http://micromo.com/n42044/i120174.html

Lubricants Report

Product Data Sheet from Shell Lubricants

PDS# 3.01.17

SHELL TELLUS*

HIGH PERFORMANCE HYDRAULIC OIL
NOW 'NEW AND IMPROVED'

PRODUCT LINE

Shell **Tellus** Oils have been reformulated using the latest generation anti-wear hydraulic oil chemistry and Shell's high qualilty HVI basestocks. New **Tellus** maintains an exceptional performance profile while achieving improvements in wet filterability, tolerance to contamination and frictional characteristics. Shell **Tellus** now passes Denison's T6C vane pump test.

Tellus anti-wear hydraulic oils are available in a wide viscosity range from ISO grade 22 to 150.

APPLICATIONS

Hydraulic Systems - **Tellus** oils are recommended for use in all hydraulic systems where anti-wear type mineral oils are specified. They provide an outstanding combination of characteristics that protect systems against wear, rust and corrosion and will maintain excellent system oil life without excessive deterioration due to oxidation. These oils also provide superior demulsability, air separation and anti-foam properties, hydrolytic stability, thermal stability and filterability qualities. **Tellus** oils are not recommended for use in pumps containing silver plated components. Please consult your Shell Representative for a lubricant suitable for use in pumps containing silver plated components.

Circulating Systems - All anti-wear **Tellus** Oil grades can also be used in circulating systems calling for Rust and Oxidation (R&O) inhibited oils, where it becomes desirable to rationalize the number of products in use in a plant. In other words, the anti-wear additives in such grades are not a disadvantage in such applications. They will provide excellent lubrication for bearings and gears, under normal loads where an oil with extreme pressure capabilities is not required.

PERFORMANCE BENEFITS

- **Outstanding Anti-Wear Protection** - Proven anti-wear additives are incorporated to be effective throughout the range of operating conditions, including low and severe duty high load conditions. **Tellus** meets the performance requirements of major pump manufacturers including Denison vane and piston pump tests (for Denison HF-0) and Eaton Vickers 35VQ25 and 104C vane pump tests.
- **Oxidation Stability** - Advanced technology **Tellus** resists oxidation degradation and sludge formation even when make-up rates are low, outperforming major competitors in standard industry tests.
- **Superior Filterability** - New improved **Tellus** demonstrates improved wet filterability in the Denison T6C pump wet phase. Suitable for ultra-fine filtration, an essential requirement in today's hydraulic systems. Unaffected by the usual products of contamination, such as water and calcium, which are known to cause blockage of fine filters.
- **Hydrolytic Stability** - Good chemical stability in the presence of moisture which ensures long oil life and reduces the risk of corrosion.
- **Thermal Stability** - Thermally stable in modern hydraulic systems working in extreme conditions of load and temperature. Highly resistant to degradation and sludging. Superior performance demonstrated in the Cincinnati Lamb Thermal Stability Test at 135°C.
- **Low Friction** - New **Tellus** Oils possess high lubrication properties and excellent low friction characteristics in hydraulic systems operating at low or high speed. Prevent the problem of stick-slip in critical applications.
- **Good Water Separation** - The water separation properties (demulsibility) resist the formation of highly viscous water-in-oil emulsions and prevent consequent hydraulic system and pump damage. The rapid oil/water separation properties are demonstrated in the standard ASTM D-1401 test.
- **Excellent Air Release and Anti-foam Properties** - Careful use of additives ensures quick air release without excessive foaming. **Tellus** 22, 32, 46 and 68 are now silicone-free.
- **All Round Versatility** - Suitable for a wide range of other industrial applications.

- **Low Pour Points** - Allow easy equipment start-up at low temperatures. For wide temperature ranges, encountered in equipment operating outdoors and for year-round use, the correct grade of Shell Tellus T Oil is recommended.

PERFORMANCE SUMMARY

Tests and Manufacturer Approvals	**Results**
Denison HF-O, HF-1, HF-2	Approved
Eaton Vickers 35VQ25 vane pump	Pass
Eaton Vickers 104C vane pump	Pass
Cincinnati Lamb P-68, P-69, P-70	Approved

TYPICAL PROPERTIES

GRADE	**22**	**32**	**46**	**68**	**100**	**150**	
PRODUCT CODE	**407-161**	**407-162**	**407-163**	**407-164**	**407-165**	**407-166**	**ASTM METHOD**
Density at 15 °C, kg/m^3;	864.4	868	871.1	874.3	881.6	882.3	D 1298
Colour, max.	1.5	2.0	2.0	2.5	2.5	3.5	D 1500
Pour Point, °C	-36	-33	-30	-27	-27	-24	D 97
Flash Point, COC, °C	208	212	220	236	254	286	D 92
Kinematic Viscosity - mm^2/s at 40 °C - mm^2;/s at 100°C	 21.6 4.23	 32.2 5.52	 46.3 6.94	 68.2 8.88	 96.7 11.0	 147 14.6	 D 445 D 445
Viscosity Index	99	108	106	103	100	98	D 2270
Cu Corrosion at 100 °C	1a	1a	1a	1a	1a	1a	D 130
Rust Test - 24 hrs synthetic seawater	Pass	Pass	Pass	Pass	Pass	Pass	D 665
TAN-E, mgKOH/g	0.6	0.6	0.6	0.6	0.6	0.6	D 664
Aniline Point°C	98	104	108	112	113	119	D 611
Demulsability, minutes to 40/40/0	10	15	20	25	20	20	D 1401

Visit your nearest Shell Associate or90 Reseller for more details.
Need more product information? Please the Shell Helps Centre Technical Desk at 1-800-661-1600 or e-mail us at questions@shell.com
MSDS requests? Please call 1(403)691-2615 or fax your request to 1(403)691-3321.

8/29/2006 10:47 AM

DC-Micromotors

0,15 mNm

Precious Metal Commutation

For combination with
Gearheads:
08/1, 08/2, 08/3
Encoders:
05A, 05AB

Series 0816 ... S

		0816 N		003 S	006 S	008 S	
1	Nominal voltage	U_N		3	6	8	Volt
2	Terminal resistance	R		11,5	47,0	75,7	Ω
3	Output power	$P_{2\,max.}$		0,17	0,16	0,18	W
4	Efficiency	$\eta_{max.}$		52	51	50	%
5	No-load speed	n_o		15 700	15 800	17 100	rpm
6	No-load current (with shaft ø 1,0 mm)	I_o		0,021	0,011	0,009	A
7	Stall torque	M_H		0,41	0,40	0,40	mNm
8	Friction torque	M_R		0,04	0,04	0,04	mNm
9	Speed constant	k_n		5 617	2 851	2 329	rpm/V
10	Back-EMF constant	k_E		0,178	0,351	0,429	mV/rpm
11	Torque constant	k_M		1,70	3,35	4,10	mNm/A
12	Current constant	k_I		0,588	0,299	0,244	A/mNm
13	Slope of n-M curve	$\Delta n/\Delta M$		37 999	39 993	43 003	rpm/mNm
14	Rotor inductance	L		47	195	310	µH
15	Mechanical time constant	τ_m		12	13	14	ms
16	Rotor inertia	J		0,03	0,03	0,03	gcm^2
17	Angular acceleration	$\alpha_{max.}$		138	132	133	$\cdot 10^3 rad/s^2$
18	Thermal resistance	$R_{th\,1} / R_{th\,2}$	30 / 61				K/W
19	Thermal time constant	τ_{w1} / τ_{w2}	2,9 / 207				s
20	Operating temperature range:						
	– motor		– 30 ... + 85				°C
	– rotor, max. permissible		+ 85				°C
21	Shaft bearings		sintered bronze sleeves				
22	Shaft load max.:						
	– with shaft diameter		1,0				mm
	– radial at 3000 rpm (1,5 mm from bearing)		0,5				N
	– axial at 3000 rpm		0,1				N
	– axial at standstill		20				N
23	Shaft play:						
	– radial	≤	0,03				mm
	– axial	≤	0,2				mm
24	Housing material		steel, nickel plated				
25	Weight		3,5				g
26	Direction of rotation		clockwise, viewed from the front face				
Recommended values							
27	Speed up to	$n_{e\,max.}$		13 000	13 000	13 000	rpm
28	Torque up to	$M_{e\,max.}$		0,15	0,15	0,15	mNm
29	Current up to (thermal limits)	$I_{e\,max.}$		0,211	0,103	0,085	A

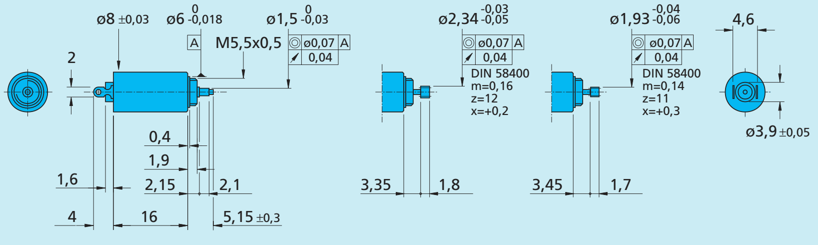

0816 N

0816 P
for Gearhead 08/1

0816 D
for Gearheads 08/2, 08/3

For notes on technical data refer to “Technical Information” in the main catalogue

Edition 17.03.2003

Planetary Gearheads

60 mNm

For combination with
DC-Micromotors:
0816

Series 08/1

	08/1	08/1 K
Housing material	metal	metal
Geartrain material	all steel	all steel
Recommended max. input speed for:		
– continuous operation	8000 rpm	8000 rpm
Backlash, at no-load	≤ 3°	≤ 3°
Bearings on output shaft	sintered sleeve bearings	ball bearings
Shaft load, max.:		
– radial (4,5 mm from mounting face)	≤ 0,8 N	≤ 5 N
– axial	≤ 1 N	≤ 3 N
Shaft press fit force, max.	≤ 5 N	≤ 5 N
Shaft play (on bearing output):		
– radial	≤ 0,03 mm	≤ 0,02 mm
– axial	≤ 0,10 mm	≤ 0,05 mm
Operating temperature range	– 30 ... + 100 °C	– 30 ... + 100 °C

Specifications

reduction ratio	weight without motor g	length without motor L2 mm	length with motor 0816 P L1 mm	output torque continuous operation M max. mNm	output torque intermittent operation M max. mNm	direction of rotation (reversible)	efficiency %
4 :1	2,9	9,6	25,6	60	120	=	90
16 :1	3,8	12,3	28,3	60	120	=	80
64 :1	4,6	15,0	31,0	60	120	=	70
256 :1	5,4	17,7	33,7	60	120	=	60
1 024 :1	6,3	20,4	36,4	60	120	=	55
4 096 :1	7,1	23,1	39,1	60	120	=	48

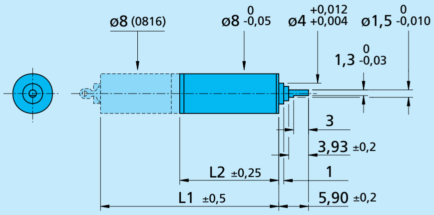

08/1

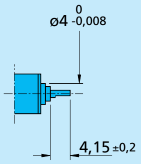

08/1 K

For notes on technical data and lifetime performance
refer to "Technical Information".

Encoders

Magnetic Encoders

Features:
10,12,15 or 16 Cycles per revolution
2 Channels
Digital output

HE

		10 mm technology[3]	15 mm technology	
Signal output (quadrature)		2	2	channels
Supply voltage	V	4.5 to 15.0	4.5 to 15.0	V DC
Current consumption, typical (V_{cc} = 5 V DC)	I_{CC}	5	5[1]	mA
Pulse width	P	180 ± 45	180 ± 45	°e
Phase shift, channel A to B	Φ	90 ± 45	90 ± 45	°e
Logic state width	S	90 ± 45	90 ± 45	°e
Cycle	C	360 ± 30	360 ± 30	°e
Signal rise/fall time, typical	tr/tf	5 / 0.2	5 / 0.2	µs
Frequency range	f	up to 7.2	up to 7.2	khz
Inertia of code disc	J	$2{,}83 \cdot 10^{-7}$	$5{,}79 \cdot 10^{-6}$	oz-in-sec^2
Operating temperature range		–20 to +85 (–4 to +185)	–20 to +85 (–4 to +185)[2]	°C (°F)

[1] current consumption for 1 ppr encoder = 11mA (typical at Vcc = 5 V DC)
[2] operating temperature range for 1 ppr encoder is –20 to 85°C (–4 to 185°F), –40°C operating temperature available on request
[3] not recommended for use with PWM drives

Encoder type	number of channels	Cycles per revolution Ø 10 technology	Ø 15 technology	**in combination with DC-Micromotors and DC-Motor-Tacho units**
HEM 0816	2	10, 12		**series 0816**
HEM 1016, 1219, 1224	2	10, 12		**series 1016, 1219, 1224**
HEM 1319, 1331, 1336	2		1, 10, 12, 15, 16	**series 1319, 1331, 1336**
HEM 1516, 1524, 1624, 1841	2		1, 10, 12, 15, 16	**series 1516, 1524, 1624, 1841**
HEM 1717, 1724, 1727	2		1, 10, 12, 15, 16	**series 1717, 1724, 1727**
HEM 2230, 2233, 2251	2		1, 10, 12, 15, 16	**series 2230, 2233, 2251**
HEM 2338, 2342	2		1, 10, 12, 15, 16	**series 2342**
HEM 2842, 3042	2		1, 10, 12, 15, 16	**series 2642, 2657, 2842, 3042**
HEM 3557	2		1, 10, 12, 15, 16	**series 3557**

Phase Relationship (with clockwise motor shaft rotation as seen from the shaft end)

HEM1016 thru HEM12.. 10 or 12 CPR	**Channel A leads channel B**
HEM1319 thru HEM35.. with 15 CPR	**Channel A leads channel B**
HEM1319 thru HEM35.. with 1, 10, 12 or 16 CPR	**Channel B leads channel A**

These incremental shaft encoders in combination with the FAULHABER® DC-Micromotors are designed for indication and control of both shaft velocity and direction of rotation as well as for positioning.

Solid state Hall sensors and a low inertia magnetic disc provide two channels with 90° phase shift.
The supply voltage for the encoder and the DC-Micromotor as well as the two channel output signals are interfaced with a ribbon cable to a 6-pin connector on motors ≤ 22mm in diameter.

Motors ≥ 23mm in diameter the motor voltage is supplied separately.

Details for the DC-Micromotors and suitable reduction gearheads are on separate catalog pages.

Please note: Velocity (rpm) = f (Hz) x 60/N

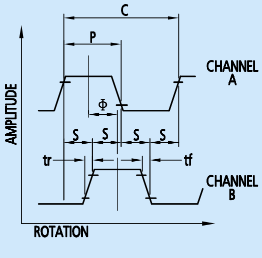

OUTPUT SIGNALS
with clockwise rotation as seen from the shaft end

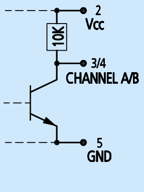

OUTPUT CIRCUIT
* Motors 2342 and larger have separate motor connections

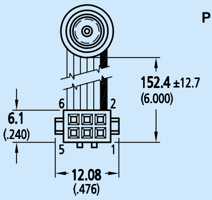

STANDARD CONNECTOR (-6P)
(Berg / FCI 71601-106)
Polarized
.050" Ribbon cable - PVC
6 conductors - 28 AWG
Mating connector:
Header / FCI 75869-131

PIN FUNCTION

1	*	MOTOR (+)
2		Vcc
3		CHANNEL A
4		CHANNEL B
5		GND
6	*	MOTOR (-)

For notes on technical data refer to "Technical Information". Specifications subject to change without notice. MME0506

HE

Encoder HEF Free standing

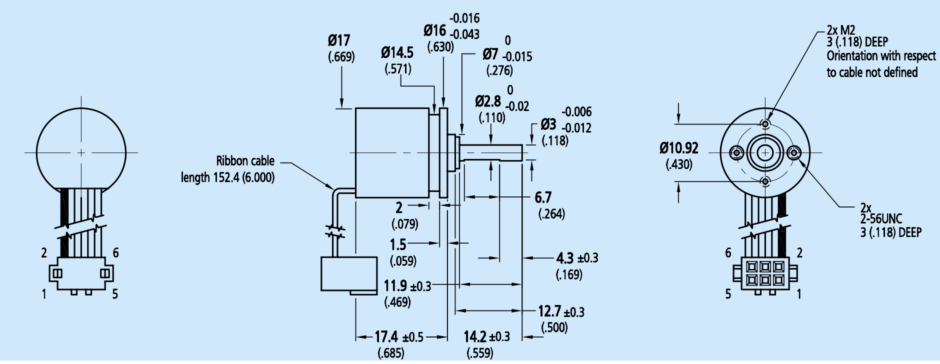

Encoder HEM 1016 & HEM 12...

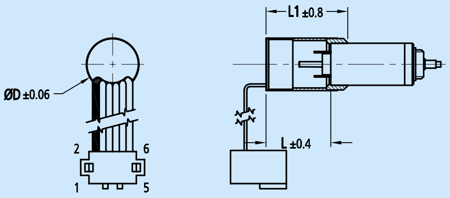

MODEL	ØD	L	L1
HEM 0816	10 (.394)	12.3 (.453)	15.5 (.650)

HEM 0816

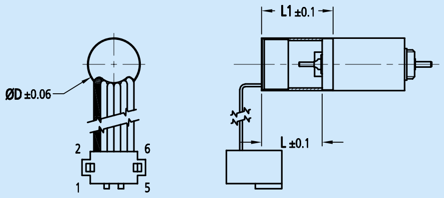

MODEL	ØD	L	L1
HEM 1016	10 (.394)	11.5 (.453)	13.5 (.531)
HEM 12..	12 (.472)	11.5 (.453)	11.5 (.453)

HEM 10../12..

Encoder HEM 13...

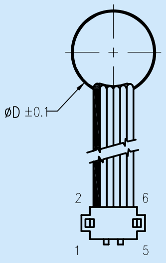

Rear View

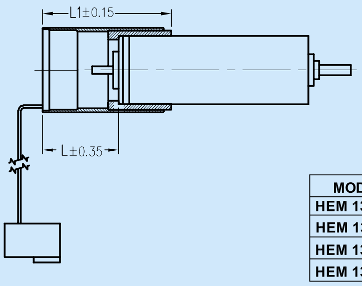

HEM 13..

MODEL	ØD	L1	L
HEM 1319	16 (.630)	20.5 (.807)	14.4 (.567)
HEM 1331E	16 (.630)	32.69(1.287)	14.5 (.571)
HEM 1331T	16 (.630)	23 (.906)	14.4 (.567)
HEM 1336	16 (.630)	23 (.906)	14.4 (.567)

For notes on technical data refer to "Technical information". Specifications subject to change without notice. MME0506

PRODUCTINFORMATION

Information About *Dow Corning* ®3110, 3112, and 3120 RTV Rubbers

Type

Two-part RTV silicone rubber

Color

Dow Corning 3110 and 3112
RTV Rubbers – White
Dow Corning 3120 RTV Rubber – Red

Physical Form
– As Supplied
Pourable liquid –
As Cured
Firm, flexible silicone rubber; at room temperature, choice of four catalysts offers cure times ranging from 12 minutes to 12 or more hours

Primary Uses
Potting and encapsulating of electircal/electronic products; moldmaking RTV Rubbers

DESCRIPTION

Encapsulants

Dow Corning ® 3110, 3112 and 3120 RTV Rubbers are pourable rubber bases that become firm, flexible silicone rubber when cured. They can be cured with any of four catalysts. The cured rubbers exhibit good dielectric properties, and various combinations of base and catalyst allow a wide range of working times and curing rates that can satisfy most potting, coating and moldmaking needs.

These RTV rubbers:

- Are easily mixed and poured
- Cure at room temperature in any thickness
- Give accurate reproduction of masters for moldmaking
- With primer, can obtain strong adhesion to many surfaces
- Provide wide service temperature ranges
- Absorb mechanical shock and vibration

Catalysts

Usually, a recommended mixing ratio of 10:1 base to catalyst assures more accurate measuring and mixing of catalyst, particularly when automatic equipment is used to mix and/or dispense the RTV silicone rubber.[1] Do not use *Dow Corning* ® RTV Catalyst S or F when molding polyesters because the polyester can be inhibited.

HOW TO USE

Preparation of Units

To ensure maximum reliability and complete environmental protection, the following procedure should be followed:

1. Clean assembly of all contaminants such as oil, grease, solder flux, moisture and dirt.

2. For strong adhesion, dip, spray or brush surfaces with *Dow Corning* ® 1201 RTV Primer and allow to cure at least 30 minutes. Silicone rubber surfaces should not be primed, but should be abraded and cleaned.

Catalyst Selection

A common catalyst concentration is 10 percent by weight of the RTV base. Varying the catalyst concentration will change the curing rate as indicated in Table II. Decreasing the catalyst level will slow the cure and give longer working and demold times.

Dow Corning ® RTV Catalyst 4 is used where very fast curing is necessary for polyester molds. The recommended mixing ratio is 200:1.

Dow Corning RTV Catalyst F is used for high speed production. It is ideally suited for use with automated mixing-dispensing equipment, where the mixing is done in a mixing head immediately before dispensing. *Dow Corning* RTV Catalyst F will lose its activity rapidly when exposed to air. Keep all catalyst containers tightly closed when not in use.

Mixing

Dow Corning 3110 RTV Rubber base should be stirred before using, since filler separation may occur upon prolonged standing.

Catalysts can be added to the base material in its shipping container or any clean, dry container. If vacuum deairing is planned, the container should be no more than one-half full to allow for the expansion during the vacuum cycle.

Either hand mixing or mechanical mixing is satisfactory. With either method, care should be taken not to whip large amounts of air into the mixture. Avoid vigorous mechanical mixing since sufficient frictional heat may be generated to accelerate the cure rate.

---

[1] A 10:1 mixing ratio is not recommended for *Dow Corning* RTV Catalyst 4.

DOW CORNING

TYPICAL PROPERTIES

These values are not intended for use in preparing specifications.

		Dow Corning 3110 RTV Rubber[1]	*Dow Corning* 3112 RTV Rubber[1]	*Dow Corning* 3120 RTV Rubber[1]
Processing Considerations				
	Color	White	White	Red
ASTM D 1084B	Viscosity at 25°C (77°F), poise	130	280	280
ASTM D 792A	Specific Gravity at 25°C (77°F)	1.14	1.30	1.45
MIL-S-23586	Corrosion Resistance	Good/Pass[2]	Good/Pass[2]	Good/Pass[2]
Physical and Chemical Properties				
	Radiation Resistance, Cobalt 60 Source, 25°C (77°F), megarads	100	100	100
	Useful Temperature Range, °C (°F)	- 55 to 200 (- 67 to 392)	- 55 to 250 (- 67 to 482)	- 55 to 300 (- 67 to 572)
ASTM D 2214	Thermal Conductivity, Cenco-Fitch, 25-100°C (77-212°F), gm cal/cm^2 sec-(°C/cm)	$5.7x10^{-4}$	–	$7.5x10^{-4}$
	Volume Expansion, 25-150°C (77-302°F), cc/cc/°C	$7.35x10^{-4}$	$8.85x10^{-4}$	$10.5x10^{-4}$
Mechanical Properties				
ASTM D 412	Tensile Strength, die C, psi	400	700	900
ASTM D 412	Elongation, die C, percent	175	130	120
ASTM D 2240	Durometer Hardness, Shore A, points	45	60	60
Electrical Properties				
ASTM D 150	Dielectric Constant at 25°C (77°F), at 100 Hz	2.29	3.25	4.19
	100 kHz	2.20	3.20	3.54
ASTM D 150	Dissipation Factor at 25°C (77°F), at 100 Hz	0.010	0.030	0.070
	100 kHz	0.0010	0.004	0.017
ASTM D 149	Dielectric Strength, 1/16" sample, volts/mil	434	545	457
ASTM D 257	Volume Resistivity, 500 V dc, ohm-cm	$7.3x10^{13}$	$4.2x10^{13}$	$2.7x10^{13}$

---

[1] Using *Dow Corning* RTV Catalyst F or S at 10:1 base to catalyst ratio. Wide departures from normal 10:1 ratio may slightly alter physical properties such as hardness and elongation.

[2] With *Dow Corning* RTV Catalysts F and S.

Specification Writers: Please obtain a copy of the Dow Corning Sales Specification for this product and use it as a basis for your specifications. It may be obtained from any Dow Corning Sales Office, or from Dow Corning Customer Service in Midland, MI. Call (517) 496-6000.

Table I: Catalysts

Catalyst	**Color**	**Consistency**	**Demold Time**	**Cure Conditions**
F (Fast rate)	light tan	paste	25 minutes - 2 hours	room temperature – any thickness or in confined spaces
S (Standard rate)	light blue	paste	5-12 hours	room temperature – any thickness or in confined spaces
1 (Same as S but no corrosion inhibitor)	light blue	paste	5-12 hours	room temperature – any thickness or in confined spaces
4 (Fast rate, 200:1 ratio, no corrosion inhibitor)	clear straw	liquid	10 minutes-2 1/2 hours	room temperature – any thickness or in confined spaces

Model 13 Subminiature Load Cell

Order Code AL322

- 150 g to 1,000 lb.
- mV/V Output
- Stainless Steel
- Single Diaphragm Construction

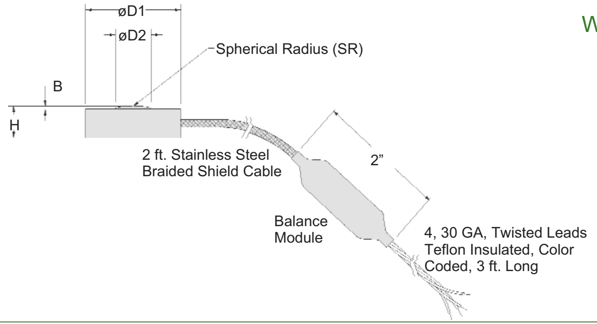

Wiring Code

Cable/ Unamplified

Red	(+) Excitation
Black	(-) Excitation
Green	(-) Output
White	(+) Output

Dimensions

Ranges	D1 (in.)	D2 (in.)	H (in.)	B (in.)	SR (in.)
150; 250; 500; 1000 g 5; 10; 25; 50 lb.	0.38	0.09	0.13	0.027	0.25
100; 250 lb.	0.50	0.12	0.15	0.020	0.50
500; 1000 lb.	0.75	0.25	0.25	0.025	0.50

Performance

Load Ranges	150; 250; 500; 1000 g; 5; 10; 25; 50; 100; 250; 500; 1000 lb.
Linearity	+/- 0.5% Full Scale
Hysteresis	+/- 0.5% Full Scale
Non-Repeatability	+/- 0.1% Full Scale
Output (tolerance)	
150 g to 500 g	15 mV/V (nominal)
1000 g	1.5 mV/V (nominal)
5 lb. to 1000 lb.	2 mV/V (nominal)
Operation	Compression Only
Resolution	Infinite

Environmental

Temperature, Operating	-65° to 250° F
Temperature, Compensated	60° to 160° F
Temperature, Effect	
Zero	0.01% Full Scale/ °F
Span	0.02% Reading/ °F

Electrical

Strain Gage Type	
150 g to 500 g	Semiconductor
1000 g to 1000 lb.	Bonded Foil
Excitation (calibration)	5 VDC
Insulation Resistance	5000 Megohms @ 50 VDC
Bridge Resistance (tolerance)	
150 g to 500 g	500 Ohms (nominal)
1000 g to 1000 lb.	350 Ohms (nominal)
Zero Balance (tolerance)	+/- 3% of Full Scale (nominal)
Shunt Calibration Data	Included
Electrical Termination (std)	5' Integral cable with balance board (note 3)

Mechanical

Maximum Allowable Load	See table
Weight	See table
Material	Stainless Steel
Deflection @ Full Scale	See table

Model 13

Deflections and Weight

Capacity	Deflection at Full Scale (10^{-3} in.)	Weight (g)	Weight with Cable (g)	Maximum Allowable Load (note 1) (%F.S.)
150 g	0.06	1	9	500
250 g	0.06	1	9	500
500 g	0.08	1	9	500
1000 g	0.05	1	9	150
5 lb.	0.5	1	9	150
10 lb.	0.4	1	9	150
25 lb.	0.4	1	9	150
50 lb.	0.4	1	9	150
100 lb.	0.4	3	11	150
250 lb.	0.5	3	11	150
500 lb.	0.5	10	18	150
1000 lb.	0.6	10	18	150

Typical System Diagram

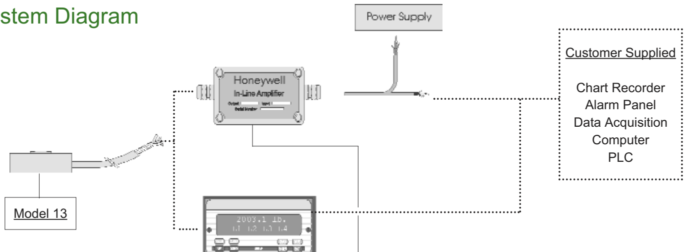

Display Units

SC500
SC1000
SC2000
SC2001
SC3004
GM
NK
HH

In-Line Amplifiers
(Used with unamplified units only)

Amplifier	Output
Universal In-Line Amplifiers	
UV	+/- 5 VDC
UV-10	+/- 10 VDC
UBP	0 +/- 5 VDC
U3W	4-20 mA (3 wire)
DIN Rail Mount In-Line Amplifiers	
DV-05	0 +/- 5 VDC (3 wire)
DA-05	4-20 mA (3 wire)
DV-10	0 +/- 10 VDC (3 wire)

Range Codes

Range	Range Code
150 g	AL
250 g	AN
500 g	AP
1000 g	AR

Range	Range Code
5 lb.	AT
10 lb.	AV
25 lb.	BL
50 lb.	BN
100 lb.	BR
250 lb.	CN
500 lb.	CR
1000 lb.	CV

J

iglide® J

Telephone 1-888-803-1895
Fax 1-401-438-7680

Internet: http://www.igus.com
E-Mail: webmaster@igus.com
QuickSpec: www.igus.com/qs/iglide.asp

igus®

iglide® J - Linear Plain Bearing

Price Index

● ◐ ○

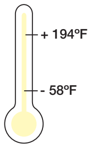

3 Styles
More than 517 Dimensions
Inner Diameters
From 1/8 - 1-5/8 in. (2.5 - 75 mm)

When to use iglide® J plain bearings:

- When very low coefficients of friction are necessary
- When a cost effective bearing for low pressure loads is needed
- For high speeds
- For high wear resistance

When not to use iglide® J plain bearings:

- When high pressure loads occur
  ➤ iglide® G300, iglide® L280
- When temperatures occur that are greater than 248°F for a short-term
  ➤ iglide® G300

Structure of the Part Number:

J S I - 0 2 0 3 - 0 3
d1 d2 b1 (s-Thrust Washer)
Dimension: I - Inch (in 1/16”)
M - Metric (in mm)
Type: S - Sleeve
F - Flange
T - Thrust Washer
Material

Table 6.1 - Material Table

General Properties	Unit	iglide® J	Testing Method
Density	g/cm^3	1.49	
Color		yellow	
Max. moisture absorption at 73°F/50% r.h.	% weight	0.3	DIN 53495
Max. moisture absorption	% weight	1.3	
Coefficient of friction, dynamic against steel	µ	0.06 - 0.18	
p x v value, max. (dry)	psi x fpm	9700	
Mechanical Properties			
Modulus of elasticity	psi	348,000	DIN 53457
Tensile strength at 68°F	psi	10,585	DIN 53452
Compressive strength	psi	8,700	
Permissible static surface pressure (68°F)	psi	5,075	
Shore D-hardness		74	DIN 53505
Physical and Thermal Properties			
Max. long-term application temperature	°F	194	
Max. application temperature, short-term	°F	248	
Min. application temperature	°F	-58	
Thermal conductivity	W/m x K	0.25	ASTM C 177
Coefficient of thermal expansion (at 73°F)	$K^{-1} \times 10^{-5}$	10	DIN 53752
Electrical Properties			
Specific volume resistance	Ωcm	$> 10^{13}$	DIN IEC 93
Surface resistance	Ω	$> 10^{12}$	DIN 53482

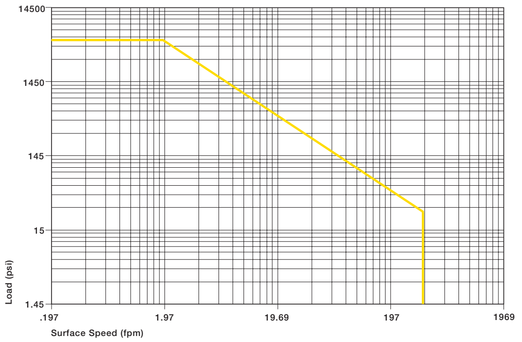

Graph 6.1: Permissible p x v value for iglide® J running dry against steel shaft, at 68°F

iglide® J - Linear Plain Bearing

Installation Tolerances

iglide® J plain bearings are designed to be oversized before being pressfit. After proper installation into a recommended housing bore, the inner diameter adjusts to meet our specified tolerances. Please adhere to the catalog specifications for housing bore and recommended shaft sizes. This will help to ensure optimal performance of iglide® plain bearings.
Please contact an iglide® technical expert for support.

➤ Tolerance Table, Page 1.24
➤ Testing methods, Page 1.25

Friction and Wear

Graph 6.5 shows the coefficients of friction for different loads. The coefficient of friction level is very good for all loads with iglide® J.
Friction and wear are also dependent, to a large extent, on the shafting partner. With increasing shaft roughness, the coefficient of friction also increases.
The best case is a ground surface with an average roughness Ra = 4 to 12 rms.

➤ Coefficients of Friction and Surfaces, Page 1.17
➤ Wear Resistance, Page 1.18

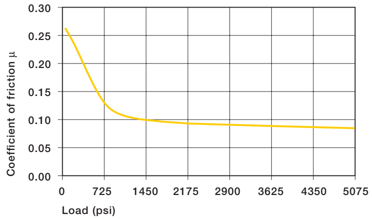

Graph 6.5: Coefficient of friction of iglide® J as a result of the load, v = 1.97 fpm

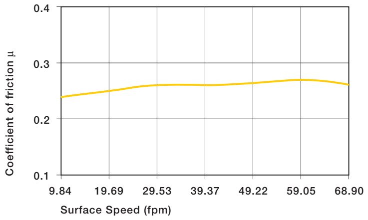

Graph 6.4: Coefficient of friction of iglide® J as a result of the surface speed; p = 108 psi

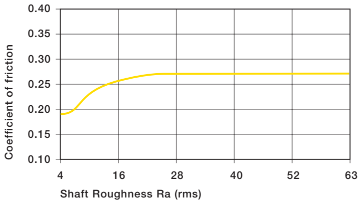

Graph 6.6: Coefficient of friction of iglide® J as result of the shaft surface (shaft Cold Rolled Steel)

iglide® J	Dry	Grease	Oil	Water
Coefficient of Friction µ	0.06 - 0.18	0.09	0.04	0.04

Table 6.4: Coefficients of friction for iglide® J against steel (Ra = 40 rms, 50 HRC)

igus®

iglide® J - Linear Plain Bearing Sleeve Bearing, Inch

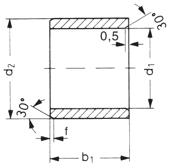

Based on I.D.
f = .019 → $d_1 \le .393$
f = .031 → $.39 < d_1 \le 1.181$
f = .047 → $d_1 > 1.259$

Length Tolerance (b1)

Length (inches)			Tolerance (h13)
0.1181	to	0.2362	-0.0000 /-0.0071
0.2362	to	0.3937	-0.0000 /-0.0087
0.3937	to	0.7086	-0.0000 /-0.0106
0.7086	to	1.1811	-0.0000 /-0.0130
1.1811	to	1.9685	-0.0000 /-0.0154
1.9685	to	3.1496	-0.0000 /-0.0181

Part Number	d1	d2	b1	I.D. After Pressfit		Housing Bore		Shaft Size	
				Max.	Min.	Max.	Min.	Max.	Min.
JSI-1416-12	7/8	1	3/4	.8791	.8757	1.0005	.9997	.8741	.8729
JSI-1418-12	7/8	1 1/8	3/4	.8809	.8775	1.1255	1.1250	.8750	.8740
JSI-1418-24	7/8	1 1/8	1 1/2	.8809	.8775	1.1255	1.1250	.8750	.8740
JSI-1618-16	1	1 1/8	1	1.0041	1.0007	1.1255	1.1250	.9991	.9979
JSI-1618-24	1	1 1/8	1 1/2	1.0041	1.0007	1.1255	1.1250	.9991	.9979
JSI-1620-16	1	1 1/4	1	1.0059	1.0025	1.2510	1.2500	1.0000	.9990
JSI-1620-24	1	1 1/4	1 1/2	1.0059	1.0025	1.2510	1.2500	1.0000	.9990
JSI-1822-16	1 1/8	1 3/8	1	1.1327	1.1276	1.3760	1.3750	1.1250	1.1240
JSI-2022-14	1 1/4	1 3/8	7/8	1.2548	1.2508	1.4068	1.4058	1.2488	1.2472
JSI-2024-24	1 1/4	1 1/2	1 1/2	1.2600	1.2532	1.5005	1.4995	1.2500	1.2490
JSI-2426-32	1 1/2	1 5/8	2	1.5100	1.5032	1.6568	1.6558	1.4988	1.4972
JSI-2428-24	1 1/2	1 3/4	1 1/2	1.5100	1.5032	1.7505	1.7495	1.5000	1.4990
JSI-2832-20	1 3/4	2	1 1/4	1.7547	1.7507	2.0010	2.0000	1.7500	1.7476

iglide® J - Linear Plain Bearing Flange Bearing, Inch

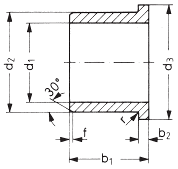

r = max. 0.5

Based on I.D.
f = .019 → $d_1 \le .393$
f = .031 → $.39 < d_1 \le 1.181$
f = .047 → $d_1 > 1.259$

Length Tolerance (b1)

Length (inches)			Tolerance (h13)
0.1181	to	0.2362	-0.0000 /-0.0071
0.2362	to	0.3937	-0.0000 /-0.0087
0.3937	to	0.7086	-0.0000 /-0.0106
0.7086	to	1.1811	-0.0000 /-0.0130
1.1811	to	1.9685	-0.0000 /-0.0154
1.9685	to	3.1496	-0.0000 /-0.0181

Part Number	d1	d2	b1	d3	b2	I.D. After Pressfit		Housing Bore		Shaft Size	
					-.0055	Max.	Min.	Max.	Min.	Max.	Min.
JFI-0204-06	1/8	1/4	3/8	.360	.047	.1280	.1262	.2515	.2510	.1250	.1241
JFI-0304-02	3/16	1/4	1/8	.375	.032	.1905	.1887	.2515	.2510	.1865	.1858
JFI-0304-04	3/16	1/4	1/4	.375	.032	.1905	.1887	.2503	.2497	.1865	.1858
JFI-0304-06	3/16	1/4	3/8	.375	.032	.1905	.1877	.2503	.2497	.1865	.1858
JFI-0304-08	3/16	1/4	1/2	.375	.032	.1905	.1887	.2503	.2497	.1865	.1858
JFI-0305-06	3/16	5/16	3/8	.370	.047	.1905	.1887	.3140	.3135	.1875	.1866
JFI-0305-08	3/16	5/16	1/2	.370	.047	.1905	.1887	.3140	.3135	.1875	.1866
JFI-0405-04	1/4	5/16	1/4	.500	.032	.2539	.2516	.3122	.3128	.2481	.2490
JFI-0405-06	1/4	5/16	3/8	.500	.032	.2539	.2516	.3122	.3128	.2481	.2490
JFI-0405-12	1/4	5/16	3/4	.500	.032	.2539	.2516	.3122	.3128	.2481	.2490
JFI-0406-03	1/4	3/8	3/16	.560	.047	.2539	.2516	.3765	.3760	.2500	.2491
JFI-0406-04	1/4	3/8	1/4	.560	.047	.2539	.2516	.3765	.3760	.2500	.2491
JFI-0406-08	1/4	3/8	1/2	.560	.047	.2539	.2516	.3765	.3760	.2500	.2491
JFI-0506-04	5/16	3/8	1/4	.500	.032	.3148	.3125	.3753	.3747	.3115	.3106
JFI-0506-06	5/16	3/8	3/8	.500	.032	.3148	.3125	.3753	.3747	.3115	.3106
JFI-0506-08	5/16	3/8	1/2	.500	.032	.3164	.3141	.3765	.3760	.3115	.3106

General Information

Area of Application

Ease of installation, integrated technology, compatability, size, stand-alone capability and the numerous connection possibilities allow this motion controller to perform to the highest standards in a wide range of applications, for example in decentralized automated production systems like handling or tooling machines.

Options

- FAULHABER offers the optional Multiplexer Board to operate multiple motion controllers from one RS-232 port.
- To accomadate our customers specialized needs we offer factory preconfiguring of Modes and Parameters to fit the application.
- The **FAULHABER Motion Mananger** is available for download from the internet at www.faulhaber.de or upon request.
- The adapters allow for simple attatchment to mounting railings.

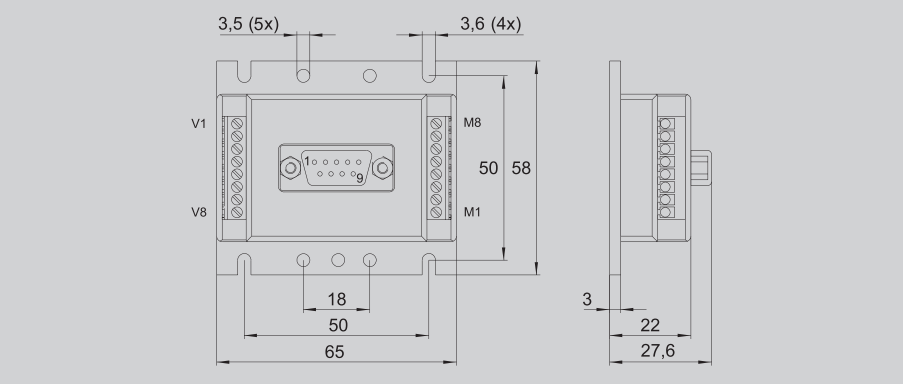

Connections

Supply Side:

No.	Function
V1	RS-232 TXD
V2	RS-232 RXD
V3	Analog GND
V4	Fault Output
V5	Analog Input
V6	+24V
V7	GND
V8	Input No. 3

SUB-D Connector:

No.	Function
2	RS-232 RXD
3	RS-232 TXD
5	GND

Motor Side:

No.	Function
M1	Input No. 5
M2	Input No. 4
M3	Channel A
M4	Channel B
M5	VCC (+5V)
M6	Signal GND
M7	MOTOR+
M8	MOTOR-

Data Sheet

General Specifications			
Supply Voltage	U_B	12 ... 28	V DC
PWM Switching Frequency	f_{PWM}	62,5	kHz
Efficiency	η	95	%
Max. Continuous Current	I_{cont}	5	A
Max. Peak Current	I_{max}	10	A
Current Consumption in the Electronics	I_{el}	0,06	A
Velocity Range		10 ... 30000	rpm
Output Voltage for External Use	VCC	5	V DC
-Max. Load Currecnt	I_{CC}	60	mA
Input No. 1 1)	Input Resistance	18	kΩ
Command Analog Velocity	Voltage Signal	± 10	V
	Slope of the Curve	1000 2)	rpm/V
Command Digital Velocity	PWM Signal	low 0...0,5 / high 4...30	V
	Frequency Range	100 ... 2000	Hz
	Pulse Duty Ratio 50%	0	rpm
	Pulse Duty Ratio <50%	left turning	
	Pulse Duty Ration >50%	right turning	
Step Frequency	f_{max}	100	kHz
Fault Output (Input No. 2)	Open collector	max. U_B / 30mA	
	No Error	Switched to GND	
	Programmed as an input	low 0...0,5 / high 4...U_B	V
Input No. 3 / No. 4 / No. 5	Logic Level	low 0...0,5 / high 4...30	V
Encoder Input	Logic Level	low 0...0,5 / high 4...30	V
	Max. Frequency	200	kHz
Port	RS-232	9600 (1200,2400,4800,19200)	Baud
Memory for Programs	Serial EEPROM	7936	Bytes
Operating Temperature Range		0 ... +70	°C
Storage Temperature Range		–25 ... +85	°C
Weight		110	g

1) Can be set over the RS-232 port. (Factory configuration: Command Analog Velocity)

2) Preset value. Can be changed over the RS-232 port.

B.2 Experimental Results

Curve	**Equation**	**Avg. Error**	**Max. Error**
Exp: Rigid Tail			
F_{R0}	$F_{R0} = 5.21 \times 10^{-9}(\omega/\pi) - 4.77 \times 10^{-11}$	4.7%	36.1%
Exp: Flex Tail: Cyl			
F_{R0}	$U = -3.96 \times 10^{-10}(\omega/\pi)^2$ $+5.11 \times 10^{-9}(\omega/\pi) - 4.75 \times 10^{-9}$	13.3%	51.5%
Exp: Flex Tail: Rec			
F_{R0}	$U = 1.78 \times 10^{-9}(\omega/\pi) + 1.49 \times 10^{-10}$	13.6%	68.1%

Table B.1: Equations, and error analysis, of curve fits for experimental data as plotted in Figures 5.15 and 5.21